

UC San Diego

UC San Diego Electronic Theses and Dissertations

Title

Investigating Fusion Relevant Plasma Material Interactions: Analyzing Hydrogenic Isotope Retention in Heavy-Ion Damaged Tungsten

Permalink

<https://escholarship.org/uc/item/69h4v5q9>

Author

Simmonds, Michael James

Publication Date

2018

Peer reviewed|Thesis/dissertation

UNIVERSITY OF CALIFORNIA, SAN DIEGO

**Investigating Fusion Relevant Plasma Material Interactions:
Analyzing Hydrogenic Isotope Retention in Heavy-Ion Damaged Tungsten**

A dissertation submitted in partial satisfaction of the
requirements for the degree
Doctor of Philosophy

in

Physics

by

Michael James Simmonds

Committee in charge:

Professor George R. Tynan, Chair
Professor Cliff M. Surko, Co-Chair
Professor Renkun Chen
Professor Patrick Diamond
Professor Vitali F. Nesterenko
Professor Frank Wuerthwein

2018

Copyright

Michael James Simmonds, 2018

All rights reserved.

The dissertation of Michael James Simmonds is approved,
and it is acceptable in quality and form for publication on
microfilm and electronically:

Co-Chair

Chair

University of California, San Diego

2018

DEDICATION

To my grandfather for teaching me to question and his infinite patience.

To my mother for allowing me to question and her enduring support.

TABLE OF CONTENTS

Signature Page	iii
Dedication	iv
Table of Contents	v
List of Figures	viii
List of Tables	xiii
Acknowledgements	xiv
Vita	xv
Abstract of the Dissertation	xvii
Chapter 1	Introduction	1
	1.1 Fusion	1
	1.2 Controlled Fusion Energy	2
	1.2.1 Hydrogenic Fusion Fuel	3
	1.2.2 Fusion Reactor Concepts	4
	1.2.3 Tokamak Reactor	5
	1.3 Plasma-Material Interactions	9
	1.3.1 Neutron Damage	13
	1.3.2 Impact to Tritium Fuel Cycle and Inventory	13
Chapter 2	Experimental Methods	16
	2.1 Tungsten (W) as a Plasma Facing Material (PFM)	16
	2.2 Laboratory Devices to Mimic Fusion PMI Environments	17
	2.2.1 Plasma Devices	18
	2.2.2 Ion Accelerator	19
	2.3 Trapped D Measurements	20
	2.3.1 Nuclear Reaction Analysis	21
	2.3.2 NRA analysis programs	29
	2.3.3 Thermal Desorption Spectroscopy	30
	2.3.4 TDS Analysis Program	31
Chapter 3	Previous Results	35
	3.1 D Retention Experiments in Heavy Ion Damaged W	35
	3.2 Defect Recovery/Annealing	36
	3.3 Application of Reaction-Diffusion Codes	39
	3.4 Isolating Various Traps	39

Chapter 4	Reduced Deuterium Retention in Simultaneously Damaged and Annealed Tungsten	43
	4.1 Introduction	43
	4.2 Experiment	44
	4.2.1 W Sample Preparation	44
	4.2.2 Heavy-ion Displacement Damage in W	45
	4.2.3 Concurrent Heating During Damage	45
	4.2.4 D ₂ Plasma Exposure	46
	4.2.5 Nuclear Reaction Analysis (NRA)	46
	4.2.6 Thermal Desorption Spectroscopy (TDS)	47
	4.3 Results	48
	4.4 Discussion	52
	4.5 Summary	55
	4.6 Acknowledgments	56
Chapter 5	Expanding the Capability of Reaction-diffusion Codes using Pseudo Traps and Temperature Partitioning: Applied to Hydrogen Uptake and Release from Tungsten	57
	5.1 Introduction	57
	5.2 TMAP7 Simulation	59
	5.3 Expanding TMAP7	66
	5.4 Verification of the PTTP Scheme: Simulating 3 traps with 2 traps . .	70
	5.5 Using the PTTP Scheme to model D retention in damaged W with 6 traps	73
	5.6 Discussion	78
	5.7 Summary	80
	5.8 Acknowledgments	80
Chapter 6	Isolating the Detrapping of Deuterium in Heavy Ion Damaged Tungsten via Partial Thermal Desorption	82
	6.1 Introduction	82
	6.2 Experiment	84
	6.2.1 Sample Preparation	84
	6.2.2 Heavy Ion Damage	85
	6.2.3 D ₂ Plasma Exposure	85
	6.2.4 Partial TDS	86
	6.2.5 NRA	86
	6.2.6 Final TDS	87
	6.3 Results	88
	6.4 Isolating Detrapping Energies	92
	6.4.1 NRA Subtraction	93
	6.4.2 TDS Subtraction	95
	6.5 TMAP Simulation with PTTP	96

	6.5.1 Fitting Results	99
	6.6 Discussion	101
	6.7 Summary	104
	6.8 Acknowledgments	105
Chapter 7	Conclusions and Future Work	106
	7.1 TDS and Detrapping Energies	107
	7.2 Further Isolating Defects	108
	7.3 TMAP Modification and Updates	109
Bibliography	110

LIST OF FIGURES

Figure 1.1:	Tokamak coil geometry and corresponding magnetic field schematic [1]. The blue toroidal field coils and green inner poloidal field coils induce the corresponding color magnetic fields shown as arrows. The poloidal field also induces an increased plasma current.	6
Figure 1.2:	Schematic of the ITER tokamak device depicting fundamental components such as field coils, central solenoid, vacuum vessel, blanket module, and divertor [2]. The modular design allows for individual component replacement over the lifetime of operation.	7
Figure 1.3:	The ITER design uses a beryllium wall in the main plasma chamber, and a tungsten divertor [55] (adapted). The divertor consists of replaceable cassettes. The nested lines are magnetic field contours. The confined plasma is bounded by the separatrix, which is the last field contour that is closed. .	8
Figure 1.4:	Schematic illustration of the complex, synergistic, and inherently multi-scale surface interactions occurring at the material surface in a realistic magnetic fusion plasma environment [57]. H, hydrogen; D, deuterium; T, tritium; PFC, plasma facing component; γ , gamma ray.	10
Figure 1.5:	Potential energy diagram for trapping of D atom in a metal lattice [61]. Potentials shown are the energies for detrapping (E_{dt}), binding (E_b), trapping (E_{tr}), diffusion (E_D), and the difference between trapping and diffusion (E_x).	11
Figure 1.6:	Cross-sectional Scanning Electron Microscope (SEM) images of W targets exposed to pure He plasma at 1120 K for exposures times of (a) 300 s, (b) 2.0×10^3 s, (c) 4.3×10^3 s, (d) 9.0×10^3 s, and (e) 2.2×10^4 s [6].	12
Figure 1.7:	Roth <i>et al.</i> [39] assessed previous experimental data on various PFM to predict the overall component lifetime due to T retention. Note that with a 700 g T limit, W has the lowest retention and longest overall lifetime.	14
Figure 2.1:	Wampler <i>et al.</i> [55] presented various erosion rates for PFM candidates. Note the erosion rate is negatively correlated to atomic mass. Hence W presents the lowest erosion rate.	17
Figure 2.2:	Schematic for the major components of the MØRI TM - 200 RF plasma source [53] (adapted). An azimuthally symmetric helicon wave is excited by the antenna structure and propagates axially along the diverging magnetic field lines into a field-free downstream bucket.	19
Figure 2.3:	The geometry of the sample, detector, and 3 mm wide slit shielding are shown in the schematic [28] (adapted). The probing beam with initial energy E_0 is normal to the W surface. The detector was located 135° relative to the incident beam and ~ 42 mm away, from sample to shield center.	22
Figure 2.4:	The instantaneous (dashed lines for E_1 on the left axis) and detected proton energies (solid lines for E_{Detect} on the right axis) are plotted with respect to nuclear reaction depth (x) for various initial probing energies (E_0).	25

Figure 2.5:	The nuclear reaction cross section for the $D(^3\text{He},p)^4\text{He}$ reaction collected at a detector reaction angle of 135° [60]. The cross section is peaked for an incident ^3He beam energy near 0.6 MeV. Note that the x-axis is the instantaneous ^3He energy (E_1) when the nuclear reaction occurs.	26
Figure 2.6:	NRA data from a heavy ion damaged and D exposed W sample is shown. a.) D concentration (solid-shaded) and cross sections (dashed) for various initial energies are plotted with respect to depth. b.) Both the D concentration and cross sections are plotted with respect to detected energy.	27
Figure 2.7:	QMS partial pressures plotted against mass to charge ratio (m/q) for one time step (i.e. one sweep). Each peak is fit with a quadratic to find the peak value and remove outliers.	32
Figure 2.8:	The raw HD partial pressure is plotted in black for the m/q value of 3. Performing a stabilization and quadratic fit to the HD peak results in the blue dotted line. A Gaussian filter over 5 time steps produces the smoothed red line. Note that the post-analysis lines are offset for clarity.	33
Figure 2.9:	TDS data is shown for a sample with a linear heating ramp of 0.5 K/s held fixed at 1300 K and followed by additional cooling and heating ramps. Beyond the initial temperature ramp, the HD and D_2 has effectively degassed from the sample and what remains is primarily due to water on the chamber	34
Figure 3.1:	Damage microstructure in (a and b) as-irradiated tungsten (1.5 dpa, 2 MeV W^+ , 773 K) and post-irradiation annealed tungsten subject to conditions of (c) 1073 K for 1 h, (d) 1223 K for 1 h, (e) 1373 K for 1 h, (f) 1673 K for 1 h.	38
Figure 3.2:	In order to simulate six detrapping energies, Shimada <i>et al.</i> [44] separately simulated three lower energy traps (a), three higher energy traps (b), and summed the result (c).	40
Figure 3.3:	Ogorodnikova <i>et al.</i> [30] (adapted) plotted various binding energies (E_b) against associated defects (arbitrary x-axis).	41
Figure 4.1:	TDS data is shown for a sample with a linear heating ramp of 0.5 K/s held fixed at 1300 K and followed by additional cooling and heating ramps. Beyond the initial temperature ramp, the HD and D_2 has effectively degassed from the sample and what remains is primarily due to water on the chamber	48
Figure 4.2:	NRA measured D depth profiles for 3 samples of increasing temperature during displacement damage by 3.4 MeV Cu ions. The SRIM calculated dpa profile is also shown with a peak dpa of 0.2 near $0.6 \mu\text{m}$	49
Figure 4.3:	D release measured by TDS on samples simultaneously damaged with 3.4 MeV Cu ions while being heated. Decreasing retention trending toward the undamaged/control sample is found. Peaks 1-3 with release temperatures at 480, 600, and 825 K are indicated.	49
Figure 4.4:	The total D retention measured via NRA up to $6 \mu\text{m}$ and TDS throughout the bulk of the samples.	50

Figure 4.5:	The thermal desorption flux (solid line) of D is fit with the sum of 3 Gaussians peaked at 480, 600, and 825 K (dashed lines).	51
Figure 4.6:	Three Gaussians peaked near $\sim 480, 600,$ and 825 K were fit to TDS profiles of D release. The total D retention associated with each Gaussian is plotted here, demonstrating the recovery from damage with concurrent elevated sample temperatures.	52
Figure 4.7:	Total D retention normalized to the displacement damage profile (i.e. $\text{dpa} \cdot \mu\text{m}$) shows agreement between Sakurada [41], Markina [26], Ogorodnikova [33], and this work. The inset plot shows the profiles for Fe (green), W (blue), and Cu (red) with peak dpa of 0.1, 0.2, and 0.45 respectively.	53
Figure 4.8:	The fractional recovery, $F_r(T) = (R_t(300K) - R_t(T))/R_t(300K)$, for both high energy traps correlates with an activation energy of 0.1 eV.	55
Figure 5.1:	Traps 1-3 (dashed lines) are simulated using TMAP and the sum total (green) is compared to experimental NRA data (thick black) with a NRMSE of 0.7. Note that the heavy ion damage profile simulated in SRIM (red) defines the spatial profile of induced traps used in TMAP shown with arbitrary units	62
Figure 5.2:	The residual error (dashed red) shows the difference between the TMAP simulated release peaks (green) and the experimental TDS data (thick black) with a NRMSE of 0.7.	63
Figure 5.3:	The experimental TDS data for a) D_2 and b) HD fluxes released from dynamically annealed damaged W. Samples damaged with Cu ions at RT (blue), 573 K (cyan), 873 K (green), and 1243 K (red) show reduced D retention.	65
Figure 5.4:	The calculated residence times for traps 2 and 3 exceed total implantation time (horizontal light green) for the implantation temperature (vertical grey).	71
Figure 5.5:	The residual error (dashed red) between the exact (thick black) and pseudo (green) solutions for the D depth profile (i.e. after the implantation phase). Note that the exact solution is the sum of D filling traps 1-3, whereas the pseudo solution is the sum of trap 1 and the pseudo trap.	72
Figure 5.6:	The pseudo solution (green) with no temperature partition begins to deviate from the exact solution (thick black) as the temperature approaches the second release peak, which activates the lowest energy trap contained within the pseudo trap.	73
Figure 5.7:	The D inventory of each trap displays the trapping and release directly, without the effects of diffusion and surface recombination shown with the surface flux in Fig 6. The total inventory for the exact solution (thick black) is the sum of traps 1-3	74
Figure 5.8:	PTTP scheme (green) applied using 2 traps at any given temperature. Below 555 K (vertical dashed orange), traps 1 and pseudo are modeled. Above 555 K, only traps 2 and 3 are modeled. The residual error (dashed red), magnified by 10, with respect to the exact solution (thick black)	75

Figure 5.9:	The calculated residence time for traps 3-6 exceed the total implantation time (horizontal light green) for the implantation temperature (vertical grey). Thus traps 3-6 can be well modeled as one pseudo trap in the implantation phase.	76
Figure 5.10:	The total D concentration simulated with PTTP (green) is the sum of all 6 trap concentrations (dashed lines) after the implantation phase. The pseudo trap is separated into its constituent traps 3 through 6. The NRMSE for the PTTP simulation is 0.7 with respect to the experimental NRA data	77
Figure 5.11:	The total D inventory in each trap as well as the total inventory (thick black). The discontinuity of the pseudo trap (dashed green) is due to removing the lowest energy trap in the pseudo trap at each transition temperature (vertical dashed orange).	78
Figure 5.12:	The full PTTP simulation (green) with 6 traps compared to experimental RT damaged W (thick black). The residual error (dashed red) is 4% and the NRMSE is 0.95.	79
Figure 6.1:	The D concentration measured through NRA decreases with increasing pTDS temperature. The SRIM predicted trap profile (dot-dashed orange) for 5 MeV Cu^{2+} displays a peak near $\sim 0.9 \mu\text{m}$ and shown here scaled to 1. Note that the experimental dose resulted in a calculated peak dpa of 0.12.	89
Figure 6.2:	The D surface flux during pTDS (dashed) and the final TDS (solid) are plotted with respect to a 0.5 K/s linear heating ramp. Once pTDS samples reached a specific peak-and-hold temperature, the flux during the 2.5 hr peak-and-hold decays exponentially in time and approaches zero at this fixed temperature.	90
Figure 6.3:	The sum total D retention measured in the first $5.5 \mu\text{m}$ through NRA and the bulk through TDS. Plotted at the plasma exposure sample temperature of 373 K, the “No pTDS” sample shows the largest deviation from NRA. . . .	92
Figure 6.4:	The difference in D concentration between consecutive pTDS samples are shown as solid lines. The damage profile of zone II is further defined and fit well by the SRIM dpa profile scaled to 0.3 for ease of comparison (dot-dashed orange).	94
Figure 6.5:	The “No Cu” sample is shown as solid black with an exponential decay function (dot-dashed red). The solid blue line representing “No pTDS” subtracting both the “No Cu” and 597 K pTDS NRA profiles isolates the low energy traps due to heavy ion damage.	95
Figure 6.6:	The difference in D flux during final TDS ($\Delta\Gamma$) for each consecutive pTDS sample pair are shown. The first dark blue line displays a broader primary peak than the other differences. Each of the remaining differences can be modeled with a single detrapping energy.	96
Figure 6.7:	The total trap concentration (black) compared to the “No pTDS” NRA data (blue). The individual trap concentrations for $k = 1-6$ are shown as dot-dashed lines.	101

Figure 6.8:	The comparison of the NRA data (solid) and the simulation result (dashed) using the optimized fit parameters, summarized in Table 6.2. For clarity, only 4 samples are shown.	102
Figure 6.9:	The comparison of the TDS data (solid) and the simulation result (dashed) using the optimized fit parameters, summarized in Table 6.2.	103

LIST OF TABLES

Table 5.1:	Summary of detailed experimental conditions used as inputs to the TMAP7 modeling.	60
Table 6.1:	Summary of the fixed parameters and activation energies (E_a) used in the TMAP simulation. Note that the recombination coefficient is changed depending on the modeling phase: the Pick and Sonnenberg value is used during plasma implantation and the Anderl value during thermal desorption.	97
Table 6.2:	Summary of the best fit parameters for each trap (k). The peak concentrations (C_k^j) in each zone (j) and the detrapping energies (E_k) modeled using the PTTP scheme.	100

ACKNOWLEDGEMENTS

To everyone within the PISCES group, thank you for your guidance and knowledge. Foremost, Dr. George Tynan for giving me the opportunity to work alongside a great team of scientists. I thank you all for your time: Dr. Russ Doerner, Dr. Matthew Baldwin, Dr. Jonathan Yu, Dr. Saikat Chakraborty Thakur, Dr. Daisuke Nishijima, Dr. Anže Založnik, Dr. Daniel Alegre, Ray Seraydarian, Leo Chousal, Rollie Hernandez, and Tyler Lynch. Leo, Rollie, and Tyler were always there to help fix any equipment that broke. Russ and Matt lent me an ear and pushed me to finish my publications. Saikat, Anže, Daniel, and Daisuke for our conversations. My fellow graduate students: (soon to be Dr.) Shota Abe, Dr. Rima Hajjar, Dr. Jordan Gosselin, and especially Dr. Joseph Barton for commiserating in the graduate experience. Finally, Jonathan for helping polish my ideas and their eventual publication.

Chapter 4, including text and data, is in part a reprint of the material as it appears in M.J. Simmonds, Y.Q. Wang, J.L. Barton, M.J. Baldwin, J.H. Yu, R.P. Doerner, G.R. Tynan, Reduced Deuterium Retention in Simultaneously Damaged and Annealed Tungsten, *J. Nucl. Mater.* 494 (2017). The dissertation author was the primary investigator and author of this paper.

Chapter 5, including text and data, is in part a reprint of the material as it appears in M.J. Simmonds, J.H. Yu, Y.Q. Wang, M.J. Baldwin, R.P. Doerner, G.R. Tynan, Expanding the capability of reaction-diffusion codes using pseudo traps and temperature partitioning: Applied to hydrogen uptake and release from tungsten, *J. Nucl. Mater.* 508 (2018). The dissertation author was the primary investigator and author of this paper.

Chapter 6, including text and data, is in part a reprint of the material as it appears in M.J. Simmonds, T. Schwarz-Selinger, J.H. Yu, M.J. Baldwin, R.P. Doerner, G.R. Tynan, Isolating the Detrapping of Deuterium in Heavy Ion Damaged Tungsten via Partial Thermal Desorption, *J. Nucl. Mater.* submitted (2018). The dissertation author was the primary investigator and author of this paper.

VITA

2002	A.S. in Physics, Moorpark College, Moorpark, CA
2001-2007	Sergeant/Helicopter power plant engineer, United States Marine Corps
2008	B.S. in Physics (Computational Physics minor), University of California, San Diego
2010	M.S. in Physics, University of California, San Diego
2008-2012	Graduate Teaching Assistant, University of California, San Diego
2012-2018	Graduate Student Researcher, University of California, San Diego
2018	Ph. D. in Physics, University of California, San Diego

PUBLICATIONS

M.J. Simmonds, Y.Q. Wang, J.L. Barton, M.J. Baldwin, J.H. Yu, R.P. Doerner, G.R. Tynan, Reduced Deuterium Retention in Simultaneously Damaged and Annealed Tungsten, Journal of Nuclear Materials, 494, (2017) 0022-3115.

M.J. Simmonds, J.H. Yu, Y.Q. Wang, M.J. Baldwin, R.P. Doerner, G.R. Tynan, Expanding the capability of reaction-diffusion codes using pseudo traps and temperature partitioning: Applied to hydrogen uptake and release from tungsten, Journal of Nuclear Materials, 508, (2018).

M.J. Simmonds, T. Schwarz-Selinger, J.H. Yu, M.J. Baldwin, R.P. Doerner, G.R. Tynan, Isolating the detrapping of deuterium in heavy ion damaged tungsten via partial thermal desorption, Journal of Nuclear Materials, submitted (2018).

R.P. Doerner, M.J. Baldwin, M. Simmonds, J.H. Yu, L. Buzi, T. Schwarz-Selinger, Quantitatively measuring the influence of helium in plasma-exposed tungsten, Nuclear Materials and Energy, 12, (2017), 2352-1791.

J.H. Yu, M. Simmonds, M.J. Baldwin, R.P. Doerner, Deuterium desorption from tungsten using laser heating, Nuclear Materials and Energy, 12, (2017), 2352-1791.

D. Alegre, M.J. Baldwin, M. Simmonds, D. Nishijima, E.M. Hollmann, S. Brezinsek, R.P. Doerner, A parametric study of helium retention in beryllium and its effect on deuterium retention, Physica Scripta, (2017), T170.

F.L. Tabars, D. Alegre, M. Baldwin, D. Nishijima, M. Simmonds, R. Doerner, E. Alves, R. Mateus, Studies of lithium deposition and D retention on tungsten samples exposed to Li-seeded plasmas in PISCES-A, Plasma Physics and Controlled Fusion, 59, 4, (2017).

S. Cui, M. Simmonds, W. Qin, F. Ren, G. R. Tynan, R. P. Doerner, R. Chen, Thermal conductivity reduction of tungsten plasma facing material due to helium plasma irradiation in PISCES using the improved 3-omega method, Journal of Nuclear Materials, 486, (2017), 0022-3115.

G.R. Tynan, R.P. Doerner, J. Barton, R. Chen, S. Cui, M. Simmonds, Y. Wang, J.S. Weaver, N. Mara, S. Pathak, Deuterium retention and thermal conductivity in ion-beam displacement-damaged tungsten, Nuclear Materials and Energy, 12, (2017), 2352-1791.

ABSTRACT OF THE DISSERTATION

**Investigating Fusion Relevant Plasma Material Interactions:
Analyzing Hydrogenic Isotope Retention in Heavy-Ion Damaged Tungsten**

by

Michael James Simmonds

Doctor of Philosophy in Physics

University of California, San Diego, 2018

Professor George R. Tynan, Chair
Professor Cliff M. Surko, Co-Chair

A fundamental obstacle to controlled fusion devices is the retention of hydrogenic fuel in Plasma Facing Material (PFM) that forms the first-wall and divertor target. A mixed plasma of primarily deuterium (D) and tritium (T) is magnetically confined and heated in the core of a confinement device. The resulting fusion reaction will create energetic ($> \text{MeV}$ kinetic energy) helium (He) and neutrons (n^0). The 14 MeV neutrons are unconfined and thus will induce damage throughout the PFM that can act to trap plasma ions that impinge on the surface, become neutral atoms, and then diffuse into the PFM. The ability to accurately quantify the T fuel loss

to the PFM is needed to ensure that a reactor design can produce enough T to keep the reactor operating and to ensure radiological safety requirements. Tungsten (W) is a primary candidate for PFMs in current and future fusion devices. To avoid the use of radiologically activated samples, in this work neutron damage and T retention are simulated with heavy ion damage and D respectively. W samples were prepared, subjected to heavy ion displacement damage, and then exposed to a relatively low flux D₂ plasma to populate the induced defects with trapped D atoms. Nuclear Reaction Analysis (NRA) and Thermal Desorption Spectroscopy (TDS) were then used to measure the retention of D within the W samples.

The first-ever study of in-situ annealing of defects during damage production, referred to here as dynamic annealing, was carried out. Plasma-implanted D retention in polycrystalline W that had been previously subjected to copper (Cu) ion damage while holding the samples at a fixed elevated surface temperature was investigated. This approach allows us to determine if the annealing rate is fast enough relative to the rate of damage production to materially affect the defect density within the sample. Both NRA and TDS measure a significant reduction in D retention for samples damaged at elevated temperature. TDS quantitatively shows that the lowest energy trap remains largely unaffected while higher energy traps, induced by Cu ions, are annealed and approach intrinsic concentrations as the temperature during ion damage approaches 1243 K. Analysis of TDS data yields an activation energy of (0.10 ± 0.02) eV for recovery of heavy-ion damage-induced traps at elevated temperature.

In order to accurately simulate the experimental implantation and thermal desorption of D in W, the capability of the Tritium Migration Analysis Program (TMAP7) needed to be expanded. TMAP7 can model systems with no more than three active traps per atomic species. To overcome this limitation, we developed a Pseudo Trap and Temperature Partition (PTTP) scheme allowing multiple inactively releasing traps to be accounted for by one pseudo trap, simplifying the system of equations to be solved. Without modifying the TMAP7 source code, the PTTP scheme is shown to successfully model the D retention using six traps. We demonstrate the full

reconstruction from the plasma implantation phase through the controlled thermal desorption phase with detrapping energies near 0.9, 1.1, 1.4, 1.7, 1.9 and 2.1 eV for a W sample damaged at room temperature.

In the above experimental modeling, the spatial location and density of traps that define the total trap profile were not well constrained. Motivated by this issue, we devised a new Partial Thermal Desorption Spectroscopy (pTDS) technique to systematically and progressively depopulate trapped deuterium (D) from heavy ion damaged tungsten (W) trap sites to isolate and resolve both their spatial location and detrapping energies. Difference TDS profiles from samples with progressively higher pTDS peak temperature permits the isolation of traps that release between the two pTDS temperatures. Results indicate detrapping energies of 1.0, 1.2, 1.4, 1.5, 1.7, 1.9, and 2.5 eV with instantaneous surface recombination. NRA of these samples then shows three spatial zones of D populated defects: (I) the near surface at depths less than $0.1 \mu\text{m}$, (II) the heavy ion displacement damage peaked near $1 \mu\text{m}$, and (III) the remaining bulk with uniform intrinsic defects. The complete cycle of D_2 plasma loading, to pTDS, NRA, and finally full TDS could be accurately modeled with TMAP7 utilizing a Pseudo Trap and Temperature Partition (PTTP) scheme developed previously with these seven distinct release peaks distributed across the three spatial zones.

Chapter 1

Introduction

1.1 Fusion

The primary source of energy and the fundamental constituents of life on Earth comes from nuclear fusion. Within the Sun and all main-sequence stars, the high density and temperature within the core induces the fusion of atomic nuclei. For atoms separated at distances on the order of femtometer (10^{-12} m), the strong nuclear force overcomes the Coulomb repulsion of proton nuclei and allows fusion to occur.

The fusion process is typically exothermic for light atoms, like hydrogen (H), and endothermic for heavy atoms more massive than iron (Fe). Elements with low mass have a smaller number of repulsive protons to overcome to form a stable fused nucleus. When two such light nuclei fuse together, the particles within the newly formed nucleus are more tightly bound together than were the nuclear particles of the incoming nuclei. As a result, a portion of the nuclear binding energy is released in the form of the kinetic energy of the nuclei and particles that emerge from the fusion reaction. The majority of atoms with masses below Fe, including carbon (C), were created through the process of stellar nucleosynthesis, the fusion of lighter particles into more massive elements within the core of stars.

The kinetic energy of the fusion reaction products can heat the surrounding matter, liberating electrons, and ionizing the neutral atoms resulting in a formation and maintenance of a hot plasma. Unlike the gaseous state of matter, plasma has a significant fraction of ionized atoms and is defined by the collective effects of these charged particles (i.e. ions and electrons). This hot plasma acts like a conductive fluid that in turn creates currents that both drive and are driven by magnetic fields. Photons created in the stellar core are absorbed and re-emitted many times before reaching the last scattering surface. Emitted in all directions, only a small fraction reaches the Earth. Other than geothermal sources, this electromagnetic radiation powers nearly all life in an unbroken chain from photosynthesis.

Aside from basic science, the need for renewable energy sources is what motivates research into controlled fusion as an energy source. Other than fossil fuels, the time-varying nature of carbon-free sources such as solar and wind technologies combined with current limitations to energy storage may limit the ultimate contribution of these renewable resources to human energy demand. Thus it seems likely that the energy required to sustain human civilization will need to come from multiple sources in addition to renewable sources. Controlled fusion offers the promise of abundance and sustainability from hydrogenic fuel available on Earth. Additionally, unlike fission reactors, when properly designed, fusion reactors offer the prospect of nuclear energy with relatively short-lived radioactive waste and no production of fissile materials that could be diverted for use in nuclear weapons. Most importantly, properly designed fusion reactors might be able to eliminate the possibility of accidents that release a large inventory of long-lived radioisotopes into the surrounding environment.

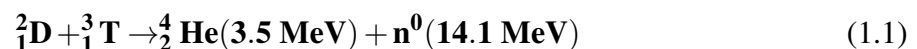
1.2 Controlled Fusion Energy

To control and maintain a fusion reaction within a reactor, fusion fuel must be confined for some period of time at sufficiently large temperatures and densities to induce fusion. The

ultimate goal is ignition, which is defined as the point at which fusion is self-sustainable and no external heating is needed to maintain the nuclear reaction. The Lawson criterion was developed to estimate the minimum parameters needed for ignition, and is described in terms of a critical minimum value of the product of density (n) and confinement time (τ_E). A further extension to this criterion involves the temperature (T) and is known as the triple product ($nT\tau_E$). This figure of merit is more sensitive to ignition conditions since the probability of a fusion reaction to occur is highly dependent on temperature.

1.2.1 Hydrogenic Fusion Fuel

Before discussing a fusion reactor concept, the fusion reaction to be induced and controlled must be identified. The Deuterium-Tritium (D-T) reaction (eq. 1.1) has the largest cross section at the lowest temperatures of any plausible exothermic fusion reactions and thus is the easiest reaction to produce in a laboratory device. Both D and T are heavy isotopes of H since they all have one proton. The D-T reaction produces a more massive ^4He and less massive neutron. The exothermic energy of 17.6 MeV is divided with respect to the inverse mass of each product, and as a result the ^4He nucleus receives 3.5 MeV and the neutron has 14.1 MeV of kinetic energy. Note that the highly energetic ^4He is also referred to as an α particle; because it is charged it can be trapped within the magnetic field of the plasma confinement device. The α particle can deposit its kinetic energy into the plasma via a series of coulomb collisions and as a result it can heat the plasma. Since the neutron product is not charged, it is not confined to the plasma or magnetic field lines and effectively transmits energy to the walls of the reactor. The neutron energy is deposited within the wall material and can damage the material crystalline structure via a series of collisions that displace atoms from their lattice position. It should be noted that the neutron also activates the material radiologically and transmute the atoms within the material.



1.2.2 Fusion Reactor Concepts

In order to understand how to control the fusion process we can draw an analogy to stellar fusion. There, gravity acts as the primary controlling mechanism. Gas giants, such as Jupiter, are not quite massive enough to create the conditions needed to achieve fusion. In a massive enough object, such as the Sun, the gravitational force can compress matter to densities and temperatures that are high enough to produce nuclear fusion in hydrogenic fuel. The excess energy released in the exothermic fusion reaction results in heating the stellar material to induce the most energetic state of matter, a plasma. The hot plasma then emits radiation, which eventually makes its way towards the surface. A balance between the energy production rate and the radiation loss rate then maintains the core plasma at conditions needed to sustain the fusion reactions.

While gravitational confinement is not feasible on Earth, there are two competing methods that are subjects of active research, inertial and magnetic confinement. Inertial fusion entails a quick pulse of energy focused on a relatively small pellet of hydrogenic fuel to compress it to densities high enough to produce fusion. The magnetic confinement approach has led to the development of several schemes to contain and condense a hydrogenic plasma to produce fusion. The basic principle relies on the fact that moving charged particles exhibit a helical orbit in the presence of a magnetic field line that acts as a guiding center. An idealized solenoid provides confinement along the long central axis but not at the ends. Linear devices such as magnetic mirrors were designed to confine a plasma along the long axis. The field lines were constricted on both ends to reduce particle loss and cause particles to reflect at each end instead of escaping. Eventually this concave field line geometry was shown to reduce the axial confinement due to the plasma instabilities which lead to transport of hot plasma from the central region towards the edge where the heat is lost to the surroundings. To prevent both the end losses and remove the concave field lines, the linear design was curved back unto itself into a torus.

Though the toroidal confinement scheme removes the loss at the ends of a linear device,

the geometry of a torus introduces an asymmetry due to the inner and outer radii. Whereas the idealized solenoid field coils surrounding a linear machine produce a uniform magnetic field, at least sufficiently far from the ends, the toroidal field coils have a denser flux of magnetic field lines near the inner radius. This nonuniform field has an inverse radial dependence that causes a magnetic gradient. The magnetic field along the toroidal axis crossed with this magnetic gradient gives rise to particle drift in opposite directions for ions and electrons. This charge separation induces a vertical electric field that crossed with the toroidal magnetic field in turn causes a particle drift towards the outer radius. The result is that a simple toroidal field coil geometry is not capable of long confinement time for the central plasma needed to sustain fusion.

Two designs utilizing a torus that attempt to correct the outward drift are the stellarator and tokamak. A poloidal magnetic field can guide particles near the outer radius towards the inner radius. The stellarator twists the field coil geometry to add a poloidal component. The tokamak concept is the primary focus of this work and explored further. Utilizing a simple toroidal field coil arrangement, the tokamak has a set of field coils located within the inner radius of the torus (i.e. the central stack) that generate a poloidal magnetic field as shown in fig. 1.1. The poloidal field generated by the central stack is due to the ramping of the current driving the electromagnet. The poloidal magnetic field increases the toroidal plasma current that in turn further increases the poloidal field. The summation of magnetic field components results in a helical magnetic field geometry that leads to increased plasma confinement times and reduced heat loss.

1.2.3 Tokamak Reactor

A toroidal chamber surrounded by electromagnetic field coils, the tokamak is an experimental device developed to confine a hydrogenic plasma to produce fusion. A set of toroidal field coils produces a strong toroidally directed magnetic field. An auxiliary set of coils threading down through the hole of the torus can be pulsed transiently to induce a toroidal electric field. This then produces a toroidal current which, in turn, generates a poloidal magnetic field. The

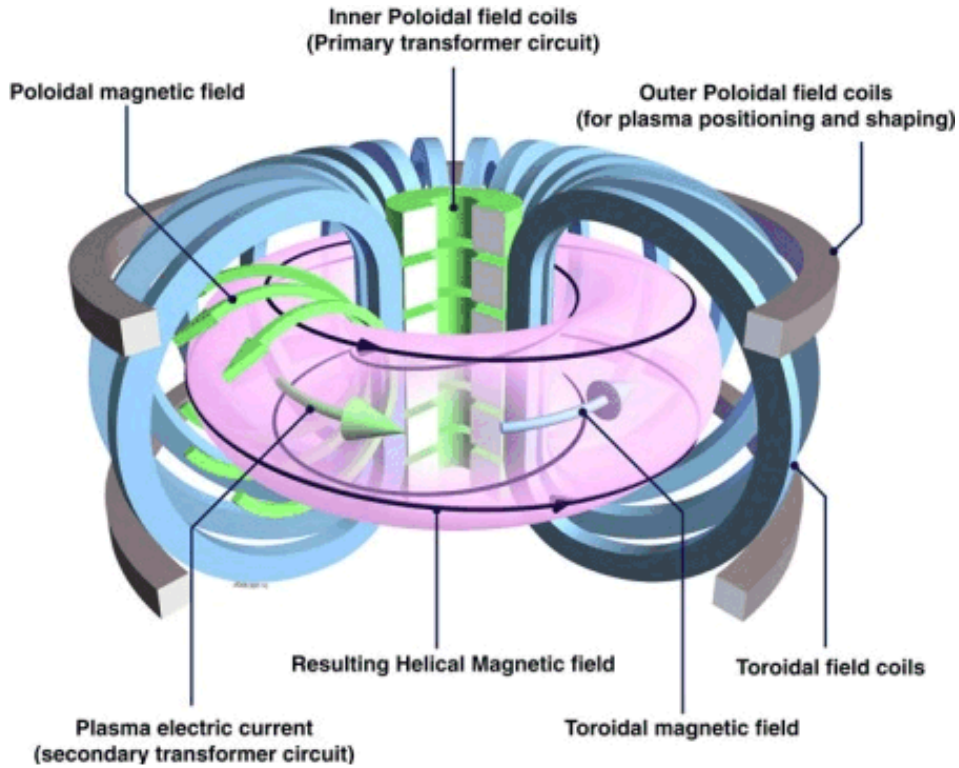


Figure 1.1: Tokamak coil geometry and corresponding magnetic field schematic [1]. The blue toroidal field coils and green inner poloidal field coils induce the corresponding color magnetic fields shown as arrows. The poloidal field also induces an increased plasma current. The combined magnetic fields create helical field lines shown as black arrows.

combination of toroidal and poloidal magnetic fields then results in helically shaped field lines that densely cover toroidally shaped magnetic flux surfaces. The plasma current resistively heats the plasma to a few keV temperature. Higher temperatures are reached by adding additional, or auxiliary, heating from energetic particle beams or radio-frequency heating.

The fusion reaction rate is highly dependent on the plasma temperature. For D-T based fusion, the plasma inside a fusion reactor must approach 100 million Kelvin to attain a high reaction rate. Magnetic confinement isolates the plasma from the walls of the device, but some plasma can leak across the magnetic field and reach the so-called scrape-off layer (SOL) which is the narrow zone at the plasma edge where magnetic field lines intercept the device walls. The thermal energy produced from fusion is absorbed as heat in the walls of the vessel; in addition energetic neutrons escape the plasma and deposit their energy deeper within the reactor in a

region called the blanket. These heated structures are then cooled using a flowing pressurized gas. Similar to conventional power plants, the resulting hot gas is used to drive turbines that finally produce electricity.

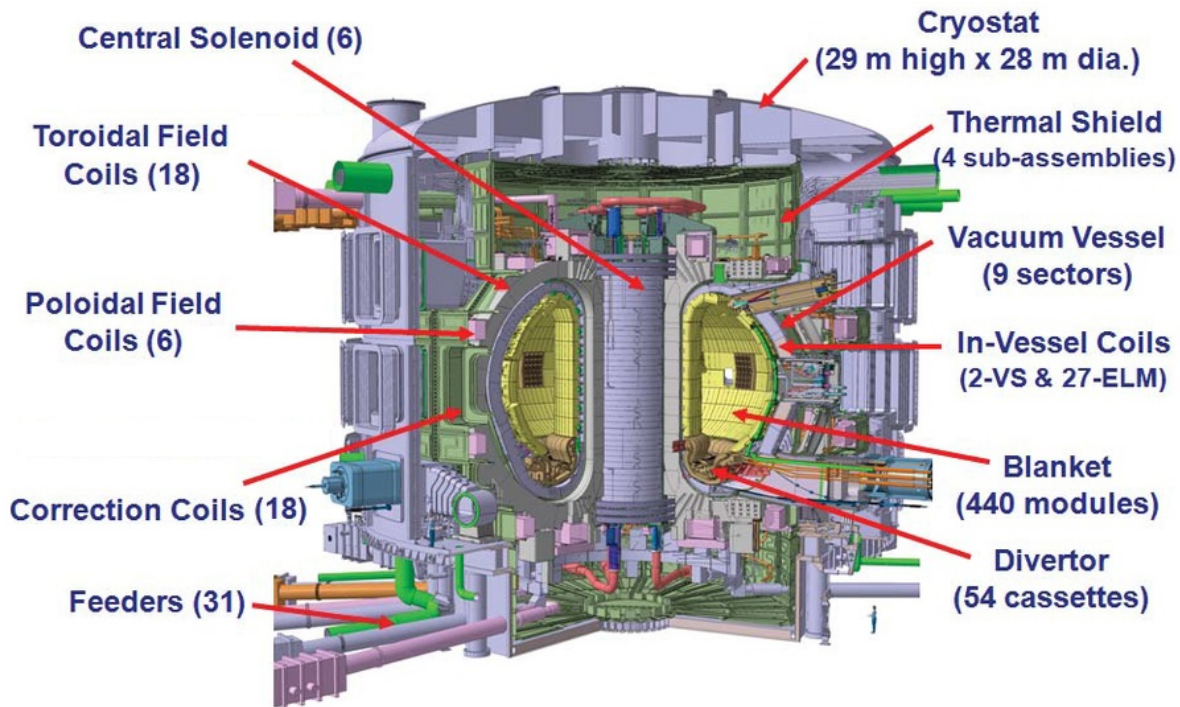


Figure 1.2: Schematic of the ITER tokamak device depicting fundamental components such as field coils, central solenoid, vacuum vessel, blanket module, and divertor [2]. The modular design allows for individual component replacement over the lifetime of operation.

The diagram in fig. 1.2 highlights the primary components of the tokamak design for the International Thermonuclear Experimental Reactor (ITER) [2]. This particular device is under construction and exemplifies the culmination of tokamak research and design to date. The primary goal is to demonstrate the high energy gain ($Q=10$) and perhaps ignition is possible for short time scales of up to twenty minutes. A hydrogenic plasma will be confined by multiple magnetic field coils within the center of the toroidal vacuum vessel. The large magnetic fields needed to confine the plasma require superconducting coils and thus the device is housed within a cryostat to thermally insulate the coils. Because of cross-field plasma transport processes, the edge of the plasma will come into contact with the first wall and divertor regions of the device.

Fig. 1.3 depicts a cross sectional cutaway of the torus. The first wall consists of modules that act to shield the rest of the device from the large heat flux produced in the plasma core. Future reactors will need to produce additional T fuel through breeding in a lithium (Li) blanket that surrounds the first wall. In order to actively remove heat and the He produced in the fusion reaction, the plasma is guided to strike a divertor region. The first wall and especially the divertor will be subjected to the most extreme conditions any tokamak component will face. The accurate prediction of the sustainability of the materials used in the first wall and divertor in a fusion environment is critical to a viable commercial fusion reactor.

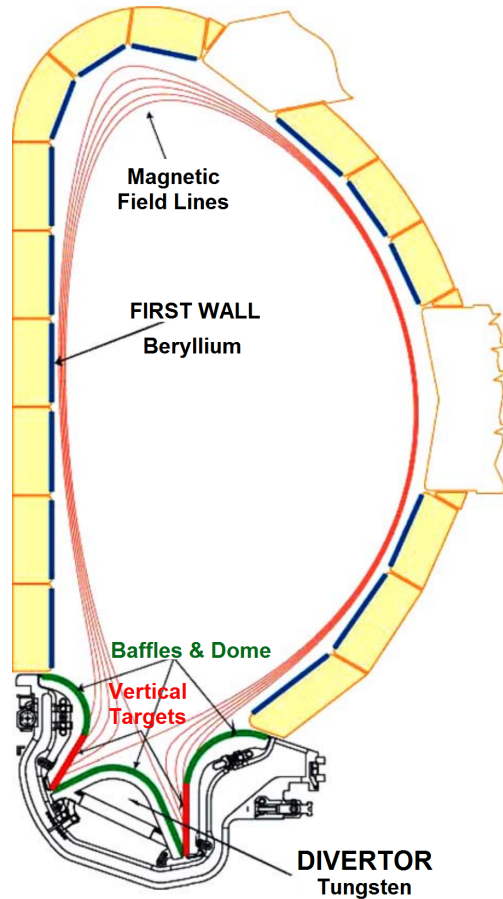


Figure 1.3: The ITER design uses a beryllium wall in the main plasma chamber, and a tungsten divertor [55] (adapted). The divertor consists of replaceable cassettes. The nested lines are magnetic field contours. The confined plasma is bounded by the separatrix, which is the last field contour that is closed (i.e. does not intersect a material surface).

1.3 Plasma-Material Interactions

As previously described, the first wall and divertor materials will be exposed to extreme conditions making the subject of Plasma-Material Interactions (PMI) a critical research area for sustained operation of a fusion reactor. The accumulation of tritium (T) within Plasma Facing Material (PFM) presents both a safety issue and inhibits fuel cycle sustainability. The simplified model of PMI shown in fig. 1.4 depicts a ballistic ion impact on a perfectly ordered crystal lattice. If the projectile ion has enough kinetic energy, the target lattice atom will be ejected into the plasma as an impurity. This impurity may act as a highly charged ion in the core plasma, which collides with hot plasma electrons and in turn radiates power away from the core plasma via bremsstrahlung radiation. This radiation loss is compounded with high-Z impurities such as W-based first wall and divertor materials. A much more realistic PMI model would also include the complex, synergistic, and multi-scale processes shown on the right hand side of the same figure, explained in what follows.

In addition to surface effects, particles in solution within the PFM (i.e. between lattice sites) may diffuse throughout the material. These diffusing particles may become trapped when encountering defects (e.g. grain boundaries, impurities, and vacancies). If unburned T nuclei become permanently trapped within the wall material, the overall T-particle generation balance is negatively impacted. Published estimates [54] show that if the probability of permanent trapping of T in the wall material exceeds 10^{-6} then it will become difficult or impossible to produce a self-sustaining T fuel breeding system. These considerations form the essential motivation for the focus of this work - a study of how defect sites induced by energetic particle bombardment act as traps to all the solute fuel and product species (i.e. D, T, and He).

Critically important processes occur at the PMI interface. In addition to the sputtered impurity atoms reaching the plasma core, impurities are also likely to redeposit on another PFM surface. This redeposition can cause a mixing of materials and form a randomized structure high

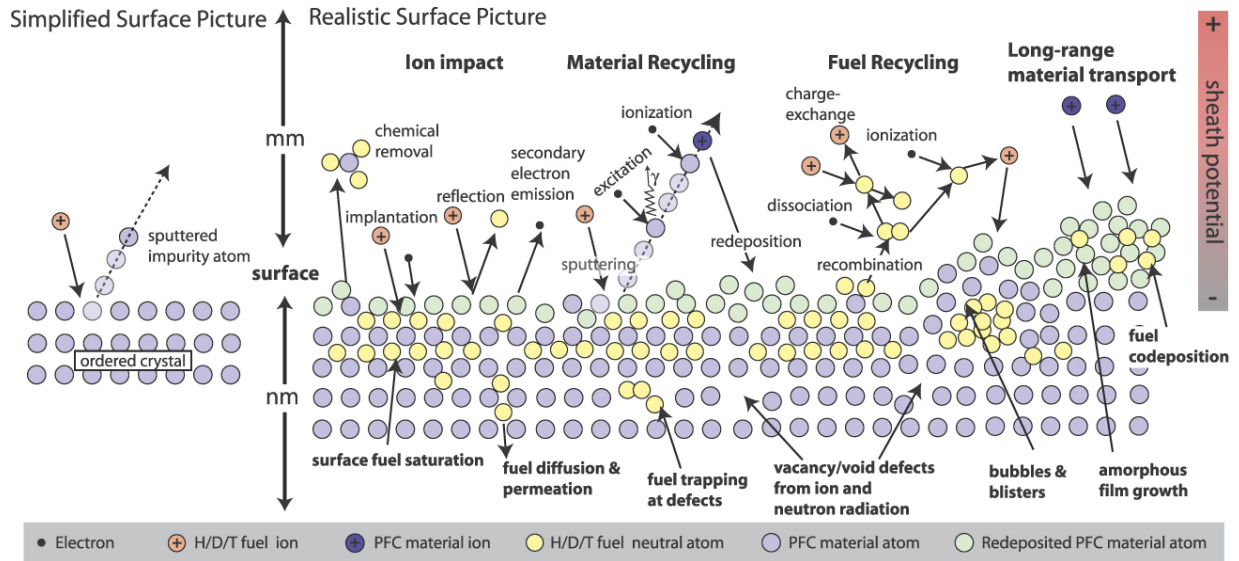


Figure 1.4: Schematic illustration of the complex, synergistic, and inherently multi-scale surface interactions occurring at the material surface in a realistic magnetic fusion plasma environment [57]. H, hydrogen; D, deuterium; T, tritium; PFC, plasma facing component; γ , gamma ray.

in defect concentration. If this process occurs in the presence of hydrogen ion deposition, it may significantly enhance hydrogenic isotope retention through co-deposition of these isotopes into the redepositing material layers and lead to the buildup of a fuel reservoir. While this reservoir may prove stable during steady state operation, various disruption events may lead to an uncontrolled release of fuel. Alternatively, if this trapped fuel is permanently sequestered, then the overall T fuel production cycle is negatively impacted, and an inventory of radioactive trapped T can build up within the device.

The realistic surface picture of fig. 1.4 depicts the penetration of plasma-fuel ions and subsequent diffusion in the PFM. Within the lattice structure a solute atom encounters various potential barriers as shown schematically in fig. 1.5. When trapped at an interstitial site, thermal vibrations can give trapped atoms enough kinetic energy to overcome the activation energy needed for diffusion (E_D) and thereby move into solution and begin to diffuse in the material. Since the lattice is not perfectly ordered, eventually a solute atom can encounter a defect in the lattice. These defects effectively act as trap sites for the solute atoms within a potential well. The

activation energy required to enter the defect site is the trapping energy (E_{tr}). Once trapped, the detrapping energy (E_{dt}) required to release from the defect is the sum of the binding and trapping energies ($E_b + E_{tr}$). Clearly, deep traps (i.e. high detrapping energy) can then become effective reservoirs for trapped atoms which would then need to acquire a high kinetic energy in order to escape from the trap.

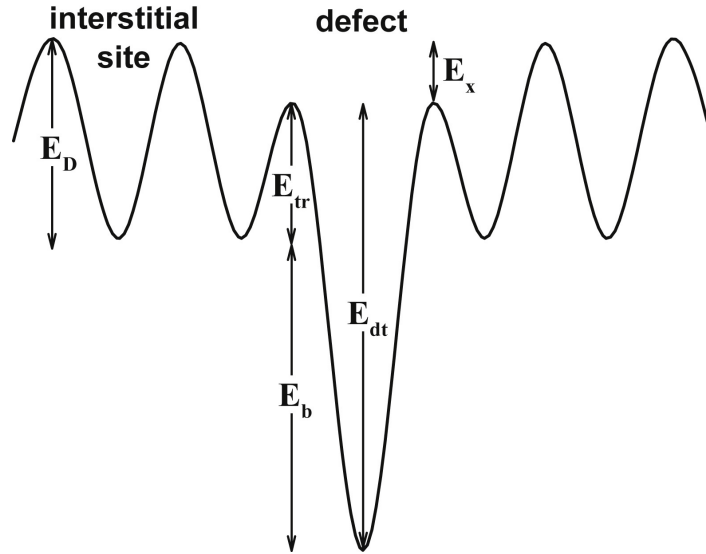


Figure 1.5: Potential energy diagram for trapping of D atom in a metal lattice [61]. Potentials shown are the energies for detrapping (E_{dt}), binding (E_b), trapping (E_{tr}), diffusion (E_D), and the difference between trapping and diffusion (E_x).

The types of defects within the lattice structure of the PFM vary. The simplest defects are either a mono-vacancy or interstitial. Assuming a regular lattice structure without any defects, a mono-vacancy results when one lattice atom is removed. Vacancies may grow into vacancy complexes with the additional removal of lattice atoms or agglomeration through vacancy migration. Typically when these complexes become large enough to resolve with an electron microscope they are called voids. Converse to vacancies, a self-interstitial atom (SIA) is an extra lattice atom placed between normal lattice points and can grow with additional SIA. Both vacancies and SIA may form structures known as dislocations in which the lattice structure may slip or glide into a more energetically favorable state. The regularity of the lattice structure is broken in this region and a boundary of two or more lattice structures are formed at the dislocation.

In addition to hydrogenic isotope retention, various defects may affect fundamental material properties. For instance, a high defect density can effectively change the propagation of heat flux through the material by reducing thermal conductivity as shown by Cui *et al.* [13]. The result could lead to increased surface temperature and a larger temperature gradient, further stressing the material. In addition, the exposure of He to PFM has shown the development of fuzz-like structures under certain conditions as shown by Baldwin *et al.* [6] in fig. 1.6. The significantly changed surface layer has been shown to retard the diffusion of hydrogenic isotopes and reduce overall retention. The impact of transient events in producing W dust is still under investigation. Characterizing and quantifying these synergistic and multi-scale effects are critical to the engineering requirements to estimate the steady state operation and lifetime of PFM components.

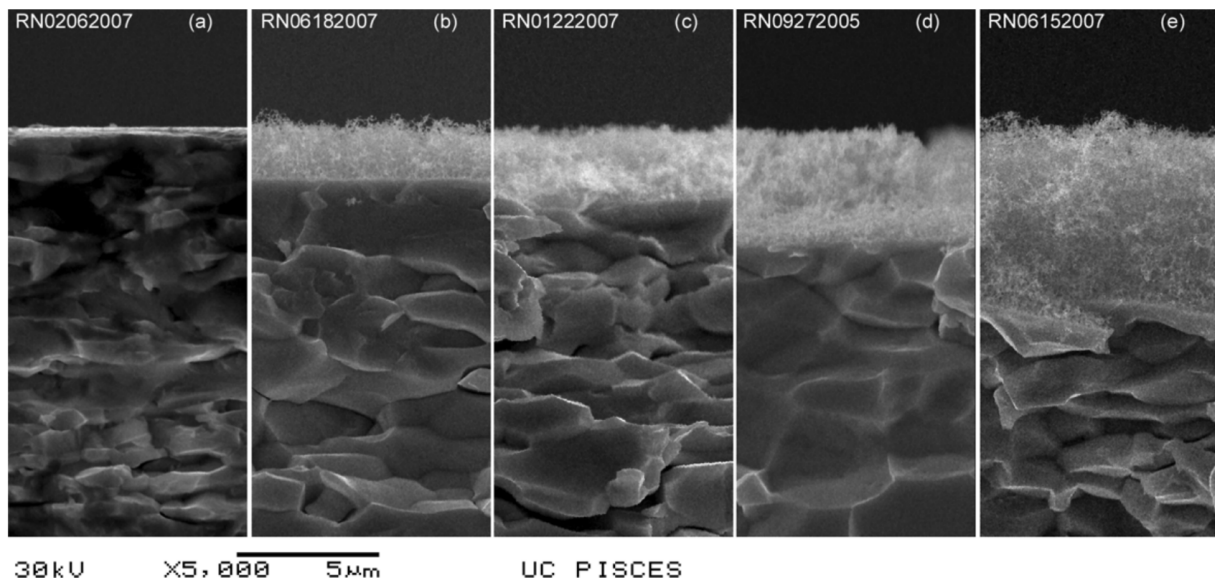


Figure 1.6: Cross-sectional Scanning Electron Microscope (SEM) images of W targets exposed to pure He plasma at 1120 K for exposures times of (a) 300 s, (b) 2.0×10^3 s, (c) 4.3×10^3 s, (d) 9.0×10^3 s, and (e) 2.2×10^4 s [6]. Fuzz-like tendrils develop on the plasma facing surface at high surface temperatures and increasing He fluence.

1.3.1 Neutron Damage

The energetic neutrons produced in the D-T reaction will leave the plasma core and reach the PFM virtually unimpeded. Within the material the neutron only interacts with the nuclei of lattice atoms. The interaction may result in a neutron capture event, transmuting the target atom and creating a heavier isotope which may then undergo radioactive decay. In addition to changing the microstructure of the lattice and introducing impurities, neutron-nucleus collisions also impart kinetic energy to the target atom. In the zone close to the surface, the neutrons still retain nearly their original 14 MeV kinetic energy; a collision between these energetic neutrons and a target nucleus is then likely to displace the target atom creating a mono-vacancy and SIA, also called a Frenkel pair. Furthermore, the recoiling target atom can create additional lattice atom displacements and cause a cascade of defect inducing events. These defects accrued by the energetic collisions act as trap sites and lead to significantly increased H isotope retention. In addition to the radiological concerns from neutron irradiated PFM, the increased T inventory further activates the PFM and can have a critical effect on tritium fuel self-sufficiency.

1.3.2 Impact to Tritium Fuel Cycle and Inventory

The accurate accounting of T fuel is essential to both the maintenance of the fuel cycle as well as for engineering safety [47]. The successful operation of a fusion reactor relies on the continuation of the fusion reaction. Equal amounts of D and T are needed in the D-T reaction. While D is a stable isotope and relatively plentiful on Earth, T is rare partially due to a ~ 12.3 year half life. A proposed breeding source of T involves the neutron capture in lithium (Li) shown in eq. 1.2. The purification and reintroduction of T into the core plasma is still a topic of active research. As such, the probability of permanent loss of T fuel in the system during operation must be below 10^{-6} to achieve a closed fuel cycle [54]. Additionally, the radioactivity of T is a safety concern for nuclear regulatory bodies. The previously mentioned ITER has an upper limit

of 1 kg of allowable T retention within the entire device, where 700 g are reserved for PFM [39]. The plot shown in fig. 1.7 depicts the predicted operational time needed to reach this site limit for various PFM choices in ITER. Thus developing a clear understanding of all the mechanisms and conditions that affect fuel retention is key to developing models of the accumulation of T in PFMs, and for determining the lifetime and feasibility of particular PFM choices used in ITER and future fusion reactors.

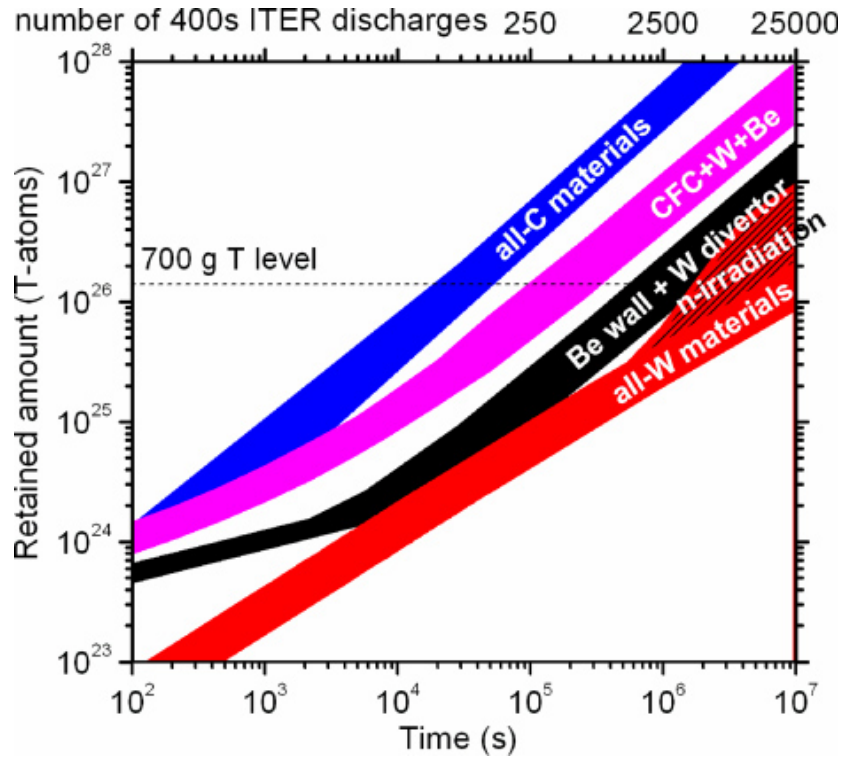
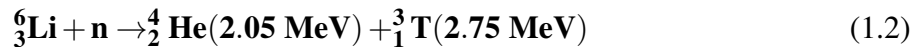


Figure 1.7: Roth *et al.* [39] assessed previous experimental data on various PFM to predict the overall component lifetime due to T retention. Note that with a 700 g T limit, W has the lowest retention and longest overall lifetime. Carbon (C), Carbon Fiber Composite (CFC), Beryllium (Be), and Tungsten (W) are shown.



These considerations then provide the primary motivations for this work, which presents three primary results. First, we experimentally determined that the annealing of damage in high temperature W during irradiation occurs at a high enough rate to virtually eliminate the increased

retention of plasma-implanted fuel ions associated with energetic particle displacement damage. Second, we developed a technique to extend the use of an existing T-fuel trapping model to the experimentally relevant case where a large number of distinct trap energies exist. Using this modified model together with a new experimental technique, introduced here for the first time and involving sequential thermal desorption and nuclear reaction analyses at progressively higher temperatures, we then inferred the existence of a low density uniform distribution of low-energy (< 1.4 eV) intrinsic traps, a near-surface (< 100 nm) intermediate energy (1.3-1.4 eV) trap population that appears to be produced by plasma irradiation, and a high energy (1.4-2.0 eV) trap population that coincides with the position of the induced displacement profile produced by energetic particle collision cascades.

Chapter 2

Experimental Methods

2.1 Tungsten (W) as a Plasma Facing Material (PFM)

Currently, W is the primary PFM candidate for the first wall and divertor armor in the first energy-producing D-T devices due to its high melting point, low H isotope retention, and resistance to sputtering [47]. Though these favorable characteristics reduce the likelihood of W entering the core plasma, disruption events are expected since current devices are still being tested and operating parameters adjusted. Therefore some amount of PFM will ultimately be eroded and entrained in the non-quiescent plasma environment. The high atomic number (Z) of W can lead to multiply ionized excited states that can then emit x-rays and act as a route for energy to escape the plasma, lowering the core temperature, and impeding fusion. To avoid this issue in ITER, the first wall will have a Beryllium (Be) coating due to its low Z , relatively high melting point, and high O_2 gettering [39]. A Be-based first wall can be used in ITER because of the relatively short overall plasma durations and low duty cycle of the device; subsequent D-T based energy producing prototype reactors would have to have higher duty cycle and thus Be is not an option for use there. As shown in fig. 2.1, PFM candidates display erosion rates that decrease with increasing atomic mass. Though Be presents a lower loss of power, the higher erosion rate,

as well as the inherent toxicity when it is formed in micron-sized particles ensures that W-based materials will likely be used in a steady state operating and energy producing commercial reactor. Lastly we note that carbon based PFM designs have been shown to have very high hydrogenic isotope retention and effectively eliminated from consideration as shown in fig. 1.7.

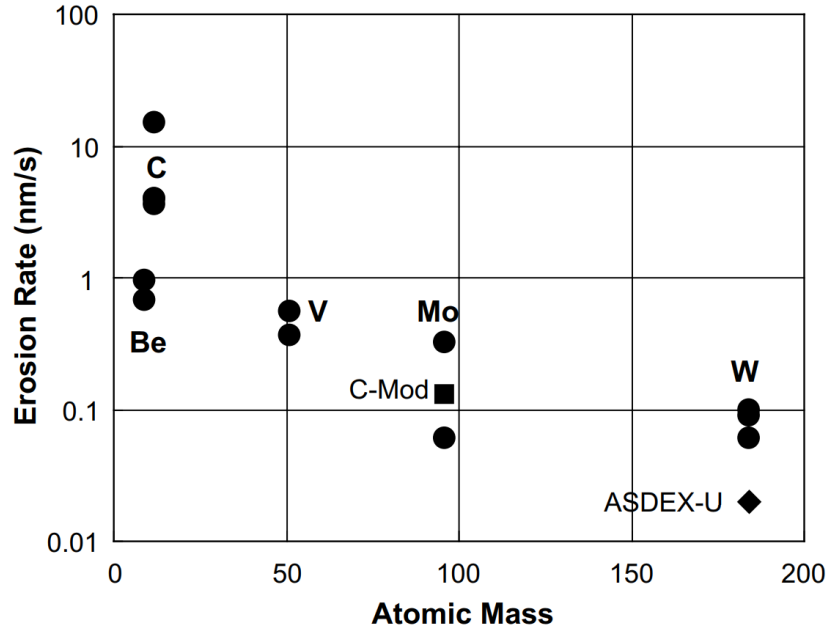


Figure 2.1: Wampler *et al.* [55] presented various erosion rates for PFM candidates. Note the erosion rate is negatively correlated to atomic mass. Hence W presents the lowest erosion rate. Erosion rates measured for various materials at the outer strike point in DIII-D (circles), for Mo at the outer strike point in C-Mod (square) and for W in ASDEX-Upgrade (diamond) on the center column.

2.2 Laboratory Devices to Mimic Fusion PMI Environments

Multiple machines are needed in order to replicate and control fundamental PMI conditions a PFM will encounter in a fusion reactor. Linear plasma-based devices provide a cheaper and more cost effective testing environment for many aspects of fusion PMI. While some experimental campaigns place PFM samples directly inside a tokamak, future fusion reactors will be significantly larger and operate in regimes unreachable by current tokamak devices. Furthermore, fundamental properties of PMI (e.g. ion energy and composition, surface temperature, ion flux and

fluence) are more easily adjusted and varied within a linear device. Some aspects of displacement damage from energetic neutrons can be simulated with energetic (i.e. ~ 0.1 to 10 MeV) ions.

2.2.1 Plasma Devices

The Plasma Interaction Surface Component Experimental Station (PISCES) program utilizes multiple steady state plasma devices. Previous experiments on W performed within the PISCES group utilized both the higher flux PISCES-A device [21] and the PISCES-E device. While the relatively low flux of PISCES-E requires longer exposure times to achieve a given fluence, the resulting plasma parameters have less variability. That is, a longer exposure is more forgiving in variations in exposure time and ensures the initial heating of the sample is a smaller fraction of the total exposure time. The lower ion flux also results in less heat flux to the sample and the resulting sample temperature is more easily controlled. Lastly, after proper conditioning of the main chamber with D₂ plasma, the ion flux is highly repeatable and easily controllable in PISCES-E.

The PISCES-E device, a plasma etcher with a 13.56 MHz RF source, was thus chosen to decorate defects in W samples with D. A schematic of the etcher is shown in fig. 2.2 and operation is further detailed in [51]. The process chamber has a base pressure near 10^{-5} Pa and during plasma operation a typical neutral pressure of 0.7 Pa. An interlock chamber houses an air cooled and electrically isolated sample manipulator that can be inserted into the main chamber. A K-type thermocouple in contact with the rear of the sample measures the temperature. The manipulator was typically biased -100 V relative to the chamber wall potential to increase the ion energy incident on the plasma facing surface and implant ions within the first few monolayers of the sample. An RF compensated Langmuir probe typically measured a flux of 10^{20} ions/m²/s uniformly across the surface of the sample holder. During plasma exposure the probe was positioned to the side of the sample. A total fluence of 10^{24} D/m² and took on average approximately one hour. Using an Electrostatic Quadrupole Plasma (EQP) particle analyzer,

the molecular ion concentrations were found to be 0.72, 0.06, and 0.22 for D^+ , D_2^+ , and D_3^+ respectively [58] for the conditions of our experiments.

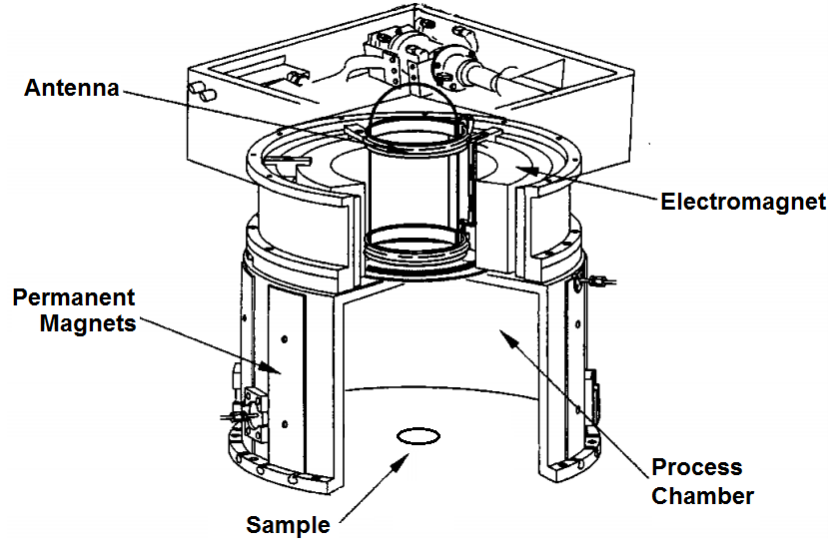


Figure 2.2: Schematic for the major components of the MØRI™ - 200 RF plasma source [53]. An azimuthally symmetric helicon wave is excited by the antenna structure and propagates axially along the diverging magnetic field lines into a field-free downstream bucket. The shape of the diverging magnetic field can be controlled with the two coils.

2.2.2 Ion Accelerator

As described earlier, in lieu of neutron damage, an ion source is used to accelerate and implant energetic heavy-ions into W samples. In addition to heavy-ion damage, $^3\text{He}^+$ was also used for NRA measurements and further discussed in the next section. Whereas neutrons produce damage uniformly throughout the material, energetic ions are slowed by Coulomb interactions and penetrate a finite distance. Multiple factors including projectile ion energy and species as well as target lattice species influence the damage produced as a function of depth. The software Stopping and Range of Ions in Matter (SRIM) numerically calculates this damage profile using a binary collision approximation [62]. The damage is quantified by the number of lattice atoms displaced, where only lattice atoms imparted with energy above a threshold displacement energy are counted. The displacements per atom (dpa) accounts for the initial incoming ion hitting a

lattice target as well as the possible cascade of displacements that can occur when the lattice target atom is mobilized. Per Stoller *et al.* [48], the Quick Kinchin-Pease option and a displacement damage threshold of 90 eV for W were used to calculate dpa.

Heavy ion damage was performed in either Los Alamos National Laboratory or the Max-Planck-Institut für Plasmaphysik, Garching. Multiple beam energies in the MeV range were chosen to produce damage profiles peaked near or below 1 μm . For various practical reasons, including the steering of the ion beam, copper (Cu) was chosen to create displacement damage. In each laboratory, the Cu ion beam was rastered over the entire plasma facing surface of the W sample. In general, the ion beam community follows the practice recommended by ASTM [15] when performing ion irradiations. Specifically, it recommends to use a defocussed ion beam to avoid periodic local flux variations artificially introduced when rastering a beam. However, it is also a common challenge to produce a uniform irradiated sample with the defocussed beam. We chose the rastering beam to produce a relatively large damaged sample size with excellent lateral uniformity.

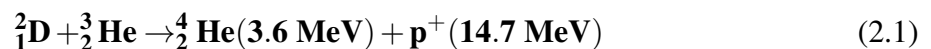
2.3 Trapped D Measurements

The primary experimental techniques for studying hydrogenic retention in W are Nuclear Reaction Analysis (NRA) and Thermal Desorption Spectroscopy (TDS). NRA is a relatively nondestructive technique that probes the D concentration up to several microns in depth. This technique does not differentiate as to which type of trap holds the D, nor if it is in solution between lattice sites, but can infer the spatial distribution of D contained within the material. TDS is a partially destructive technique wherein the sample temperature is linearly increased and the surface flux of desorbed D is measured as a function of temperature. The process of heat treatment to the sample not only causes D desorption but may change the lattice structure through partial annealing of defects. The flux of D from the sample is complicated by the multi-step

migration process of diffusion, trapping, release, and eventual surface recombination needed to escape the sample. By modeling these coupled processes, TDS can reveal the energy required to escape a given trap. The release behaves as an Arrhenius process, in that an atom is trapped within an energy barrier (E_{dt}) and may escape once the atom acquires enough kinetic energy via random collisions. Both the NRA and TDS data can be directly compared by quantifying the total D retention.

2.3.1 Nuclear Reaction Analysis

Typically low Z impurities implanted within materials are studied with NRA. A nuclear reaction is chosen to isolate and quantify the presence of a particular impurity within a material sample. In general ion beam analysis techniques may not be viable for activated samples, nor can they be used on a material that also significantly reacts with the probing ions, as those reactions may dominate over reactions with implanted atoms. The measurement of D in many materials, including W, relies on the $D(^3\text{He},p)^4\text{He}$ nuclear reaction shown in eq. 2.1. NRA for this reaction is well developed and has well separated product ion energies. Under high vacuum, a W sample is implanted with high energy ^3He ions that can overcome the Coulomb barrier and reach the nucleus of a target D impurity. Contaminants on the sample surface or other impurities within the material may also react with ^3He . For instance carbon (C) produces energetic protons via $^{12}\text{C}(^3\text{He},p_{0,1,2})^{14}\text{N}$ and $^{13}\text{C}(^3\text{He},p_{0,1,2})^{15}\text{N}$ reactions. This additional signal can be minimized by maintaining good vacuum practices, utilizing high purity W samples, and thoroughly cleaning the sample surface prior to plasma exposure.



The less massive proton is imparted with the majority of the exothermic energy and can escape from deeper in the material (up to $\sim 10 \mu\text{m}$). The relatively more massive α receives less

of the excess energy after the reaction and loses more energy traversing the same distance (i.e. higher stopping power), only allowing it to escape the W sample if located relatively close to the surface ($\sim 0.1 \mu\text{m}$). As such, alphas can only be used to probe the near surface making proton detection the primary focus of NRA. The thickness of the sample requires the position of the detector on the same side as the probing beam, as seen in fig. 2.3. To optimize the depth probed by NRA, the incident ^3He probing beam is normal to the surface with an initial energy E_0 . A small fraction of all escaping protons are measured with a solid state detector located at a 135° reaction angle per Mayer *et al.* [28]. A thin stopping foil selectively impedes more massive or less energetic particles (e.g. reflected ^3He) while also slowing protons enough to eventually stop within the detector. To ensure only particles within a specific solid angle reach the detector, a dense shield selectively blocks particles outside the slit's line of sight.

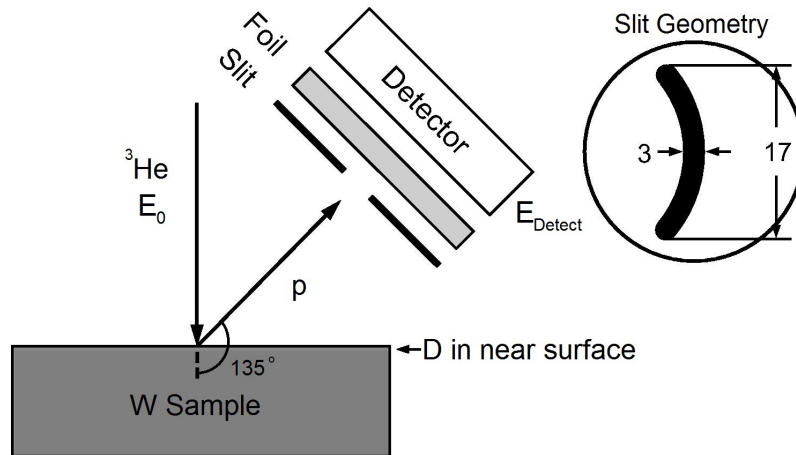


Figure 2.3: The geometry of the sample, detector, and 3 mm wide slit shielding are shown in the schematic [28] (adapted). The probing beam with initial energy E_0 is normal to the W surface. The detector was located 135° relative to the incident beam and ~ 42 mm away, from sample to shield center.

A D concentration profile as a function of depth can be inferred from the analysis of the energy spectra for either or both of the product ions. An NRA measurement consists of a controlled, nearly mono-energetic ^3He ion beam inducing nuclear reactions and measuring the energies of the resulting product ion species that escape the material and reach a solid-state detector. Energetic product ions that penetrate the solid-state detector lose energy through inelastic

collisions that create electron-hole pairs in the ion's wake. In response, a current is induced to neutralize the charged detector depletion zone. The height of the measured current pulse is proportional to the ion's kinetic energy. Accurate measurement requires a depletion zone longer than the stopping range of the detected product ion. The finite resolution of the detector and analog to digital converter determine the detected energy width (δE) for each bin (i) spanning E_i to $E_{i+1} = E_i + \delta E$. As explained in more detail below, the depth of the nuclear reaction (and thus of the measured D atom) is correlated to the detected ion energy and the width of each energy bin corresponds to a particular depth range (i.e. x_i to x_{i+1}) through a multi-step process.

The kinematics of the nuclear reaction and resulting product ion energy can be expressed in terms of the instantaneous ^3He energy (E_1), just prior to the nuclear reaction. The notation for the reaction particles are as follows: "1" denotes the projectile ^3He , "2" the target D, "3" and "4" the product ions where "3" specifies the particle that reaches the detector. In what follows, the proton is particle "3." Since the detector reaction angle (θ), particle masses (M_j), and exothermic energy (Q) released are all constants, the product ion energy immediately after the nuclear reaction (E_3) only varies with instantaneous energy (E_1) as shown in eq. 2.2. Note that of the two possible E_3 values (i.e. the \pm after the cosine), the negative term in eq. 2.2 is unphysical and neglected for the initial energies considered here.

$$E_3(E_1) = E_1 \frac{M_1 M_3}{(M_1 + M_2)(M_3 + M_4)} \left[\cos \theta \pm \sqrt{\frac{M_2 M_4}{M_1 M_3} \frac{Q}{E_1} \left(1 + \frac{M_1}{M_2} + \frac{E_1}{Q} \right) - \sin^2 \theta} \right]^2 \quad (2.2)$$

The nuclear reaction itself is only one of several processes that determine the energy of the product ion that reaches the detector. An energetic ion within a material loses kinetic energy due to inelastic Coulomb collisions with electrons and nuclei. The sum of the so-called electronic and nuclear stopping powers (dE_s^m/dz) quantifies the energy a particular ion species (s) loses within the material (m) as a function of path length. The initial energy (E_0) is reduced as the ^3He ion penetrates the material along a path length (z), where the nuclear reaction occurs. In addition

to energy lost to the material in order to reach the target D, the products of the nuclear reaction also lose energy to the W lattice while escaping the material. Note that the stopping power is both ion mass and energy dependent, leading to an asymmetry in energy lost by ^3He entering the W lattice and a product ion exiting. Lastly, note that there may be an additional thin stopping foil placed in front of the detector that further reduces the proton energy.

The aforementioned software package SRIM [62] is used to calculate the stopping power for the incident and exiting ions moving through the relevant material lattice. The initial energy is reduced to the instantaneous energy in eq. 2.3 by the stopping power integrated over the particle penetration path. Choosing to implant ^3He normal to the surface maximizes the penetration depth, optimizes the resolution, and minimizes the path length by setting $z = x$, where x is the depth perpendicular to the surface in which a nuclear reaction occurs. The detector position dictates the path length for the product ion, setting $z = x/\cos(\theta)$. No further energy is lost in vacuo, but the thin foil stopping power must also be accounted for to calculate the final energy detected.

$$E_{instant}(E_0, z) = E_{initial} - \int_0^z \frac{dE_s^m}{dx} dz' \quad (2.3)$$

The ^3He energy prior to the nuclear reaction (E_1) and the detected proton energy (E_{Detect}) are plotted as a function of depth in fig. 2.4. E_1 (dashed lines) is needed to convert the energy dependent nuclear reaction cross section shown in fig. 2.5 for each initial energy. E_{Detect} (solid lines) takes into account the stopping power along the entire path within the W lattice and foil as well as the energy gained from the reaction. Note that with increasing initial energy, the maximum probing depth increases. The inverse kinematics is displayed in which the detected proton energy increases with depth (i.e. lower ^3He energy). Lastly, the slope of the detected energy with respect to depth limits the ultimate depth resolution. That is, if the detected energy for multiple depths is nearly the same (e.g. a slope near zero), the origin of the reaction can not be well resolved. For instance, the 3.5 MeV initial energy has a lower slope and poor resolution below $3 \mu\text{m}$ and a

higher slope and better resolution above 5 μm .

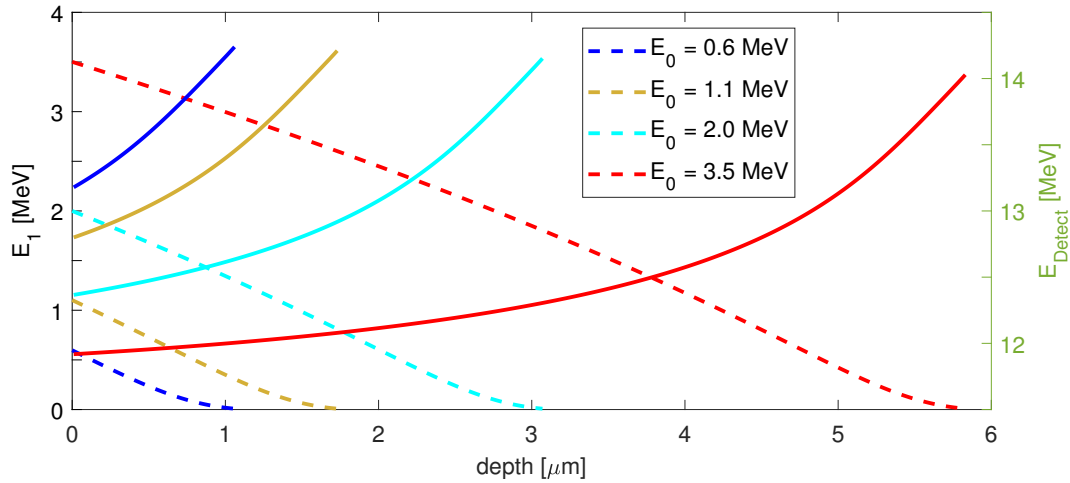


Figure 2.4: The instantaneous (dashed lines for E_1 on the left axis) and detected proton energies (solid lines for E_{Detect} on the right axis) are plotted with respect to nuclear reaction depth (x) for various initial probing energies (E_0). The energies depicted are dependent on the $\text{D}(^3\text{He},\text{p})^4\text{He}$ nuclear reaction, a ^3He beam incident normal to the sample surface, and a detector located at a reaction angle of 135° .

Next, the probability of a nuclear reaction to occur is needed. The $\text{D}(^3\text{He},\text{p})^4\text{He}$ nuclear reaction cross section as a function of energy is independent of material and well studied [60]. In the center-of-mass frame, the angular distribution of the nuclear reaction product ions is isotropic in space. Switching to the lab frame with a stationary D target, the product ion energy has an angular dependence as seen by the reaction kinematics outlined previously by eq. 2.2. The reaction cross section ($d\sigma/d\Omega$) is dependent on the instantaneous ^3He energy ($E_{instant} = E_1$) just prior to the nuclear reaction. The cross section as a function of energy for the detector reaction angle ($\theta = 135^\circ$) is shown in fig. 2.5, peaking near 0.6 MeV.

An example D concentration and several nuclear cross sections are plotted as a function of depth in fig. 2.6 (a). Though the D concentration is an unknown quantity, the inferred result is plotted here for discussion purposes. Note that the D concentration (shaded black) is shown only as a function of depth whereas the cross sections (dashed) are a function of both initial energy and depth. For an initial ^3He ion energy of 0.6 MeV, only the near surface is probed, thereby constraining the origin of nuclear reaction products produced with such a beam energy.

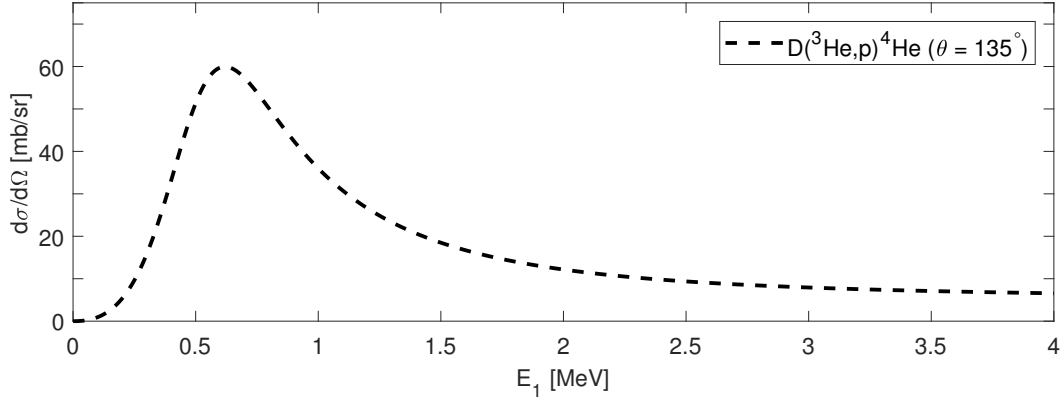


Figure 2.5: The nuclear reaction cross section for the $D(^3\text{He},p)^4\text{He}$ reaction collected at a detector reaction angle of 135° [60]. The cross section is peaked for an incident ^3He beam energy near 0.6 MeV. Note that the x-axis is the instantaneous ^3He energy (E_1) when the nuclear reaction occurs.

By increasing the initial ^3He probing energy, the cross section as a function of depth can be effectively shifted further into the material. That is, increasing the probe energy moves the peak cross section further into the material. Note that the region near the peak cross section will have a higher probability of a nuclear reaction occurring, increasing the countable events from that region. Thus multiple ^3He ion probing energies can be utilized to properly resolve the D concentration as a function of depth.

Shown in eq. 2.4, the product ion yield per detector energy bin (Y_i) is defined by the probability (P_i) of the nuclear reaction to occur. The probability is proportional to the product of the cross section and D concentration (C_D). That is, the yield simply reflects the likelihood of hitting a target D atom and the abundance of the D targets. Note that the cross section is a function of E_1 .

$$Y_i(E_0) \propto \int_{x_i}^{x_{i+1}} P_i(E_0, x) dx = \int_{x_i}^{x_{i+1}} C_D(x) \frac{d\sigma(E_1(E_0, z(x)))}{d\Omega} dx \quad (2.4)$$

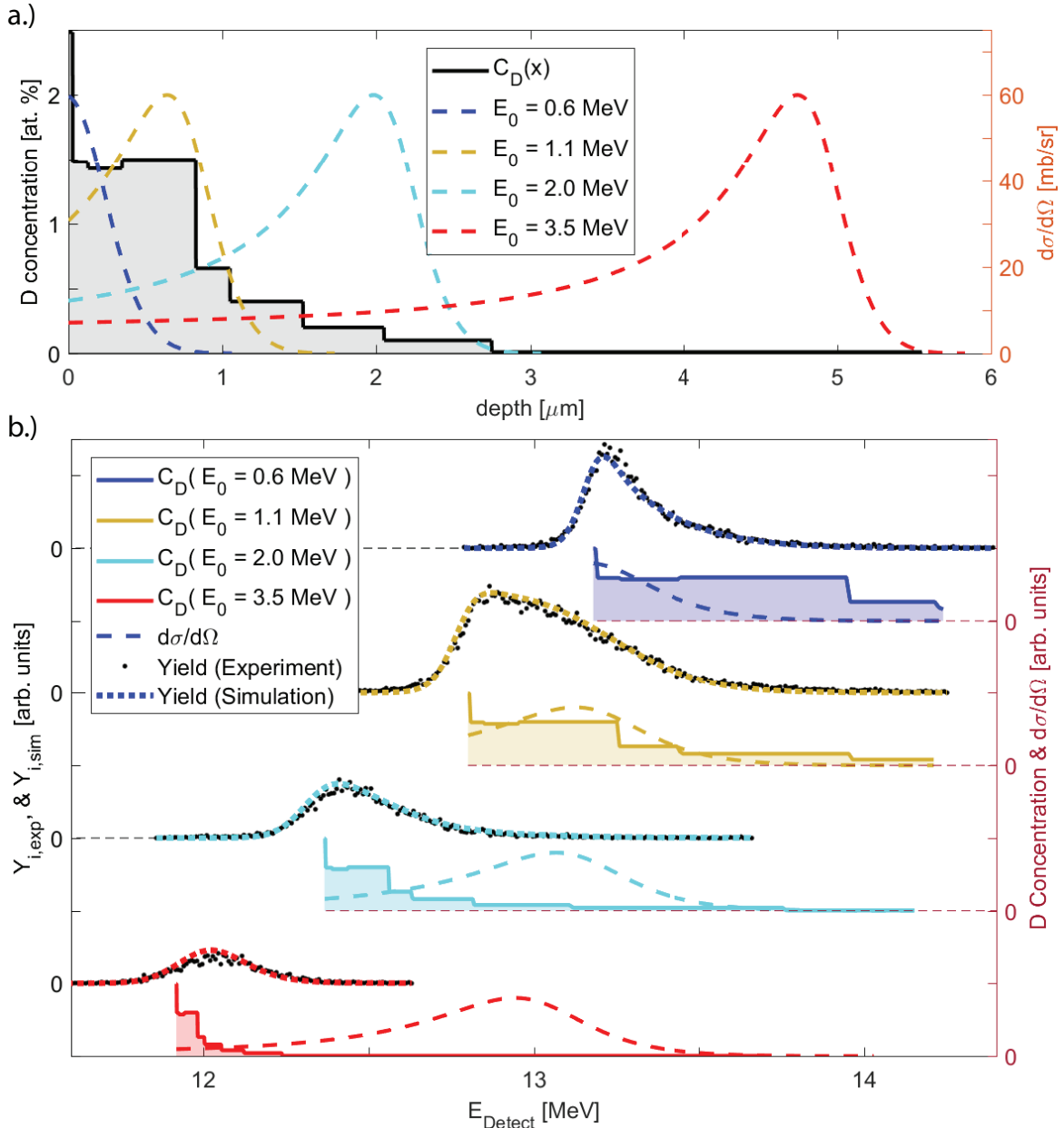


Figure 2.6: NRA data from a heavy ion damaged (up to $0.9 \mu\text{m}$) and D exposed W sample is shown. a.) D concentration (solid and shaded) and cross sections (dashed) for various initial energies are plotted with respect to depth. b.) Both the D concentration (solid and shaded) and cross sections (dashed) are plotted with respect to detected energy (offset by 2 arb. units). In addition, the experimental and simulated yields (Y_i) are plotted (offset by 1 arb. unit).

Using the detected energy to depth relation plotted in fig. 2.4, the same D concentration and nuclear cross sections are plotted from fig. 2.6 (a) as a function of proton energy detected (on the right axis) in fig. 2.6(b). In addition, experimental and simulated yields (on the left axis) for

each initial energy are plotted. Arbitrary units are used for the y-axis and various initial energies are offset and color-coded for clarity. The D concentration (shaded) is now shown to change as a function of initial energy. Note that increasing initial energy (culminating in red) reduces the resolution of the near surface D concentration as it shrinks in energy space. Conversely, the lowest probing energy (blue) is distinctly sensitive to the near surface D concentration. The experimental yield (black dots) and simulated yield (thin dashed) are proportional to the product of the D concentration and cross section for each initial energy as shown in eq. 2.4. Note that these yields do not display a one-to-one correspondence. That is, the experimental yields are broad compared to the D concentration and cross sections. Experimental uncertainties must be accounted for to broaden the detected energy and attain the simulated yield as explained in what follows.

Ideally, the probing particles do not deviate in any way during the previously explained multi-step process between the ^3He probing beam and proton detection. In reality, multiple sources of error (e.g. straggling) may arise due to the increased path length or deviation in energy for any particle in the multi-step process. For instance, straggling may occur due to multiple small angle scattering events that results in an increased distance traversed within the material, as well as the spread of both the energy and outgoing path direction. Geometric straggling is due to the finite slit size and finite beam spot size. While the shielded slit geometry significantly reduces geometric straggling, further decreasing of the slit width reduces sensitivity (i.e. the amount of detected protons). In addition to energy loss, statistical fluctuations associated with energy transfer during inelastic collisions broaden the energy distributions of the ions traversing the W lattice. This so-called energy loss straggling significantly limits the resolution of NRA measurements deeper into the sample. Mayer developed the software SimNRA to perform the transformation of the ideal yield in eq. 2.4 to a realistic yield ($Y_{i,sim}$), detailed below, that accurately reflects experimental measurements ($Y_{i,exp}$).

2.3.2 NRA analysis programs

Two software programs were employed to analyze the detected product ion energy distributions for various ^3He ion beam energies. SimNRA was used to calibrate and simulate the product ion energy spectra produced from a given D depth profile [27, 28]. The program simulates the D profile by dividing the target into thin slabs with uniform D concentration. An example of the resultant D concentration profile is shown in fig. 2.6 (a). While the initial energy of the ^3He beam is nearly mono-energetic in vacuo, the material interaction invariably convolves the ion energy as a function of material path length. Shown in eq. 2.5, Mayer [27] outlines the convolution of the ideal yield (i.e. eq. 2.4) with a source of statistical uncertainty (i.e. a Gaussian approximating energy loss straggle).

$$S(E) \propto \int_0^\infty P_i(E - E') f(E', \sigma^2(E')) dE' \quad (2.5)$$

$$Y_{i,sim}(E_0) \propto \int_{E_i}^{E_{i+1}} S(E') dE' \quad (2.6)$$

For each probing ^3He energy and associated proton energy spectra, the SimNRA software requires the user to manually adjust both the D concentration and the width of each slab in order to fit each observed energy spectrum. Prior to the development of NRADC [42], there was no well defined method to fit multiple spectra, one for each probing energy, with the same target parameters. The problem was ill-posed since different parameters could result in a plausible fit to the product ion energy spectra. NRADC calls upon multiple instances of SimNRA, one for each probing energy, and utilizes a Markov Chain Monte Carlo (MCMC) scheme to optimize fits for concentration and slab width, producing the most probable D depth profile.

2.3.3 Thermal Desorption Spectroscopy

The flux of D by thermal desorption from the sample surface and total D retention throughout the bulk were measured with TDS. W samples were mounted with a thermocouple pressed against the rear surface, pumped down to a vacuum below 10^{-6} Pa, and heated by infrared lamps at a constant rate of 0.5 K/s before plateauing near 1300 K. While at low temperature, atoms trapped in a defect lack the energy needed to escape the potential well. With increasing sample temperature, some of these atoms can acquire enough kinetic energy via collisions within the trap to then escape the trap and enter into solution (i.e. between lattice sites). Once liberated from the defect, solute atoms can diffuse, trap, release, and repeat this process many times before reaching the surface. In order to leave the surface, atoms must overcome a surface barrier and recombination must occur in the case of molecular gaseous species (e.g. HD or D₂). Within the vacuum vessel and outside the sample, the released gas will either reach a turbo pump or the Residual Gas Analyzer (RGA). Inside the RGA, the gaseous particles are ionized and accelerated into a Quadrupole Mass Spectrometer (QMS). The QMS rods are biased to allow only ions with a particular charge:mass ratio to pass through and reach a detector. The partial pressures of H₂, HD, and D₂ were measured and analyzed to determine a D flux as described in the following subsection.

Experimental notes to consider while performing TDS include attention to high vacuum practices. A clean vacuum chamber is critical to obtain usable TDS data. Vacuum contaminants are unavoidable since simply changing samples requires a vacuum break. Exposing the TDS chamber to atmosphere introduces multiple mono-layers of water to both the sample surface and chamber walls, which can lead to a significant background signal. Though this can be managed as described in the next subsection, chemical contamination to the vacuum system may lead to tainted data. Chemical contamination of the walls (e.g. oils high in carbon) can act as a getter for hydrogenic isotopes. A portion of gas released from the sample will collide with the vacuum wall

and reach contaminants that then chemically bind. Further heating of the sample also indirectly heats the walls. When the chemical bonds break, the gas releases at a significantly different temperature than needed to initially escape the sample. This process ultimately alters the signal in a way that cannot be removed during analysis.

2.3.4 TDS Analysis Program

In order to further isolate the release of D measured through TDS, a new custom-developed analysis technique was developed for use with the QMS data generated during TDS. Several problems in previous attempts to analyze the raw partial pressures measured with the QMS were identified and rectified. First, the software package used when operating the Stanford Research Systems QMS led to spurious partial pressures. A plot of pressure versus the mass to charge ratio (m/q) is shown in fig.2.7 and displays various peaks corresponding to H_2 , HD, and D_2 for m/q near 2, 3, and 4 respectively. The shape of these peaks is simply due to how the quadrupole acts as a bandpass filter for mass. The existing QMS software simply took the pressure at a preselected and stationary m/q . The new algorithm developed as part of this research fits a quadratic over several points around this peak m/q value and removes outliers above 2 standard deviations. The result was found to provide much more reliable and repeatable partial pressure measurements with quantified total error estimates.

An additional source of error is the apparent jitter in m/q value recorded by the QMS for each time step. As the QMS performs a m/q sweep, the partial pressures measured may shift with respect to the previous sweep. The new analysis software developed here uses the largest signal, in this case the H_2 partial pressure, to stabilize and isolate all of the m/q values. After these two new analysis schemes were applied to the data, the partial pressures still display a characteristic noise. For both an empty chamber or a constant D_2 source the pressures were seen to fluctuate with time, with a typical $\Delta P/P$ of ~ 0.01 . In order to reduce this noise further, we developed a Gaussian filter implemented over five time steps and applied it to the partial pressures to reduce

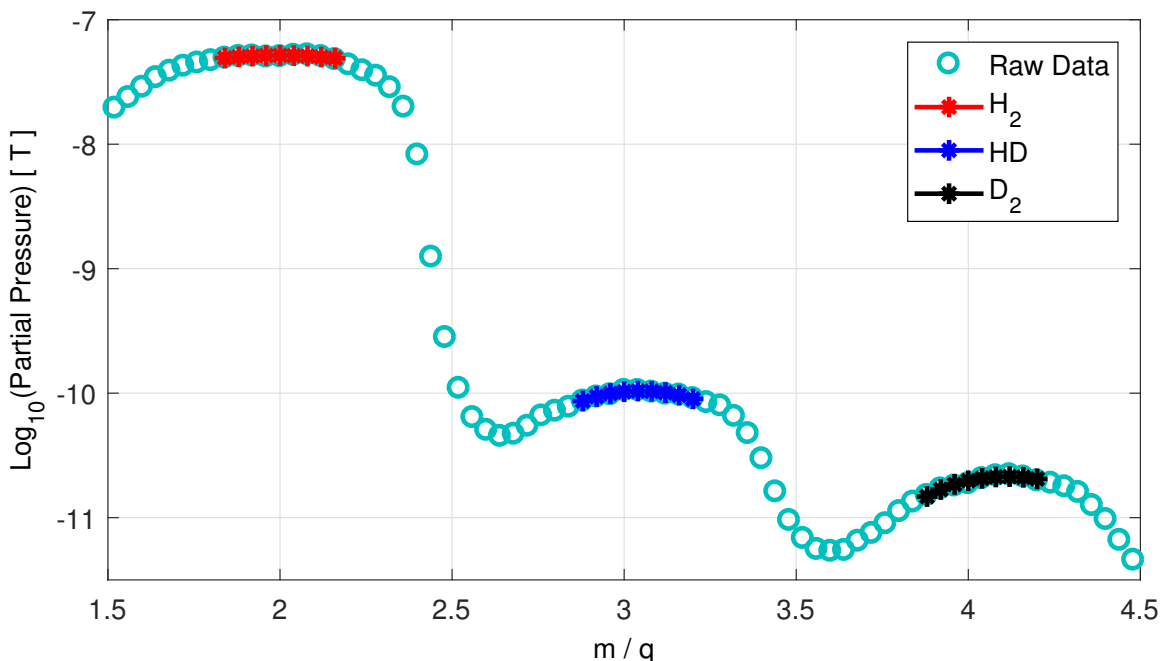


Figure 2.7: QMS partial pressures plotted against mass to charge ratio (m/q) for one time step (i.e. one sweep). Each peak is fit with a quadratic to find the peak value and remove outliers.

the noise inherent to the measurement as shown in fig.2.8.

The next source of error is the presence of a background signal due to residual water vapor in the TDS oven vacuum system. Depending on ambient laboratory humidity, temperature, and the length of vacuum break, the installation of a sample allows water to be adsorbed on the vacuum chamber walls when exposed to atmosphere. These walls were indirectly heated while performing TDS on a sample, creating H_2 , HD, and D_2 signals due to degassing water from the walls of the oven. The isotopic partial pressure is typically small for HD and D_2 relative to H_2 , with a natural abundance below 10^{-3} and 10^{-4} respectively. With increasing temperature this water vapor contribution to the HD and D_2 signals become large enough that it must be corrected. In order to remove this background signal, the dominant H_2 is scaled separately to the HD and D_2 signals, as two functions $f(P_{H_2})$ and $g(P_{H_2})$. The functional form used for f and g was typically a linear dependence on P_{H_2} . After the initial 0.5 K/s temperature ramp, fig. 2.9 demonstrates the use of several additional temperature ramps to aid in the linear scaling and offset of H_2 to HD and D_2 .

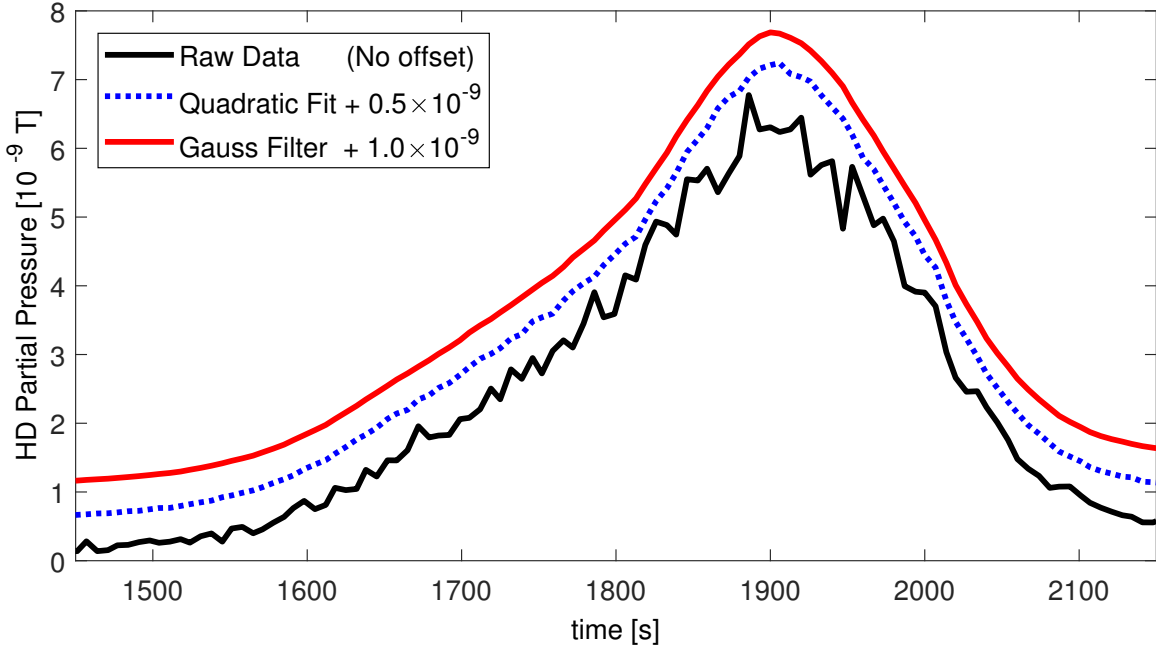


Figure 2.8: The raw HD partial pressure is plotted in black for the m/q value of 3. Performing a stabilization and quadratic fit to the HD peak results in the blue dotted line. A Gaussian filter over 5 time steps produces the smoothed red line. Note that the post-analysis lines are offset for clarity.

Finally, the total D flux (Γ) was calculated as defined in eq. 2.7. A calibrated D_2 leak was used to convert the partial pressure from the QMS to a thermally desorbed particle flux from the sample. Without any further correction for ionization efficiency, the calibration conversion for D_2 and HD are approximated to be the same ($c_{D_2} \approx c_{HD}$) [56]. The number of D atoms in each molecule is accounted for when determining the total D atom flux leaving the surface. The resulting TDS profile consists of a D flux versus either time or temperature. Integrated over time, the D flux results in the total D retention. Displayed with respect to temperature, the D flux can be used to infer the thermal energy needed to overcome and escape a defect's potential well.

$$\Gamma_D = 2c_{D_2}(P_{D_2} - f(P_{H_2})) + c_{HD}(P_{HD} - g(P_{H_2})) \quad (2.7)$$

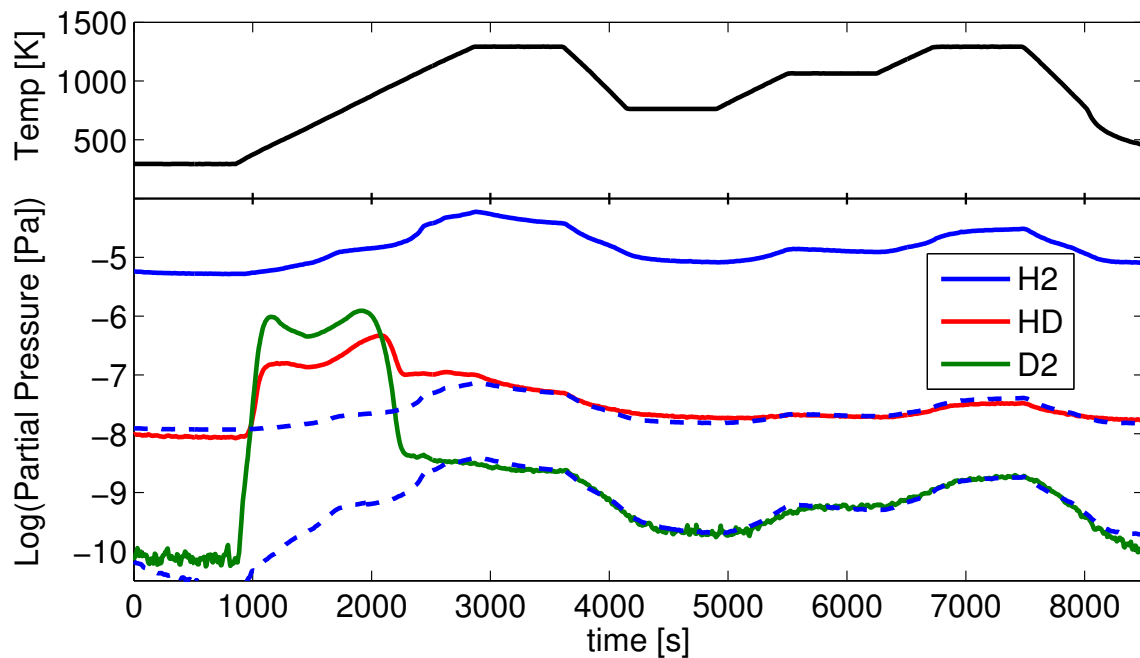


Figure 2.9: TDS data is shown for a sample with a linear heating ramp of 0.5 K/s held fixed at 1300 K and followed by additional cooling and heating ramps. Beyond the initial temperature ramp, the HD and D₂ has effectively degassed from the sample and what remains is primarily due to water on the chamber walls. Shown as blue dashed lines, the H₂ signal is linearly scaled to this background for HD and D₂.

Chapter 3

Previous Results

Within the PISCES program, properties such as the thermal conductivity and hydrogen isotope retention in displacement-damaged, plasma-exposed W have been studied under relevant fusion conditions. Barton *et al.* [8] laid the foundation for the retention studies presented in this thesis. Specifically, the experimental procedures of sample preparation, heavy ion damage, D₂ plasma exposure, NRA, and TDS were well outlined. Here we summarize some of the essential findings of this earlier work as a motivation for the present dissertation research.

3.1 D Retention Experiments in Heavy Ion Damaged W

As previously described, neutron damaged W samples exposed to a D₂ plasma exhibit a significantly enhanced D retention [44]. In lieu of energetic neutrons, heavy ions are used to produce damage near the surface, within the first few microns. Both neutrons and heavy ions impart enough energy to the W lattice to cause collision cascades. Initially, the collision cascade begins when the primary knock-on atom (PKA) is displaced from a lattice site. Depending on the kinetic energy imparted, the PKA may travel within the material a short distance before colliding with another lattice atom. The ensuing cascade of collisions is localized. Whereas the kinetic energy imparted to the PKA is spread for heavy ions as they lose energy traveling in the lattice,

neutrons produce a nearly mono-energetic PKA. Yet the ensuing collision cascade effectively acts to spread the kinetic energy, increasing the similarity between defects produced by either neutrons or heavy ions.

With respect to heavy ion damage, Barton *et al.* [8] demonstrated that W and Cu ion damaged W produced similar D retention for the same displacement damage. In that work, multiple displacement damage profiles were calculated for both Cu and W ion beam energies. The SRIM simulated damage profiles for a 2 MeV Cu and 6 MeV W beam were shown to produce nearly identical profiles and thus expected to have the same number of defects. Note that it takes 3.5 times the number of Cu ions compared to W ions to produce the same peak dpa level with respect to these ion beam energies. The D retention in W samples damaged with either Cu or W to the same peak dpa level (e.g. 1, 0.1, or 0.01 dpa) had the same total retention as measured by NRA and TDS. In unpublished work by Barton, the resulting D retention was found to deviate as the damage was increased beyond 1 dpa. Near 1 dpa the implanted Cu approaches the intrinsic impurity level of Cu in the 99.95% pure W samples and begins to alloy the material, significantly altering the W lattice. Previous heavy ion damage study [50] have demonstrated that D retention saturates at a peak dpa well below 1 ($\sim 0.2 - 0.4$ dpa). Thus heavy ion damage within the relevant dpa range, prior to induced defect saturation, is indistinguishable for various heavy ion species. It should be noted that for a lower mass ion beam, a higher fluence of ions will be needed to reach an equivalent peak damage and result in adding a significant amount of impurities to the W. Therefore the damaging ion species and fluence must be considered when using heavy ion damage to simulate neutron damage.

3.2 Defect Recovery/Annealing

The production of defects due to either neutron or heavy ion damage will compete with the rate of recovery when the material is held at an elevated temperature. Previous work by

Ogorodnikova *et al.* [33] showed a significant reduction in D retention when heavy ion damaged W was annealed *after* the displacement damage occurred. Whereas interstitial W atoms are mobile at relatively low temperatures, vacancies become increasingly mobile above 623 K [18]. The vacancies may agglomerate into larger complexes or annihilate at free surfaces and interstitials. At temperatures approaching 900 K the dissolution of vacancy complexes leads to further defect recovery. As seen in Fig. 3.1, above 1200 K the dissolution of dislocation structures is visible under Transmission Electron Microscopy (TEM). Finally, above the recrystallization temperature for W (~ 1573 K) the microscopic defect structures are completely eliminated as seen in (f). This earlier work clearly showed that annealing of the displacement damage was indeed possible, it left a crucial question unanswered: would the annealing rate be large enough to overcome the rate of displacement damage, and thus significantly reduce the defect density which then subsequently acts to trap plasma-implanted fuel ions?

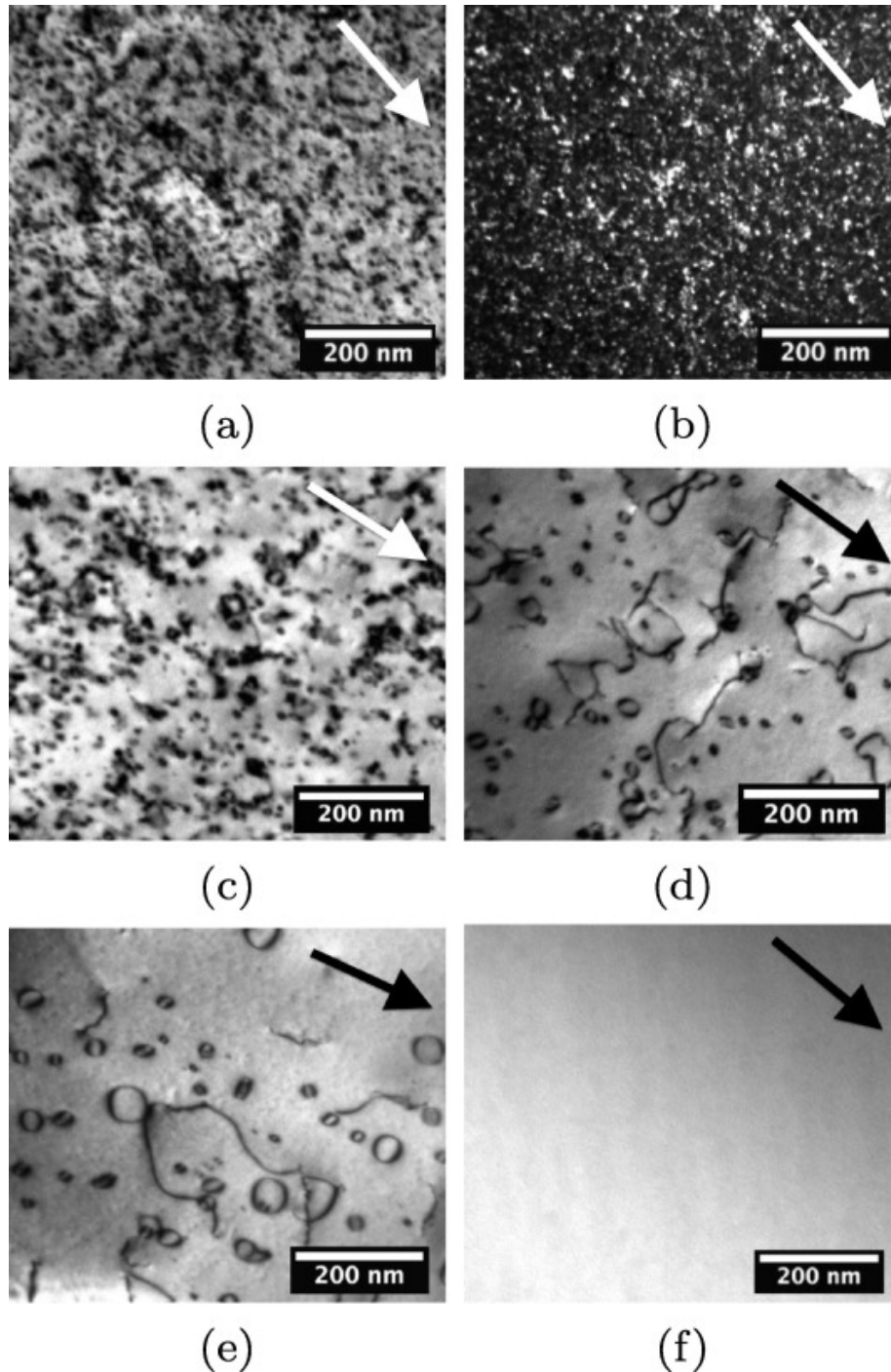


Figure 3.1: Damage microstructure in (a and b) as-irradiated tungsten (1.5 dpa, 2 MeV W^+ , 773 K) and post-irradiation annealed tungsten subject to conditions of (c) 1073 K for 1 h, (d) 1223 K for 1 h, (e) 1373 K for 1 h, (f) 1673 K for 1 h. All micrographs shown were imaged close to $[0\ 0\ 1]$, with $\equiv (2\ 0\ 0)$ excited. The arrow in each micrograph shows the direction of the g -vector. (b) Is weak-beam dark-field ($g, 3 - 4g$), to pick-up the diffraction contrast of very small loops, 1 - 2 nm, (a) and (c - e) are two-beam kinematical bright-field images [18].

3.3 Application of Reaction-Diffusion Codes

Barton's work in developing a simplified diffusion model [9] with decoupled traps led to further inquiry and attempts to model both the uptake and desorption of D in W. This model assumes each trap is filled independently of any other trap. This decoupled model was limited to a constant temperature and could not easily be applied to the controlled thermal desorption of D. Ultimately, experiments would prove to be best modeled using a system of coupled traps in a reaction-diffusion code such as the Tritium Migration Analysis Program (TMAP7) [29].

Though TMAP7 does model a system of coupled traps, it is limited to three concurrent traps. Both experiment and theory show the need for additional traps. In neutron damaged W exposed to a D₂ plasma studied by Shimada *et al.* [44], a minimum of six traps are needed to fit the TDS data well. In that work, three coupled traps were simulated at a time. The three lowest and three highest detrapping energies were modeled separately and simply added together as seen in fig. 3.2. In the overlap region shown in (c), this approximation neglects the coupling that occurs for the 1.3 and 1.5 eV traps. In order to continue to utilize the well validated and verified TMAP7, we developed and applied a new Pseudo Trap and Temperature Partitioning (PTTP) scheme to experimental data in chapter 5. This scheme then allows us to model the trapping and release of D in the displacement damaged W used here, which typically exhibits up to 7 distinct trapping energies.

3.4 Isolating Various Traps

NRA primarily gives depth information on D retention whereas TDS reveals information about the detrapping energy (E_{dt}) as well as the related binding and trapping energy (E_{tr} and E_b), where $E_{dt} = E_{tr} + E_b$. Most experiments on D retention in W demonstrate similar TDS release peaks. As Barton *et al.* [9] point out, Density Functional Theory (DFT) predicts a plethora of

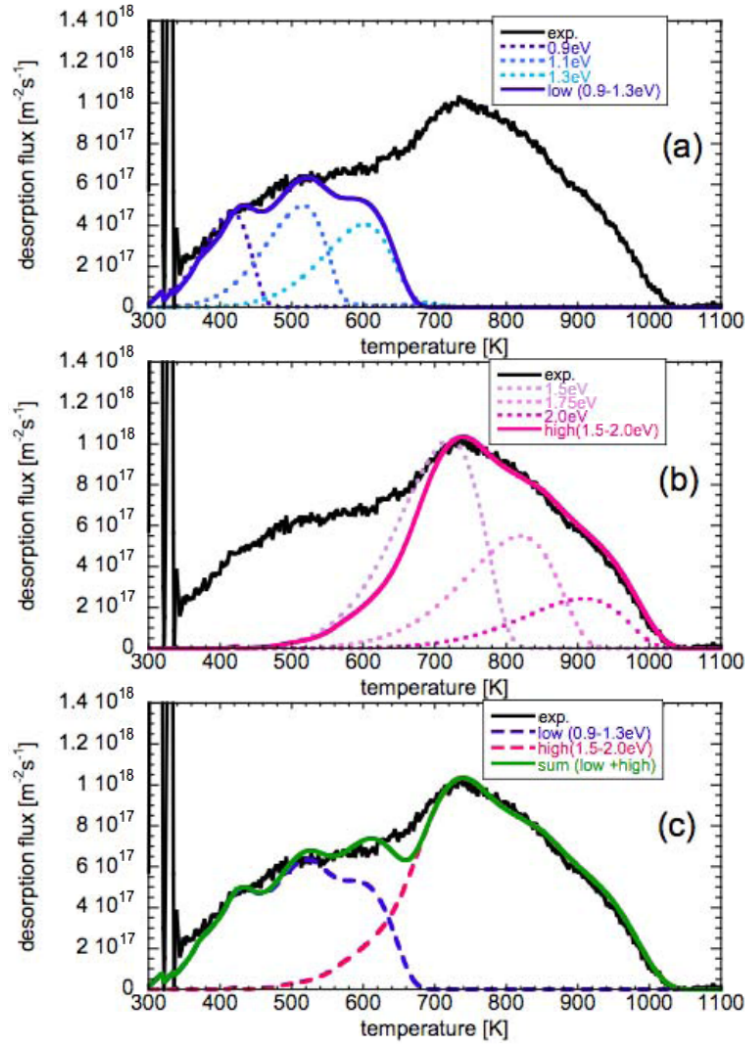


Figure 3.2: In order to simulate six detrapping energies, Shimada *et al.* [44] separately simulated three lower energy traps (a), three higher energy traps (b), and summed the result (c).

trapping energies ranging from 0.2 to 1.8 eV. In contrast, experiment demonstrates only a few discernible distinct release peaks in TDS data. A possible reason for the discrepancy is the small separation of E_{dt} values. DFT calculations by Liu *et al.* [24] predict that a mono-vacancy can trap up to 10 D atoms. As D atoms are added to the vacancy, the trap depth decreases with increasing D occupancy as follows: 1.13, 1.12, 1.09, 1.06, 1.01, 0.94, 0.84, 0.71, 0.52, and 0.26 eV. Similar values from other DFT calculations for the first five binding energies are also shown in fig. 3.3. These results suggest that an increasing occupancy level lowers the detrapping energy until the defect no longer can hold an additional atom. Zibrov *et al.* [61] damaged a W

sample with 10 keV D ions to induce defects that are correlated to a single well resolved peak near ~ 600 K. Heavy ions at large energies can produce cascades of collisions within the material lattice, while the relatively low energy and low mass D ions used by Zibrov likely produced mono-vacancies. The first few nearby binding energies could slightly broaden the release peak and be nearly indistinguishable from a single trap with an effective binding energy. The existence of the additional trap energies predicted by DFT would be expected to significantly broaden the leading edge of the release peak but such broadening does not generally appear in TDS data, raising doubts about the predictions.

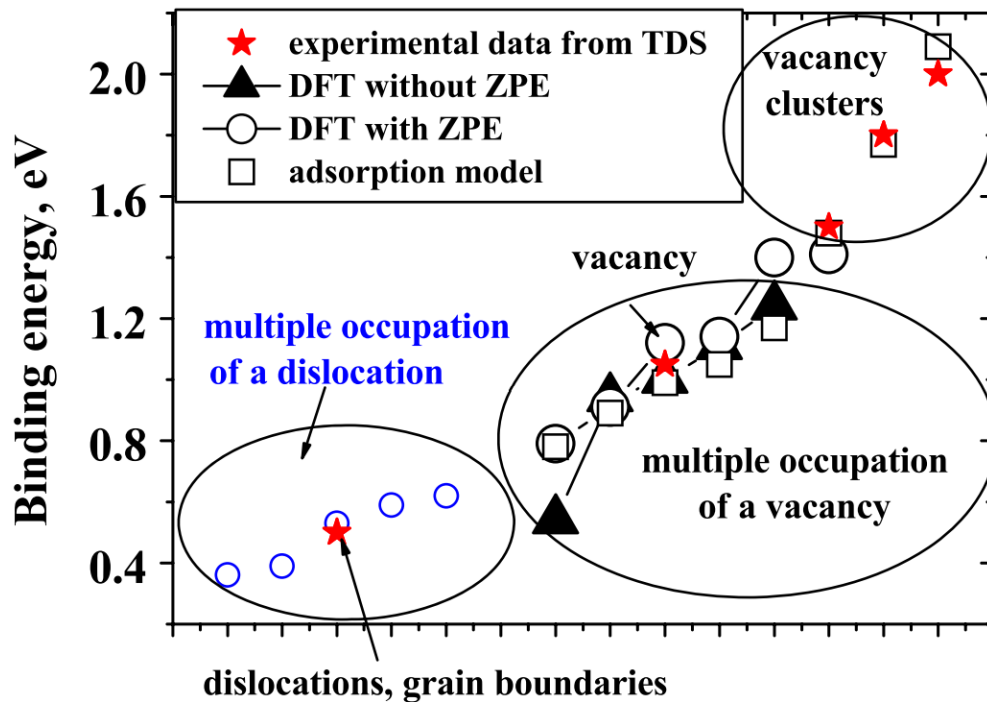


Figure 3.3: Ogorodnikova *et. al.* [30] (adapted) plotted various binding energies (E_b) against associated defects (arbitrary x-axis).

Further TDS and NRA data is needed to isolate the binding energies and spatial profiles for ion and neutron induced traps. As shown in fig. 3.3, Ogorodnikova speculated about the type of defect likely associated with each binding energy [30]. The lowest energies are likely due to grain boundaries. The mid range energies have been shown to correlate with mono-

vacancies. The highest energies are likely related to vacancy complexes, voids, and dislocations. These different types of defects, with their corresponding trapping energies, occur with distinct spatial distributions. In particular, intrinsic defects such as grain boundaries and impurities are distributed throughout the material. In contrast, defects induced by the high flux, low energy plasma bombardment will be concentrated near the surface, while those arising from energetic particle collision cascades are peaked deeper within the material.

This earlier observation suggests that if the spatial resolution of NRA could be combined with the capability of TDS infer trap energies, it might be then possible to more tightly constrain the data and thereby infer the spatial location of traps with differing energies. Motivated by this idea, a new partial thermal desorption scheme, coupled to sequential NRA profiling, was performed in order to better isolate the various traps and was developed and applied in chapter 6. The results indeed suggest that existence of three types of traps within the W samples used in this work. First, a population of uniformly distributed low-energy traps is found. Second, a population of intermediate energy traps in the near-surface region is found, presumably induced by plasma irradiation. Third, a population of deeper traps with a spatial distribution coincident with the heavy ion displacement-damage profile is found.

Chapter 4

Reduced Deuterium Retention in Simultaneously Damaged and Annealed Tungsten

4.1 Introduction

The trapping and retention of tritium fuel within neutron damaged plasma facing components (PFC) is of primary concern for next step fusion devices such as ITER and DEMO [47]. However, the direct study of neutron damaged material is difficult due to the time needed for activated samples to decay back to safe levels and the lack of high flux neutron sources to produce a fusion relevant fluence in a short period of time [44]. As such, the use of heavy ion damage and deuterium as a proxy for neutrons and tritium, respectively, allow for more timely experimental studies of fundamental aspects of this important problem. The reader is referred to ASTM E521 [15] for the key differences between neutron and heavy ion displacement damage.

Currently, W is the primary PFC candidate for first wall and divertor armor due to its high melting point, low H isotope retention, and resistance to sputtering [47]. Relevant PFC

temperatures span 373 to 1273 K for tokamak devices such as ITER and DEMO [11]. Previous studies that induced ion damage near room temperature followed by subsequent annealing steps before or during plasma exposure have shown a reduction in D retention [50, 35]. In order to further isolate and investigate fusion relevant damage production and recovery, heavy ion damage was performed while simultaneously heating/annealing W samples. In accordance with similar experiments [41, 33], the concurrent heavy ion irradiation at elevated temperature will be referred to as dynamic annealing. In this experiment, further recovery of defects during plasma exposure is limited by holding the sample at a low temperature of 383 K. This sample temperature still allows rapid D diffusion in W [19] while limiting the release rate, thus allowing D to occupy near-surface ion induced traps. These considerations allow D to act as an effective marker for trap sites that can be probed by NRA and TDS techniques.

4.2 Experiment

4.2.1 W Sample Preparation

Supplied by Midwest Tungsten, samples were cut from certified 99.95 wt.% powder metallurgy polycrystalline W rod, 6 mm in diameter and 1.5 mm thick. The surfaces to be exposed to plasma were mechanically polished down to 3 μm grit, producing a mirror finish. Afterwards, the samples were cleaned in ultrasonic baths, first in acetone and then ethanol. To further relieve mechanical stress and reduce intrinsic defects, the samples were then annealed *in vacuo* below 10^{-4} Pa at 1173 K for 1 hour. Under a scanning electron microscope, an annealed sample broken in half was observed to display elongated grains perpendicular to the surface with dimension on the order of 10 μm parallel to the surface.

4.2.2 Heavy-ion Displacement Damage in W

In the Ion Beam Materials Laboratory (IBML) at Los Alamos National Laboratory (LANL), a tandem ion accelerator irradiated the polished W samples with 3.4 MeV Cu²⁺ ions. Cu was chosen over W, since the lighter Cu ions penetrate deeper for comparable energies. SRIM-2012 [62] was used to estimate the displacements per atom (dpa) profile as a function of the beam parameters. Per Stoller *et al.* [48], the “Quick” Kinchin-Pease option and a displacement damage threshold of 90 eV for W were used. A peak dpa of 0.2, achieved by a dose of 1.82×10^{18} ions/m² with an average flux of $\sim 10^{15}$ ions/m²/s, ensured the implanted Cu remained below intrinsic Cu impurity levels [8].

In general, the ion beam community follows the practice recommended by ASTM [15] when performing ion irradiations. Specifically, it recommends to use a defocussed ion beam to avoid periodic local flux variations artificially introduced when rastering a beam. However, it is also a common challenge to produce a uniform irradiated sample with the defocussed beam. We chose the rastering beam to produce a relatively large damaged sample size with excellent lateral uniformity.

4.2.3 Concurrent Heating During Damage

A vacuum chamber at IBML with a heated stage was used to hold W samples at 300, 573, 873, 1023, or 1243 K during Cu ion irradiation, inducing dynamic annealing. The samples were affixed to a Ni slab that housed heating elements as well as a thermocouple used to measure the sample temperature. Before Cu ion implantation, the sample holder was heated to the desired plateau temperature. To ensure damage uniformity, the ion implantation was then performed by raster scanning across an area larger than the sample. Prior to reaching the sample, the ion beam was masked to allow the center of the scan to reach the sample while indirectly measuring the current by four corner positioned Faraday cups. Once the desired Cu ion dose was reached,

the beam and heating elements were shut off. The sample holder was then actively cooled with pressurized air to decrease the temperature by half the plateau/room temperature difference within a minute, limiting additional post irradiation annealing of defects.

4.2.4 D₂ Plasma Exposure

One undamaged sample, as well as the Cu ion irradiated samples, were exposed to D₂ plasma with a neutral pressure of ~ 0.7 Pa at UCSD in the PISCES-E device, a plasma etcher with a 13.56 MHz RF source [53]. An RF compensated Langmuir probe measured a flux of $\sim 10^{20}$ ions/m²/s uniformly across the surface of the sample holder. The probe was positioned near the sample holder and the voltage was swept as described in Ref. [51]. A total fluence of 10^{24} D/m² was chosen to decorate the defects throughout the damage region. During plasma exposure the sample holder was negatively biased to achieve an ion energy of 110 eV and air cooled to 383 K as measured by a thermocouple in contact with the rear of the sample. As noted by Yu [58], the molecular ion concentrations were calculated to be 0.72, 0.06, and 0.22 for D⁺, D₂⁺, and D₃⁺ respectively.

4.2.5 Nuclear Reaction Analysis (NRA)

After the plasma exposure, the D(³He,p)⁴He nuclear reaction was used to measure depth profiles of D concentration through NRA as prescribed by Mayer [28]. At IBML, a ³He ion beam was used to probe the D implanted W samples. Increasing ³He energies of 0.6, 0.8, 1.1, 1.5, 2.0, 2.5 and 3.5 MeV probed the first 6 μ m. The energy spectrum of protons captured in a solid state detector was used to determine the depth distribution of the nuclear reactions. The 2 mm thick Si detector was protected from elastically scattered ³He and reactant ⁴He by a 24 μ m thick Al foil. Proton counts were binned according to the detector energy resolution of 22 keV. Two software programs were employed to extract D depth profiles. SIMNRA was used to calibrate and simulate

the proton energy spectrum produced from a given D depth profile [28, 27]. To fit the proton energy spectra associated with each ^3He energy, the software requires the user to input and adjust both a D concentration and associated W layer thickness. NRADC calls upon multiple instances of SIMNRA and utilizes a Markov Chain Monte Carlo scheme to optimize fits for concentration and thickness, producing the most probable D depth profile [42].

4.2.6 Thermal Desorption Spectroscopy (TDS)

The thermal desorption of D from the samples' surface and total D retention throughout the bulk were measured with TDS. Samples were mounted with a thermocouple pressed against the rear surface, pumped down to a vacuum below 10^{-6} Pa, and heated by infrared lamps at a constant rate of 0.5 K/s before plateauing near 1300 K. D trapped in lattice defects acquires thermal energy to escape, diffuse, trap, and repeat many times before reaching the surface. In order to leave the surface, recombination to form a free molecule must occur. The partial pressures of H_2 , HD, and D_2 were measured with a quadrupole mass spectrometer (QMS). A calibrated D_2 leak was used to convert the partial pressure from the QMS to a thermally desorbed particle flux from the sample. The total D flux was calculated as described by Yu [58], as the sum of the HD and twice the D_2 flux. Note that the HD flux was calibrated to the D_2 leak, without any further correction for ionization efficiency, and contributed an average of 25% of the total D flux.

Depending on ambient laboratory humidity, temperature, and the length of vacuum break, the installation of a sample allows water to be adsorbed on the vacuum chamber walls when exposed to atmosphere. These walls were indirectly heated while performing TDS on a sample, creating H_2 , HD, and D_2 signals due to degassing water. The isotopic partial pressure is typically small for HD and D_2 relative to H_2 , with a natural abundance below 10^{-3} and 10^{-4} respectively. With increasing temperature this water vapor contribution becomes large enough that it must be corrected. In order to remove this background signal, the dominant H_2 is scaled separately to the HD and D_2 signals. After the initial 0.5 K/s temperature ramp, Figure 4.1 demonstrates the use of

several additional temperature ramps to aid in the linear scaling and offset of H₂ to HD and D₂.

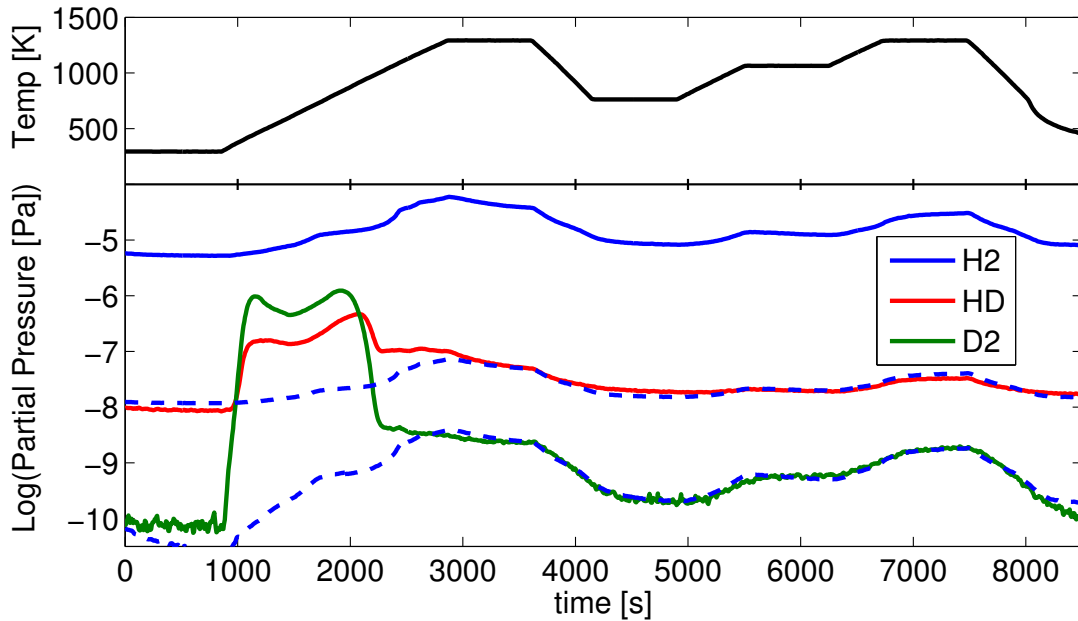


Figure 4.1: TDS data is shown for a sample with a linear heating ramp of 0.5 K/s held fixed at 1300 K and followed by additional cooling and heating ramps. Beyond the initial temperature ramp, the HD and D₂ has effectively degassed from the sample and what remains is primarily due to water on the chamber walls. Shown as blue dashed lines, the H₂ signal is linearly scaled to this background for HD and D₂.

4.3 Results

NRA depth profiles shown in Figure 4.2 demonstrate the reduction of D inventory as the dynamic annealing temperature increases. The control sample was not subject to heavy ion damage but displays D agglomeration in the very near surface, below 0.1 μm , due to stress from plasma implantation [34]. The damaged samples trapped a significant inventory of D within the SRIM predicted displacement damage profile. Since all samples were annealed well below the re-crystallization temperature of 1573 K during preparation, intrinsic defects survive and provide trap sites throughout the samples beyond the ion damage zone.

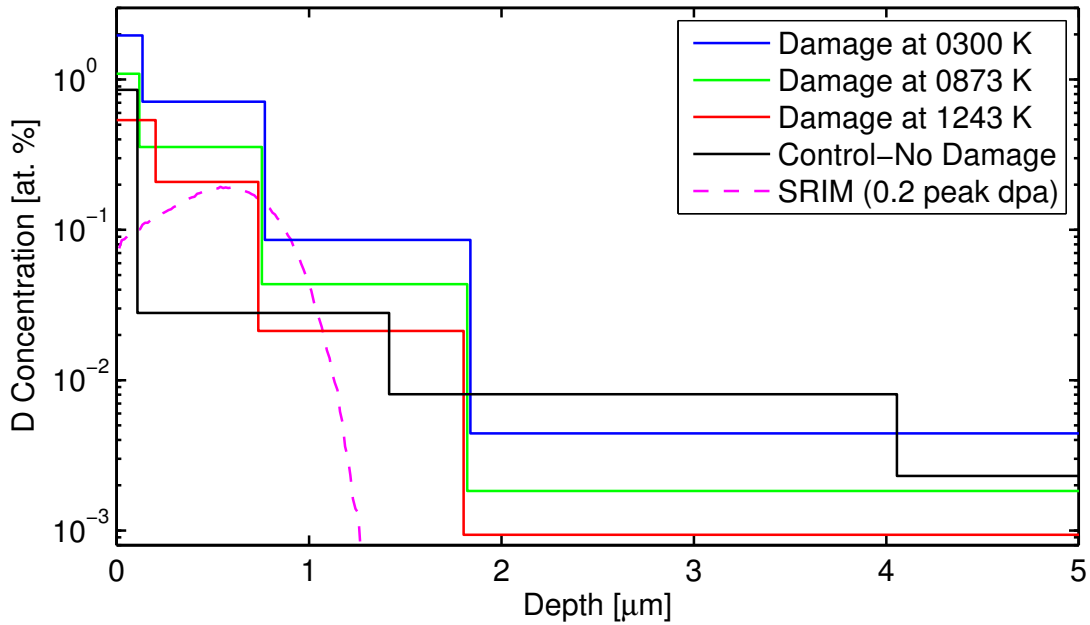


Figure 4.2: NRA measured D depth profiles for 3 samples of increasing temperature during displacement damage by 3.4 MeV Cu ions. The SRIM calculated dpa profile is also shown with a peak dpa of 0.2 near 0.6 μm .

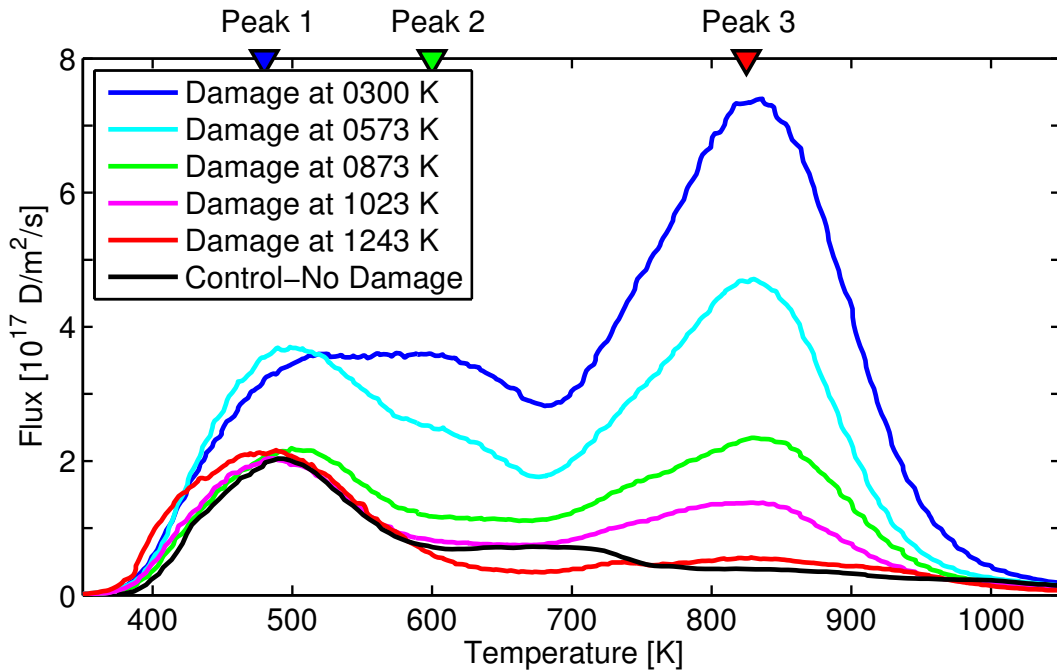


Figure 4.3: D release measured by TDS on samples simultaneously damaged with 3.4 MeV Cu ions while being heated. Decreasing retention trending toward the undamaged/control sample is found. Peaks 1-3 with release temperatures at 480, 600, and 825 K are indicated.

The TDS data in Figure 4.3 displays multiple D release peaks near 480, 600, and 825 K assigned as peaks 1, 2, and 3 respectively. Peak 1 is present in all samples and is associated with intrinsic defects that survived the annealing during preparation. Peaks 2 and 3 are largest for the sample damaged at 300 K and are significantly lower for the undamaged sample, demonstrating that these peaks are primarily due to ion induced damage. Previously, each peak has been associated with a de-trapping energy modeled as 0.85, 1.45, and 1.85 eV in Ref. [35]. According to that work, peak 1 corresponds to dislocations and grain boundaries, peak 2 to vacancies, and peak 3 to vacancy clusters. Also of note, the initial release of D occurs near 383 K, the sample temperature during D₂ plasma exposure. The total D retention from NRA and TDS measurements are compared in Figure 4.4. The spatially integrated D profile from NRA accounts for the first 6 μm, while TDS probes the entire sample. Both NRA and TDS monotonically decrease towards the D retained within the control sample.

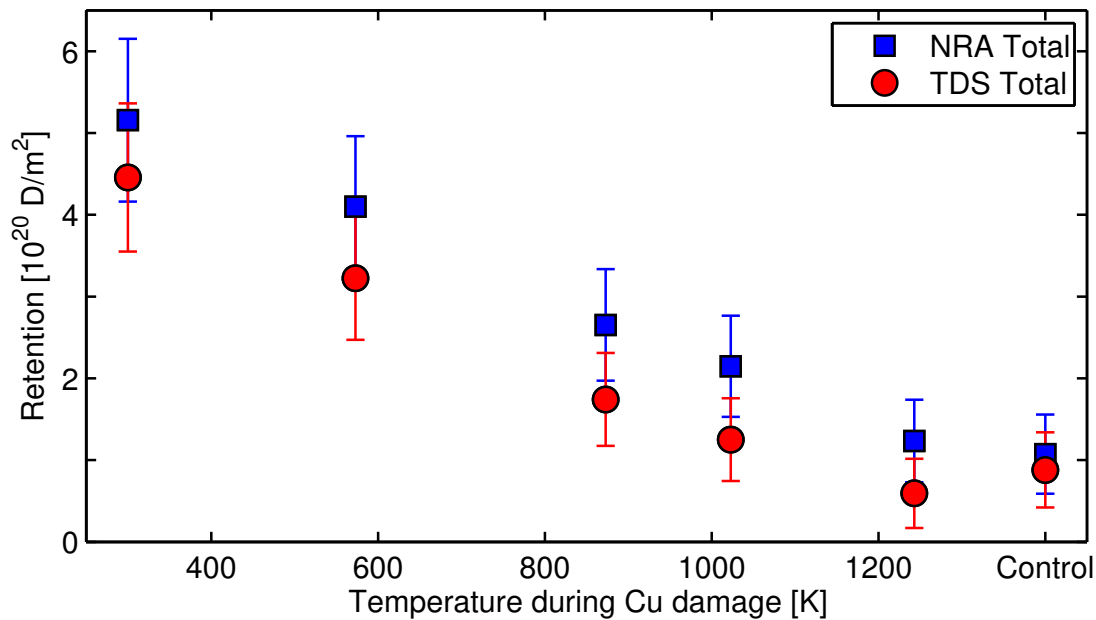


Figure 4.4: The total D retention measured via NRA up to 6 μm and TDS throughout the bulk of the samples.

In order to isolate the recovery of each type of defect, a Gaussian was fit to each release peak. For the case in which desorption peaks overlap, traps become coupled as D atoms escape/-

trap/migrate through the W lattice. To first order, the sum of Gaussians can reasonably represent thermal desorption as a function of temperature in the case of clearly separated release peaks [37, 26]. Holding the width and position fixed for each individual peak, only the amplitude was varied in the fitting for all samples. The sum of the 3 Gaussians fit to the room temperature damaged sample as well as each individual Gaussian are plotted in Figure 4.5, demonstrating the well resolved release peaks.

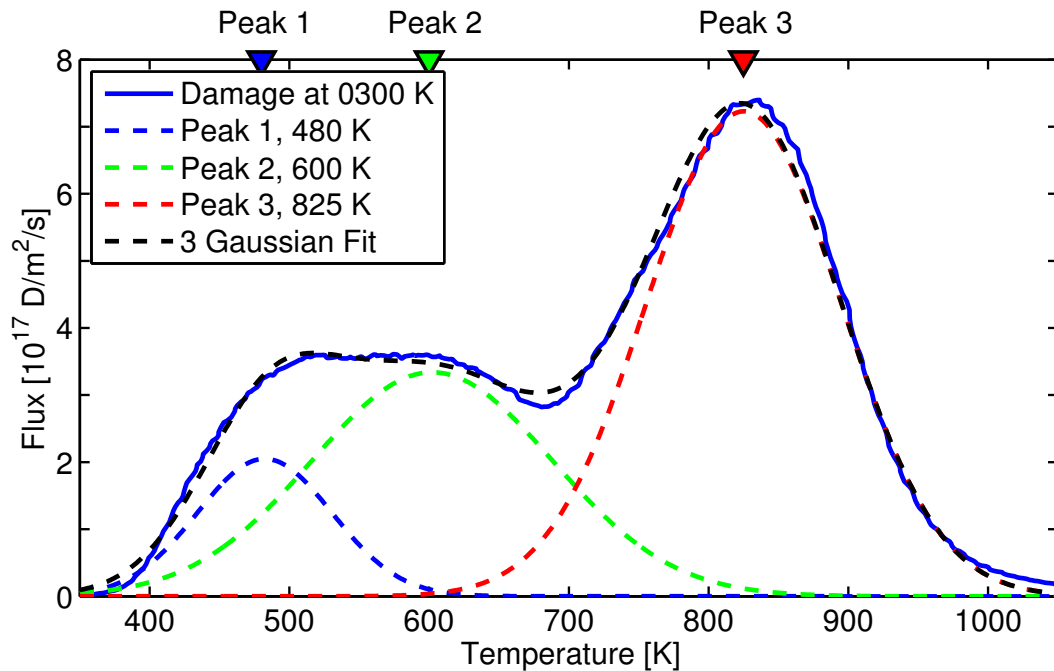


Figure 4.5: The thermal desorption flux (solid line) of D is fit with the sum of 3 Gaussians peaked at 480, 600, and 825 K (dashed lines).

The total D retention for each release peak is plotted in Figure 4.6 as the integrated area under each Gaussian. The D retention for release peak 1 is relatively constant for all damaged samples as well as the control/undamaged sample. D retention for release peaks 2 and 3 is highest for the room temperature damaged sample. For peaks 2 and 3, increasing the dynamic annealing temperature leads to decreased retention. The sample dynamically annealed at 1243 K approached the level of retention found in the control sample. While NRA displays there is D retained within the displacement zone, the TDS data shows that it is primarily stored in peak 1.

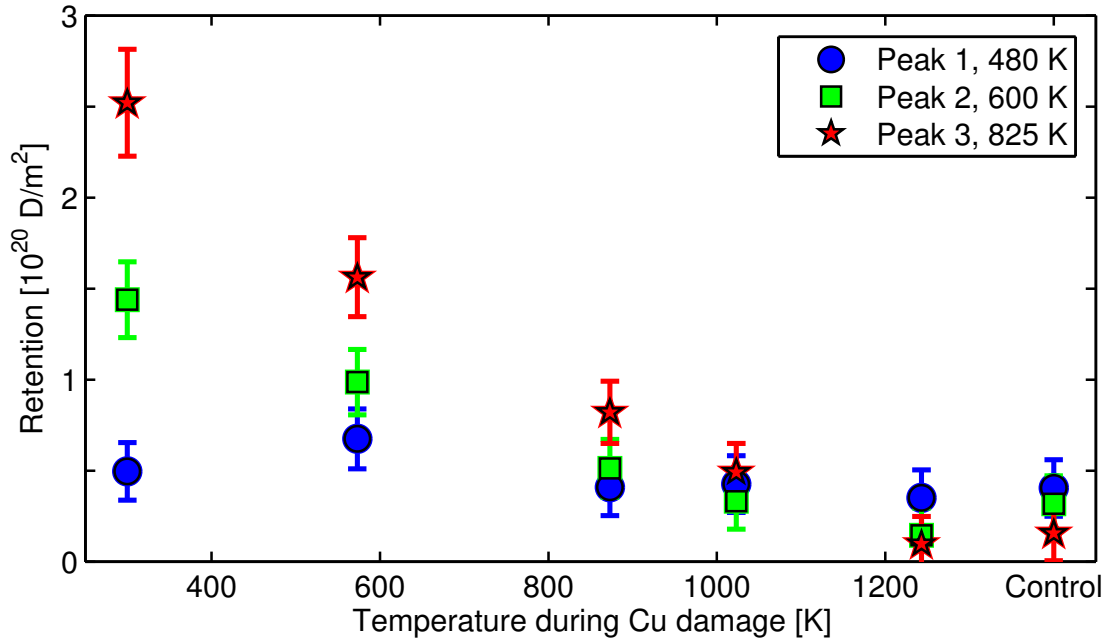


Figure 4.6: Three Gaussians peaked near ~ 480 , 600 , and 825 K were fit to TDS profiles of D release. The total D retention associated with each Gaussian is plotted here, demonstrating the recovery from damage with concurrent elevated sample temperatures.

4.4 Discussion

In experiments similar to this work, Sakurada [41], Ogorodnikova [33], and Markina [26] utilized D retention to study the annealing of heavy ion damaged W samples. Each experiment's specific heavy ion species and energy resulted in a unique dpa profile. By normalizing the total D retention to each respective dpa profile as shown in Figure 4.7, all five experimental conditions can be directly compared. In order to account for the previously reported saturation of D retention [50], the data from Markina was scaled down to 0.45. A general trend of decreased D retention with increased annealing temperature occurs for both dynamic and post irradiation annealing. In contrast to the other experiments, Ogorodnikova's NRA demonstrated a local increase in total D retention near an annealing temperature of 1000 K for both the dynamic and post annealed samples. By 1300 K, Ogorodnikova observed nearly complete recovery from post irradiation annealing.

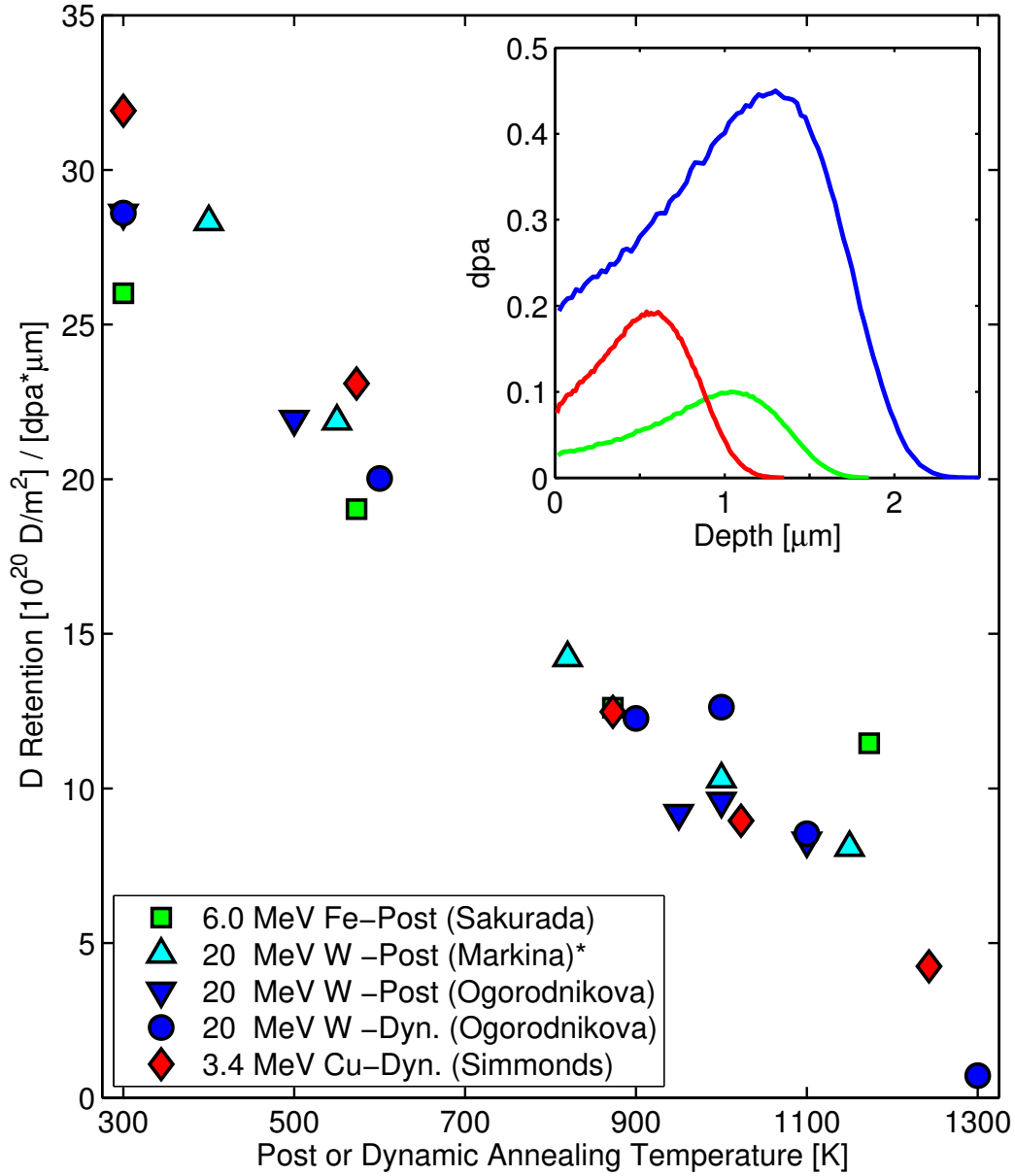


Figure 4.7: Total D retention normalized to the displacement damage profile (i.e. dpa* μ m) shows agreement between Sakurada [41], Markina [26], Ogorodnikova [33], and this work. The inset plot shows the profiles for Fe (green), W (blue), and Cu (red) with peak dpa of 0.1, 0.2, and 0.45 respectively. *Note that Markina’s peak dpa is scaled to 0.45.

Similar to Sakurada, this work prepared samples well below the recrystallization temperature and exposed to a D₂ plasma at a low enough temperature to populate peak 1. TDS for both experiments demonstrated a nearly constant contribution to the total D inventory in peak 1, regardless of annealing temperature.

The TDS profiles for Markina and this work display a monotonic D reduction in peaks 2 and 3. Sakurada observed the same trend for 0.3 and 1.0 dpa damaged samples. However for 0.1 dpa, while peak 3 significantly decreases, peak 2 grows for samples both dynamic and post annealed at 1173 K. Eleveld [17] had previously observed a shift reducing peak 3 and increasing peak 2 occurring above 1040 K. As remarked in Sakurada's paper, the various discrepancies among each work may show the sensitivity of defect recovery to dpa level. That is, the rates of vacancy-cluster and cluster-cluster formation competing with interstitial and free surface annihilation depend on the available concentration of these defects. For instance, the saturation of heavy ion induced defects as dpa approaches 0.3 that has not been observed for neutron damaged W.

To quantify the recovery of heavy ion induced defects at elevated temperatures, we define the fractional recovery of each trap at each dynamic annealing temperature, $F_t(T)$, by subtracting and normalizing the D retention, $R_t(T)$, with respect to the sample damaged at 300 K (i.e. room temperature): $F_t(T) = (R_t(300K) - R_t(T))/R_t(300K)$. The Arrhenius plot, $F_t(T)$ vs. T^{-1} , in Figure 4.8 demonstrates that heavy ion induced defects associated with peaks 2 and 3 are thermally activated and recover with an activation energy near 0.1 eV.

The relatively low activation energy for this recovery is similar to that reported for self interstitial atom (SIA) mobility [5]. While the recovery of W has been shown to have temperature stages in which various defects become mobile [22], recovery is the sum of these processes. With elevated sample temperature, the probability of the vacancy/SIA pair recombining increases due to the increased mobility of each. Though vacancy mobility has been shown to start near 523 K [14], at 1.7 eV the activation energy is an order of magnitude too large to be the primary source of recovery [18]. Thus the current work is more consistent with SIA mobility as the dominant recovery mechanism since they are simply the most mobile defect.

Lastly we remark on the recovery of neutron damage at elevated temperatures. One major difference between ion and neutron induced damage is the displacement rate. Typical experiments

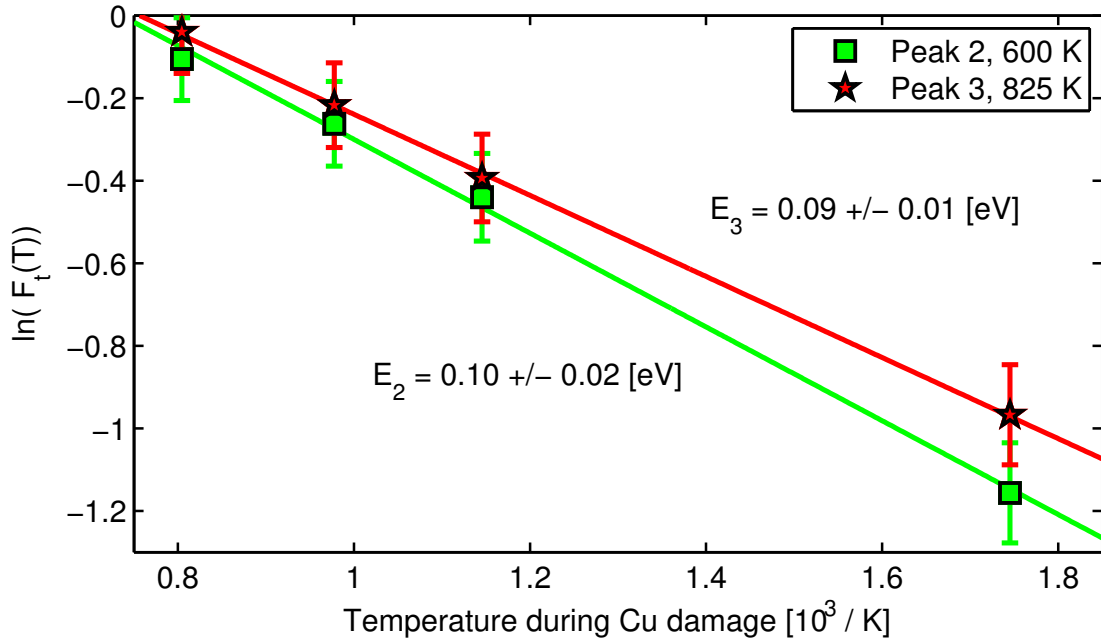


Figure 4.8: The fractional recovery, $F_t(T) = (R_t(300K) - R_t(T))/R_t(300K)$, for both high energy traps correlates with an activation energy of 0.1 eV.

utilize ion dpa rates that are 10^3 to 10^4 times faster than fusion neutrons are predicted to produce [44]. A slower dpa rate will allow for further recovery of damage as mobile SIA will have more time to perform a random walk and possibly recombine with a vacancy or free surface. Neglecting transmutation, these results show that a significant amount of displacement damage from neutrons may be annealed away provided the wall/divertor armor is held at high enough temperature. That is, an optimal temperature window may be possible that limits the net damage induced defect concentration while preventing the loss of favorable elastic and tensile properties.

4.5 Summary

Utilizing plasma implanted and diffused D in heavy ion damaged W, we have isolated and examined the effect of dynamic annealing due to elevated temperature concurrent with displacement damage. NRA and TDS measure a significant reduction in D retention for samples damaged at elevated temperature, approaching the retention found in a control sample that is

undamaged. TDS demonstrates that higher energy, heavy ion induced traps recover with dynamic annealing while the lowest energy, intrinsic trap remains unaffected. The recovery is found to be thermally activated with an activation energy of 0.1 eV and most likely corresponds to the action of SIA mobility.

4.6 Acknowledgments

This work was supported by U.S. Department of Energy under DE-FG02-07ER54912 and DE-SC0001999 as well as the University of California Office of Presidential Research Fund under 12-LR-237801. Chapter 4, including text and data, is in part a reprint of the material as it appears in M.J. Simmonds, Y.Q. Wang, J.L. Barton, M.J. Baldwin, J.H. Yu, R.P. Doerner, G.R. Tynan, Reduced Deuterium Retention in Simultaneously Damaged and Annealed Tungsten, *J. Nucl. Mater.* 494 (2017) 0022-3115. The dissertation author was the primary investigator and author of this paper.

Chapter 5

Expanding the Capability of Reaction-diffusion Codes using Pseudo Traps and Temperature Partitioning: Applied to Hydrogen Uptake and Release from Tungsten

5.1 Introduction

The modeling of tritium fuel trapping and retention within neutron damaged W is of primary concern to next step fusion devices. In addition to the degradation of material properties, the accumulation of tritium has safety requirements regulated by the Nuclear Regulatory Commission [36]. Aside from transmutation and radioactivity, many of the fundamental aspects of neutron damage and tritium retention can safely be studied with the use of heavy ions and deuterium (D), respectively.

The primary experimental techniques for studying hydrogenic retention in W are Nuclear Reaction Analysis (NRA) and Thermal Desorption Spectroscopy (TDS). NRA utilizes a ^3He ion beam to probe the D concentration up to several microns in depth. This technique does not differentiate as to which type of trap holds the D, nor if it is in solution between lattice sites, but can infer the spatial distribution of D contained within the damaged materials. With TDS, the sample temperature is linearly increased and the surface flux of desorbed D is measured as a function of temperature. The flux of D from the sample is complicated by the multi-step migration process of diffusion, trapping, release, and eventual surface recombination to escape the sample. By modeling these coupled processes, TDS can reveal the energy required to escape a given trap. The release behaves as an Arrhenius process, in that an atom is trapped within an energy barrier and may escape once the atom acquires enough kinetic energy via random collisions.

Previous experiments studying the release of D from W through TDS have observed a range of release peaks at different temperatures, leading to a variety of inferred detrapping energies ranging from 0.65 to 2.4 eV [12, 59, 38, 34, 32, 37]. Release peaks may shift in temperature due to various experimental effects. In the case of heavy ion damaged samples, the most significant factor that affects the release peaks is the damage depth profile. Samples with D filling traps formed by damage cascades deeper within the material will have further to migrate before reaching the surface, and thus have a higher probability of retrapping prior to reaching the surface, which leads to a broadening of the release peak and a shift towards higher temperature. Analysis of the release peaks is further obfuscated by the overlapping and coupling of traps due to a range of detrapping energies. In addition, traps with low detrapping energies may be missed entirely when sample temperature during the atomic implantation phase approaches or exceeds its low temperature release peak, preventing that trap from being populated and subsequently inferred through NRA or TDS measurements.

We do note that experiments utilizing ion damage may have experimental data that in turn produces more reliable inferred detrapping energies. Samples with uniform trap concentrations,

such as undamaged or neutron damaged samples, may never saturate the filled trap concentration causing atoms escaping low energy traps to diffuse and further populate high energy traps deeper into the material. This can result in the filling of traps that are located beyond 10 μm depth. The subsequent TDS of such traps results in significant broadening of the release peaks, causing adjacent peaks to overlap and further obscuring the inferred detrapping energies. Unlike an undamaged or neutron damaged sample, the damage profile from heavy ions has a distinct depth and shape localized to the near surface region that can be modeled with the Stopping Range of Ions in Material (SRIM) [48]. Using this ion-induced damage spatial profile as a constraint, the resultant release peaks seen in experimental TDS data have a specific origin, increasing the confidence in the inferred detrapping energies.

In order to infer the detrapping energies from TDS release peaks, a reaction-diffusion model must be used to simulate the experimental conditions. The Tritium Migration Analysis Program (TMAP) is a well validated and verified code used extensively within both the fission and fusion communities to simulate hydrogenic retention measurements [29, 25, 4]. The current version of TMAP7 can model up to three coupled traps simultaneously and was used to model the D implantation and thermal desorption phases of a recent experiment [45]. In our present work, we find that three traps cannot reasonably model the experimental data. To model a larger number of traps concurrently within the TMAP7 framework, we introduce a new PTTP scheme and show that it can effectively model the trapping and release of D from damaged W that exhibits trapping and release in six distinct traps.

5.2 TMAP7 Simulation

As described in detail in [45], W samples were simultaneously damaged and annealed prior to D implantation in the PISCES-E RF plasma device. The simulation of D retention in W can be separated into three phases: the sample preparation, D implantation, and thermal

Table 5.1: Summary of detailed experimental conditions used as inputs to the TMAP7 modeling.

Phase 0 (Sample Preparation)
1.5 mm thick polycrystalline W
Annealed at 1173 K
3.4 MeV Cu ion damage
0.2 peak dpa (Kinchin-Pease)
Simultaneous heating during damage
Temperatures spanning 300 to 1243 K
Phase I (D Implantation)
D ₂ plasma exposure for 50 minutes
Flux average of 3.3×10^{20} D/m ²
Fluence of 10^{24} D/m ²
Ion energy 110 eV
Sample temperature 383 K
20 minutes to cool down to RT
NRA - D concentration up to 6 μ m
Phase II (Thermal Desorption)
Linear temperature ramp 0.5 K/s
Peak temperature of 1273 K

desorption of D. Phase 0, sample preparation, produces the initial concentration of various defects that act as traps. Phase I, D implantation, entails the diffusion of D within the W lattice and the gradual filling of traps encountered by the diffusion front. Phase II, thermal desorption, is defined by the release of D from filled traps by controlled heating of the W sample. Table 1 below provides a summary of the relevant experimental parameters utilized in this simulation.

Simulating the implantation phase, values for mean implantation depth (~ 4 nm) and surface ion reflection coefficient (~ 0.65) were taken from Eckstein [16]. To achieve consistency between modeled depth profile, thermal desorption, and experiment, the surface ion reflection coefficient (R) was increased above the quoted value; the incident ion flux ratio, Γ_{in}/Γ_{ion} , that penetrates the surface and is then implanted was taken to be 8×10^{-4} , where $\Gamma_{in}/\Gamma_{ion} = 1 - R$. This degree of reduction is consistent with what was required to match results in other relatively high ion flux experiments [7]. We do note that a similar implantation profile can be achieved with a reflection coefficient closer to 0.85 when recombination is neglected and instantaneous

surface release is modeled. This is currently an unresolved issue that highlights the difficulty in the application of reaction diffusion physics to the uptake of hydrogenic isotopes in tungsten.

The D filled trap sites shown in the NRA experimental data (thick black) in fig. 5.1 occupy three different spatial zones: the near surface implantation zone (~ 70 nm), the heavy ion damage zone ($\sim 1 \mu\text{m}$), and the intrinsic defects throughout the rest of the sample. The W samples were initially annealed below the recrystallization temperature, which leaves behind a presumably uniform distribution of residual intrinsic defects. A uniform concentration of intrinsic traps was therefore assumed throughout the 1.5 mm thick sample. The spatial profile of D detected by NRA largely coincides with the spatial location of heavy ion damage predicted by SRIM [8]. As a result, in this work the concentration of Cu ion induced defects shown in fig. 5.1 is assumed to have the SRIM spatial profile (red). Within 70 nm of the surface region, the NRA measurements of D retention shows defects were created and populated by D implantation, possibly due to lattice stresses induced by the incident plasma ion flux [32, 52]. Shown on the log-log plot, the implantation zone is a small contribution to the total D retention and therefore simply modeled as a step function up to 70 nm. Since NRA measures the sum of all D filled traps, the type of trap cannot be determined without simulating the thermal desorption phase. As such, the concentration of each trap within each of these three zones is a free parameter, constrained by both the sum of filled traps after implantation (i.e. the spatial D profile from NRA) and the surface flux profile from TDS.

In order to illustrate the need for the new approach proposed here, we model the experiment utilizing TMAP7 with three detrapping energies using an input file that was prepared with the parameters outlined above. Relevant constants such as Anderls recombination coefficient and the mass corrected Fraunfelder diffusion constant are well outlined by Poon *et al.* [37]. Phase I and II are simulated in order to establish a self-consistent solution to the NRA and TDS experimental data. The resultant concentrations of traps due to intrinsic defects and heavy ion damage present after Phase 0 are assumed constant. The plasma exposure modeled in Phase I

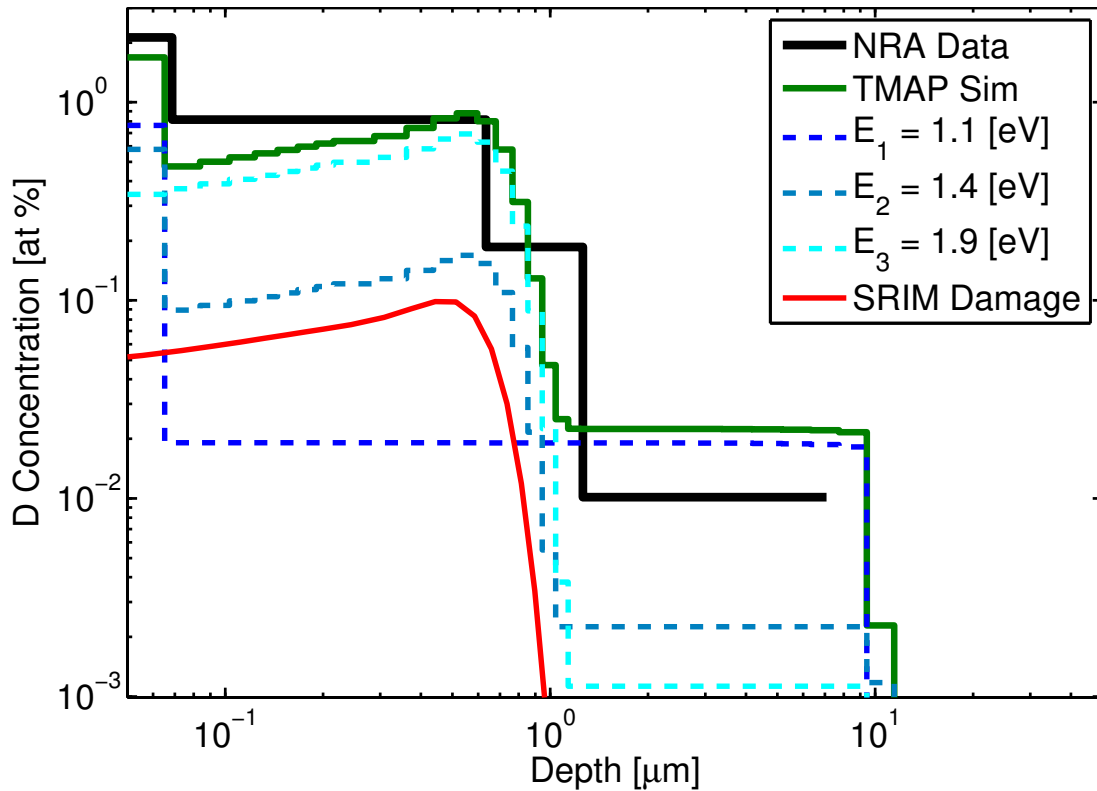


Figure 5.1: Traps 1-3 (dashed lines) are simulated using TMAP and the sum total (green) is compared to experimental NRA data (thick black) with a NRMSE of 0.7. Note that the heavy ion damage profile simulated in SRIM (red) defines the spatial profile of induced traps used in TMAP shown with arbitrary units on the y-axis.

produces further defects in the implantation zone. Due to the high ion flux and rapid surface saturation, the defects induced during Phase I likely formed in less than a second, relatively short compared to the total exposure of nearly an hour. Therefore the near surface implantation induced trap concentration is also assumed to be constant and an initial condition prior to the start of Phase I.

In fig. 5.1 and 5.2, the best-fit NRA profiles and TDS release history from the TMAP7 simulation are shown for a W sample damaged at RT. Here the best-fit is determined by an iterative process of adjusting the various free parameters (e.g. trap concentrations) and comparing the resultant simulation against the experimental NRA and TDS measurements. The experimental and simulation data were interpolated on a finely spaced linear grid in order to determine the "Goodness of Fit." The Normalized Root Mean Square Error (NRMSE) was chosen as the figure

of merit, where 1 would be a perfect fit of simulation to experimental data. Relative to the uncertainty in experimental NRA data, the three-trap TMAP fit to the NRA trapped D profile is acceptable. However, the thermal desorption profile obtained from the same sample, seen in fig. 5.2, has a significant residual error that measures the unaccounted trapping and suggests the presence of more than three detrapping energies.

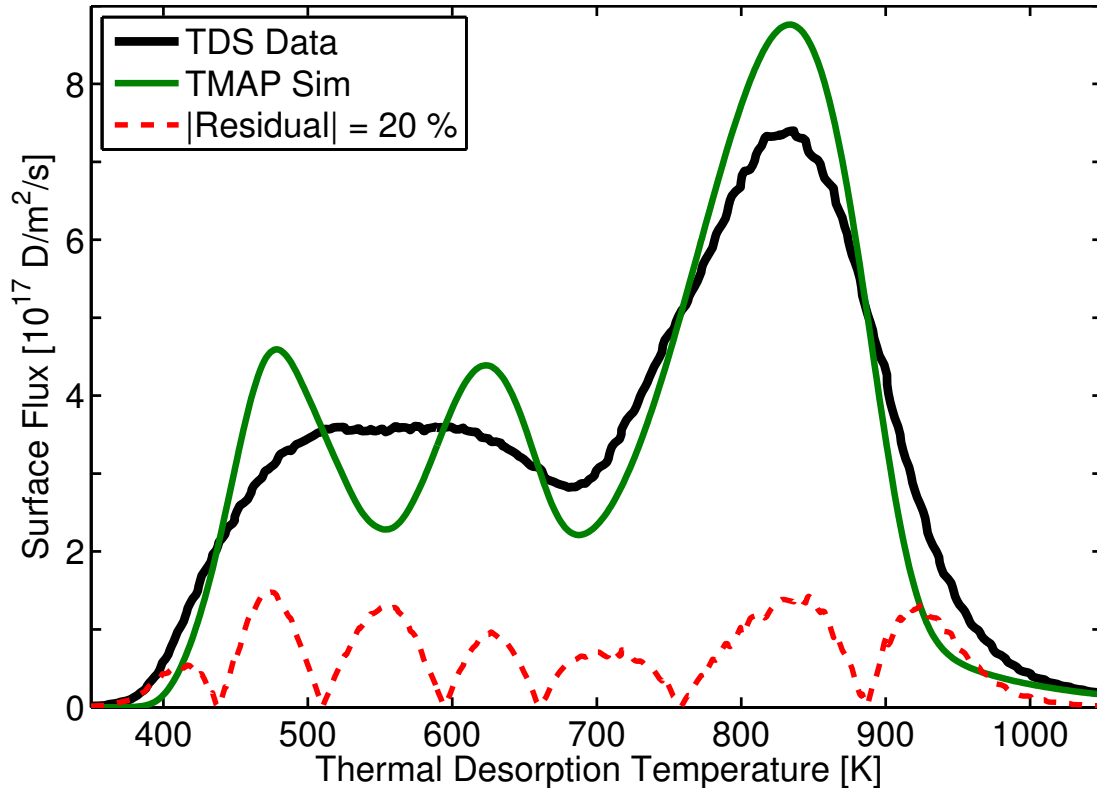
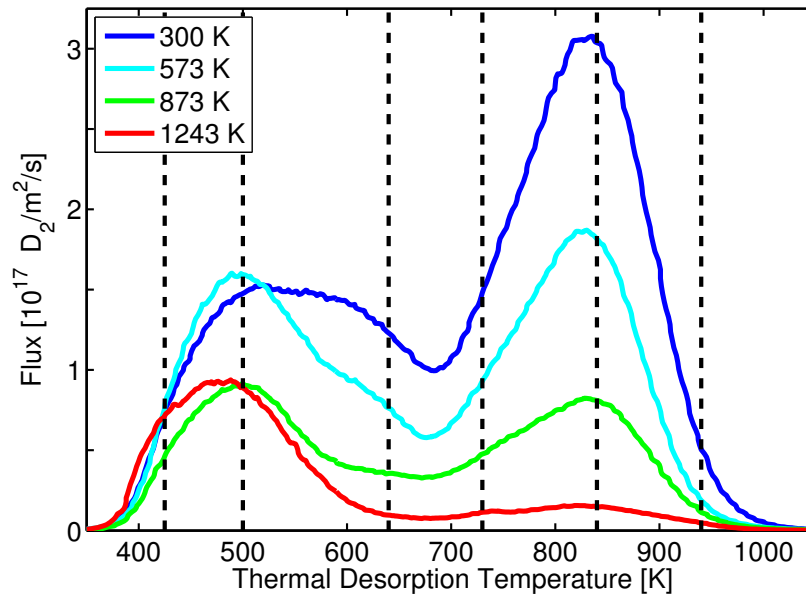


Figure 5.2: The residual error (dashed red) shows the difference between the TMAP simulated release peaks (green) and the experimental TDS data (thick black) with a NRMSE of 0.7.

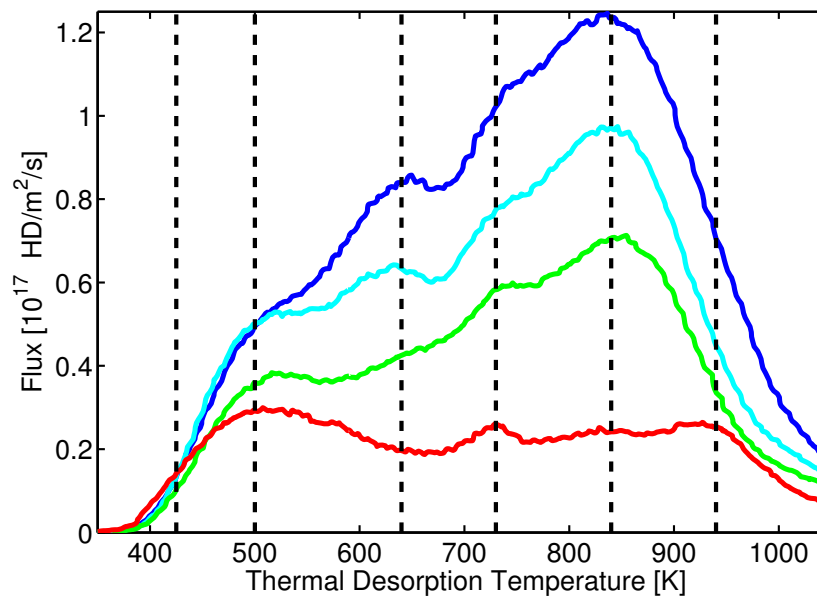
In recent work [45], we showed that three release peaks were clearly observable in the TDS data and well fit by three Gaussians. Initially, the area under each Gaussian was used to constrain the D inventory for each trap. Subsequently, the experimental conditions were simulated with TMAP7 as described above; however, the calculated TDS profile could not accurately replicate both the experimental NRA and TDS data as seen in fig. 5.2. In retrospect, the Gaussians were found to be unphysical in that their width were not the result of only three traps. Relaxing the total area constraint and thereby allowing the traps to vary in concentration does not yield a

better fit. Only when using unphysical values, by significantly decreasing the diffusion coefficient or ignoring the NRA profile to increase the depth of trapped D could we broaden the release peaks to match the experimental TDS data.

Further examination of the TDS data suggests the existence of additional traps. In particular, although not easily seen in the total D flux, the D_2 and especially the HD flux reveal additional release peaks as shown in fig. 5.3. These results suggest the presence of six release peaks with distinct detrapping energies. Here we note that the lowest release peak in the present TDS data is not well resolved and may occur at a slightly lower temperature since it is only partially filled and obscured by the next nearest peak at 500 K. As mentioned previously, the values used to model the detrapping energies associated with these release peaks range from 0.65 to 2.4 eV [12, 59, 38, 34, 32, 37]. The lowest and least resolved peak has an energy below the ~ 1.1 eV associated with the 500 K peak. These two peaks are clearly the dominant traps present in undamaged W. The four higher temperature release peaks are due to the heavy ion induced damage. Assuming that the spatial distribution for these four traps follows the damage profile computed with SRIM as shown in fig. 5.1, and using the previously quoted values, the rest of the detrapping energies appear to be near 1.4, 1.7, 1.9, and 2.1 eV. While these detrapping energies are initially a free parameter, they are constrained by the complete experimental data set for all the TDS profiles annealed at various temperatures seen in fig. 5.3. Motivated by the desire to model the D release from all six traps seen here in a manner that is consistent with NRA profiles and physically plausible diffusion rates for D in solution, we developed the PTTP scheme described below.



(a)



(b)

Figure 5.3: The experimental TDS data for a) D₂ and b) HD fluxes released from dynamically annealed damaged W. Samples damaged with Cu ions at RT (blue), 573 K (cyan), 873 K (green), and 1243 K (red) show reduced D retention. Release peaks identified by eye are marked near 425, 500, 640, 730, 840 and 940 K (vertical dashed black).

5.3 Expanding TMAP7

To expand the capabilities of TMAP7 we developed a PTTP scheme that simplifies the system of equations. Note that the source code was not modified, instead only the input files were adjusted. This scheme works by redefining the traps to be modeled into two classes: a class of actively releasing traps and all remaining traps that are lumped into a single class within a pseudo trap. This class of pseudo traps can actively trap D in solution, but have high enough detrapping energies so that trapped D atoms are not appreciably released at the current sample temperature. All of the primary equations utilized in TMAP are further defined in the TMAP user manual [25]. In this section, we discuss the mathematical model in detail in order to clearly define the pseudo trap concept and explain the applicability of the model to experimental results.

TMAP models the migration of hydrogenic species as the temporal evolution of the solute concentration, C_s . The first term on the right hand side is the one-dimensional Fickian diffusion equation, where D is the diffusion constant:

$$\frac{\partial C_s}{\partial t} = \frac{d}{dx} \left(D \frac{dC_s}{dx} \right) + S_s - \sum_{k=1}^m \frac{\partial C_k}{\partial t} \quad (5.1)$$

The source of solute, S_s , models the implantation of atoms during plasma exposure. The last term accounts for the interaction of solute with m distinct traps, where C_k denotes the filled concentration for the k^{th} trap. The sum of all traps, 1 through m , act as a sink or source when solute is lost to empty traps or released from filled traps respectively. This competition between the trapping rate, R_k^t , and release rate, R_k^r , determines the time dependence of all filled traps:

$$\sum_{k=1}^m \frac{\partial C_k}{\partial t} = \sum_{k=1}^m (R_k^t - R_k^r) \quad (5.2)$$

Between trap sites, the solute concentration diffuses at a rate determined by the diffusion constant renormalized by the lattice parameter, λ . The probability of finding an empty trap of

type \mathbf{k} is the difference between the total concentration of the \mathbf{k}^{th} trap, $C_{\mathbf{k}}^0$, and the filled trap concentration, $C_{\mathbf{k}}$, normalized by the number density, $N_{\mathbf{w}}$. Therefore the total trapping rate, summed over all \mathbf{m} traps, is due to the probability of the diffusing solute finding an empty trap:

$$\sum_{\mathbf{k}=1}^{\mathbf{m}} R_{\mathbf{k}}^t = \frac{D}{\lambda^2} C_s \sum_{\mathbf{k}=1}^{\mathbf{m}} \frac{C_{\mathbf{k}}^0 - C_{\mathbf{k}}}{N_{\mathbf{w}}} \quad (5.3)$$

Noting that the summation can easily be applied to a subset of the total number of traps, we can separate the total trapping rate:

$$\sum_{\mathbf{k}=1}^{\mathbf{m}} R_{\mathbf{k}}^t = \sum_{\mathbf{k}=1}^{\mathbf{n}-1} R_{\mathbf{k}}^t + \sum_{\mathbf{k}=\mathbf{n}}^{\mathbf{m}} R_{\mathbf{k}}^t = \sum_{\mathbf{k}=1}^{\mathbf{n}-1} R_{\mathbf{k}}^t + R_{\mathbf{p}}^t \quad (5.4)$$

Without any approximation, this allows us to expand the total trapping rate into the trapping rate due to individual traps spanning $\mathbf{1}$ to $\mathbf{n} - \mathbf{1}$ and a pseudo trap accounting for all additional traps ranging from \mathbf{n} to \mathbf{m} , as shown in eq. (4). It is useful now at this point to assume, again without loss of generality, that the detrapping energies are ordered from lowest to highest, i.e. $\mathbf{k} = \mathbf{1}$ denotes the lowest detrapping energy, $\mathbf{k} = \mathbf{2}$ denotes the next lowest, and so forth, with $\mathbf{k} = \mathbf{m}$ denoting the deepest (i.e. highest energy) trap. Here we define the pseudo trap concentration as the sum of concentrations across all traps spanning \mathbf{n} to \mathbf{m} for both the total and filled concentrations respectively:

$$C_{\mathbf{p}}^0 \equiv \sum_{\mathbf{k}=\mathbf{n}}^{\mathbf{m}} C_{\mathbf{k}}^0, \quad C_{\mathbf{p}} \equiv \sum_{\mathbf{k}=\mathbf{n}}^{\mathbf{m}} C_{\mathbf{k}} \quad (5.5)$$

With these definitions for the pseudo trap concentration, the trapping rate due to the pseudo trap, $R_{\mathbf{p}}^t$, is given by:

$$R_{\mathbf{p}}^t \equiv \frac{D}{\lambda^2} C_s \sum_{\mathbf{k}=\mathbf{n}}^{\mathbf{m}} \frac{C_{\mathbf{k}}^0 - C_{\mathbf{k}}}{N_{\mathbf{w}}} = \frac{D}{\lambda^2} C_s \frac{C_{\mathbf{p}}^0 - C_{\mathbf{p}}}{N_{\mathbf{w}}} \quad (5.6)$$

Again, we point out that these expressions are exact.

Next we turn our attention to the release of atoms from filled traps. The atoms held in a trap, C_k , have a probability to escape that is a thermally activated Arrhenius process, the release rate coefficient. The pre-exponential factor is the attempt frequency, ν_0 , and the detrapping energy, E_k , is the barrier to activation. The total release rate is then given by the sum:

$$\sum_{k=1}^m R_k^r = \sum_{k=1}^m \nu_0 \exp\left(\frac{-E_k}{k_B T}\right) C_k \quad (5.7)$$

Utilizing the previously defined pseudo trap in eq. 5.5, we would like to separate the release rate the same way as was done for the trapping rate. However, here the summation cannot be pulled through since the likelihood of release from the k^{th} trap is dependent on the corresponding detrapping energy, E_k . As such, the first $n - 1$ terms are exact while the pseudo release rate, R_p^r , must be an approximation:

$$\sum_{k=1}^m R_k^r = \sum_{k=1}^{n-1} R_k^r + \sum_{k=n}^m R_k^r \approx \sum_{k=1}^{n-1} R_k^r + R_p^r \quad (5.8)$$

Based on the release rate shown in eq. 5.7, it is reasonable to conjecture that the release rate for the pseudo trap also follows an Arrhenius dependence on temperature, $\alpha(T)$, and the filled pseudo trap concentration:

$$\sum_{k=n}^m R_k^r \approx R_p^r = \alpha(T) C_p \quad (5.9)$$

To determine the form of the approximation, we consider the two limiting cases. First, the extreme where all traps spanning n to m are completely empty is automatically satisfied by eq. 5.9 because the concentrations vanish. The second extreme of a completely filled pseudo trap, where $C_k \Rightarrow C_k^0$ for $k = n$ to m , yields the following:

$$\sum_{k=n}^m \nu_0 \exp\left(\frac{-E_k}{k_B T}\right) C_k^0 = \alpha(T) C_p^0 \quad (5.10)$$

Solving for $\alpha(\mathbf{T})$ and rewriting equation 5.9, the pseudo trap release rate can be defined in terms of the total trap concentrations and the Arrhenius behavior of each trap spanning \mathbf{n} to \mathbf{m} :

$$\mathbf{R}_p^r \equiv \left[\sum_{k=n}^m v_0 \exp\left(\frac{-E_k}{k_B T}\right) \frac{C_k^0}{C_p^0} \right] C_p \quad (5.11)$$

Once again, C_p denotes the filled pseudo trap concentration, and C_p^0 denotes the total pseudo trap concentration. The result is an effective pseudo trap release rate that is given by the weighted average of the probability per unit time that a trapped particle escapes from the k^{th} trap multiplied by the relative concentration of the k^{th} trap.

With the assumed ordering of the trap energies, the error of the approximate release rate introduced by using this pseudo release rate is dominated by the lowest trap energy:

$$\Delta_{\text{error}} = \sum_{k=n}^m \mathbf{R}_k^r - \mathbf{R}_p^r \approx v_0 \exp\left(\frac{-E_n}{k_B T}\right) \left[C_n - \frac{C_n^0}{C_p^0} C_p \right] \quad (5.12)$$

The primary motivation for using the pseudo trap is to exploit the fact that, relative to the sample temperature, traps with deep detrapping energies (i.e. high temperature release peaks) are nearly indistinguishable in that the release probability is small for all such traps. For instance, one measure of a trap is its residence time, the average time an atom spends in a trap with energy E_k calculated as the inverse of the release rate coefficient. During the implantation phase, at a specific temperature, a pseudo trap can be chosen to span the detrapping energies with residence times approaching or exceeding the total implantation time. This condition ensures that any atom that falls into a pseudo trap stays trapped for the duration of implantation. A diffusion front progresses into the material filling low energy traps partially and fully filling the higher energy traps. The approximation becomes an exact solution when the pseudo trap is completely filled, as seen in eq. 5.12. Furthermore, the low pseudo release rate is accurate until the sample temperature is raised to the point where the pseudo trap begins to appreciably release during the thermal desorption phase. This is when the re-allocation of a given trap from the pseudo trap

population to the active trap population must occur.

5.4 Verification of the PTTP Scheme: Simulating 3 traps with 2 traps

To verify that the PTTP scheme used in TMAP7 can model multiple traps with one pseudo trap, we outline the simulation of a system of 3 traps with well separated detrapping energies using only 2 traps within the TMAP7 model (referred to in this discussion as the pseudo solution). We then compare the pseudo solution with an exact solution obtained by using TMAP7 with 3 traps applied to this same system. This numerical exercise demonstrates the concept and outlines the PTTP scheme. For brevity, we choose to use the experimental conditions and simulation inputs previously outlined in section 2. That is, we reuse the trap concentrations for the best fit with 3 traps to the release of D from a W sample subjected to Cu ion beam damage at RT.

During D implantation in Phase I, traps 2 and 3 have residence times that exceed the total implantation time as seen in fig. 5.4, which shows the total implantation duration (green horizontal line) for a sample held at 383 K (grey vertical line). Thus D atoms that are trapped in these two traps essentially stay there for the duration of the implantation. It thus stands to reason that the populations trapped within these two distinct traps can be viewed as a single population that is trapped for long periods of time. Incorporating this assumption into TMAP7, we simulate the diffusion and trapping of the implantation phase with trap 1 and a pseudo trap composed of traps 2 and 3, yielding the result shown in green in fig. 5.5. Comparing this pseudo solution to the exact result also shown in fig. 5.5 demonstrates that simplifying the set of equations with a single pseudo trap accurately reproduces the exact solution of the D depth profile with a residual error across the entire trapped D profile that is well below 1%.

Next, we apply the TMAP7 model to Phase II of the experiment, i.e. the controlled thermal desorption step. Below a temperature of 555 K there is little deviation between the

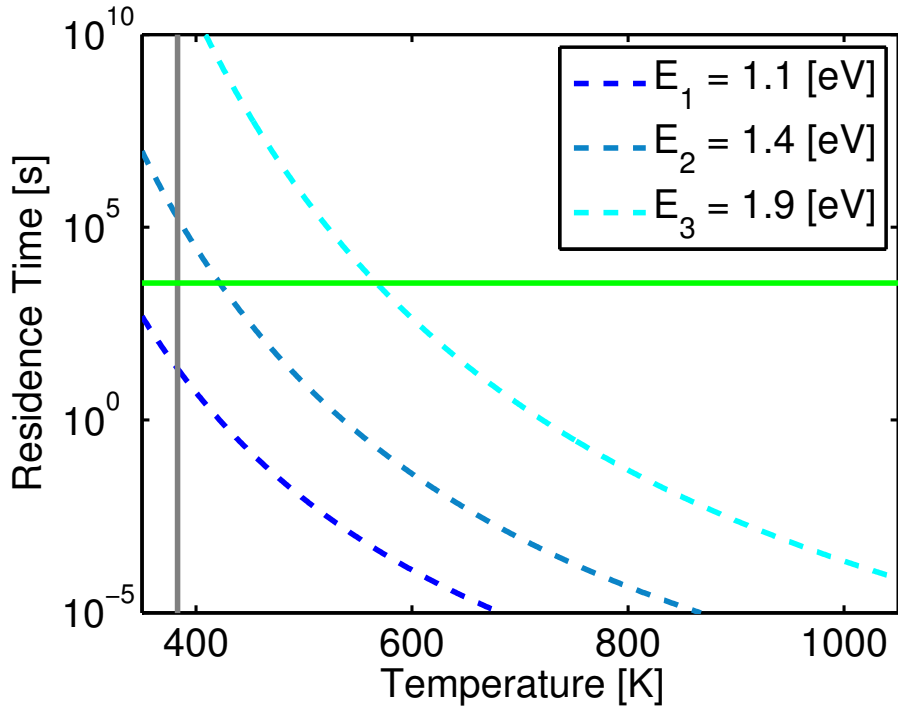


Figure 5.4: The calculated residence times for traps 2 and 3 exceed total implantation time (horizontal light green) for the implantation temperature (vertical grey).

surface flux of the exact and pseudo solutions as shown in fig. 5.6. In this temperature regime only trap 1 is releasing while traps 2 and 3 are not appreciably releasing particles. We note that a transition occurs near a temperature where the pseudo trap begins to appreciably release, in this case a temperature near the trough between the first and second release peaks. We choose to define this as a transition temperature, that is the temperature where the exact and pseudo solutions begin to deviate significantly. As noted previously, the lowest energy trap within the pseudo trap dominates the error and produces the large secondary peak in fig. 5.6.

Fig. 5.7 plots the total inventory of atoms held in each trap as a function of desorption temperature. The trap inventory is a better measure of release than the surface flux, since the latter is coupled to the diffusion and recombination processes. It can easily be seen that the pseudo trap begins to release at a transition temperature of 555 K (vertical dashed orange). Failure to account for the onset of this release process causes the pseudo-solution to then significantly deviate from the exact solution.

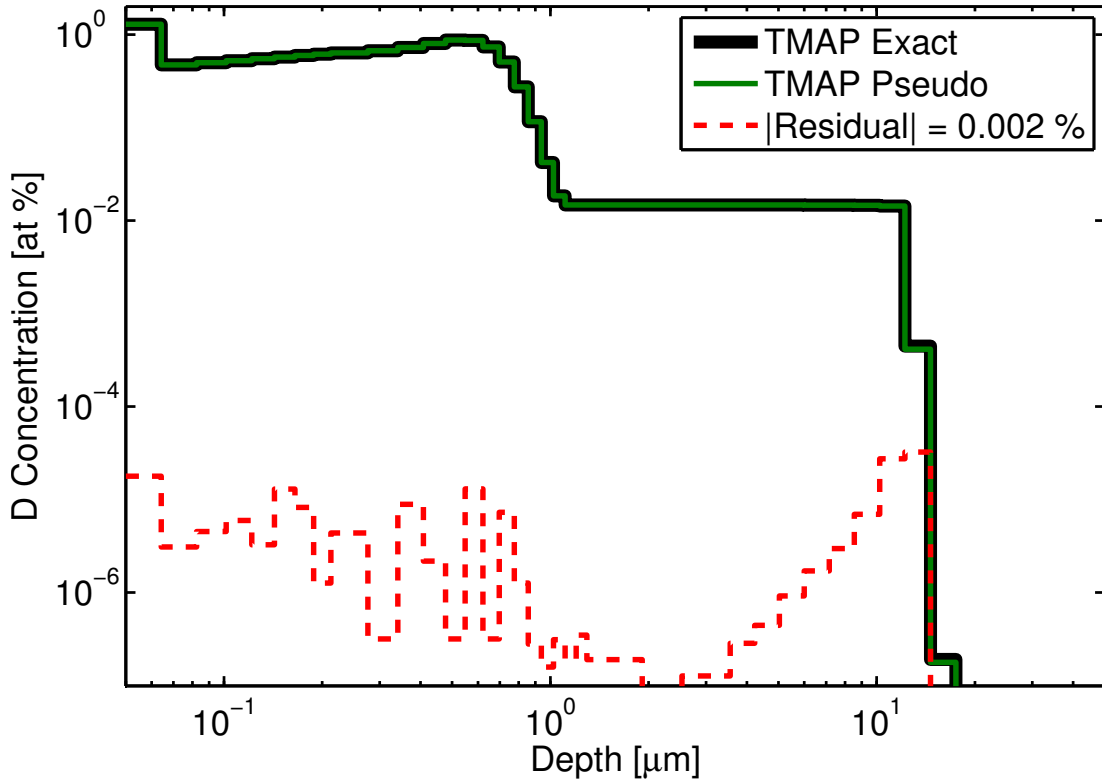


Figure 5.5: The residual error (dashed red) between the exact (thick black) and pseudo (green) solutions for the D depth profile (i.e. after the implantation phase). Note that the exact solution is the sum of D filling traps 1-3, whereas the pseudo solution is the sum of trap 1 and the pseudo trap.

To recover the correct desorption profile, the model must be modified at this transition temperature to account for the onset of release from the higher energy traps. Examining fig. 5.7, we note that at the transition temperature, trap 1 is nearly empty. Above the transition temperature, we can therefore safely neglect this lowest energy trap from the subsequent time evolution of the coupled equations, and in this simple example we can separate trap 2 out of the pseudo trap, leaving trap 3 explicitly within the pseudo trap. Solving the resulting two equations for the evolution of trap 2 and the remaining pseudo trap (which in this simple example only consists now of trap 3) then yields the PTTP scheme TDS profile shown in fig. 5.8. Note that this approximate solution has only a minimal deviation from the exact solution obtained by tracking the evolution of all three traps simultaneously. This simple example therefore demonstrates that, as long as the lowest energy active trap can be considered to become depopulated before the next higher energy

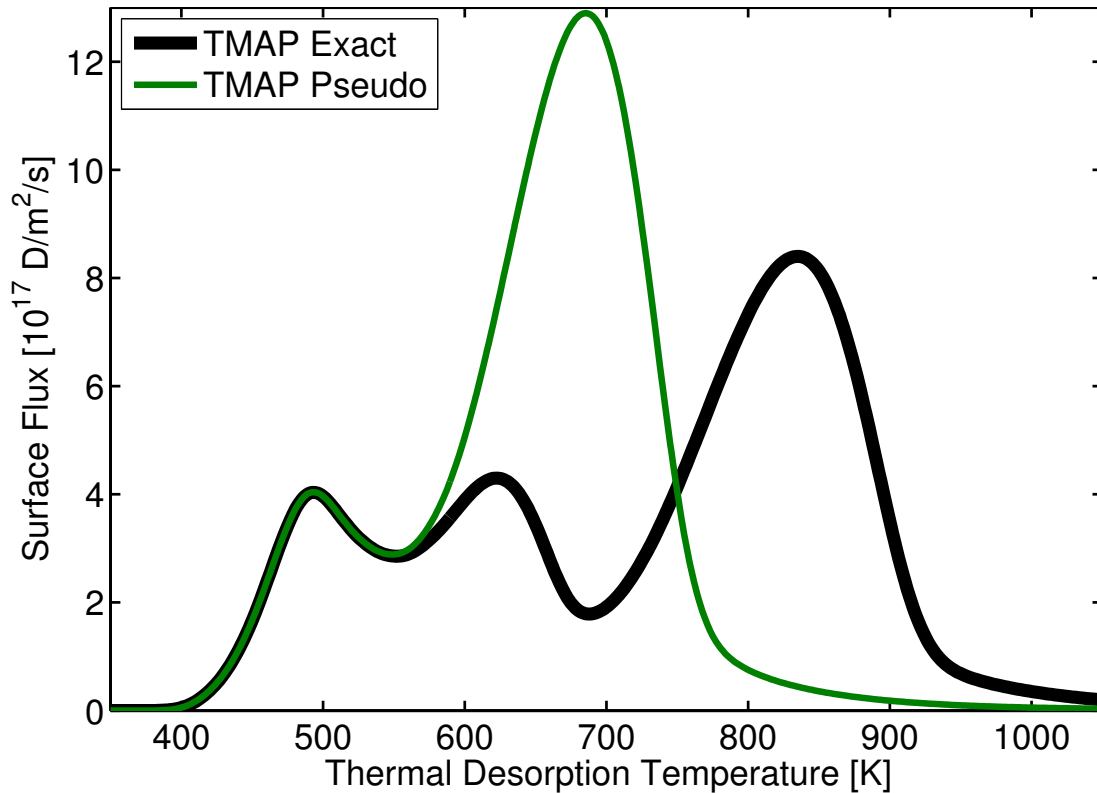


Figure 5.6: The pseudo solution (green) with no temperature partition begins to deviate from the exact solution (thick black) as the temperature approaches the second release peak, which activates the lowest energy trap contained within the pseudo trap.

trap begins to release atoms, then this PTTP scheme can reduce the number of equations to be solved at any given temperature.

5.5 Using the PTTP Scheme to model D retention in damaged W with 6 traps

The results shown in fig. 5.3 shows that the displacement-damaged W has six effective detrapping energies. This then suggests that we take the PTTP scheme further by incorporating additional traps to account for these six traps. Here we describe how the PTTP scheme can be used with TMAP7 to model the trapping and release of D from six distinct traps, and successfully reconstruct the implantation and thermal desorption of D in the RT damaged W sample described

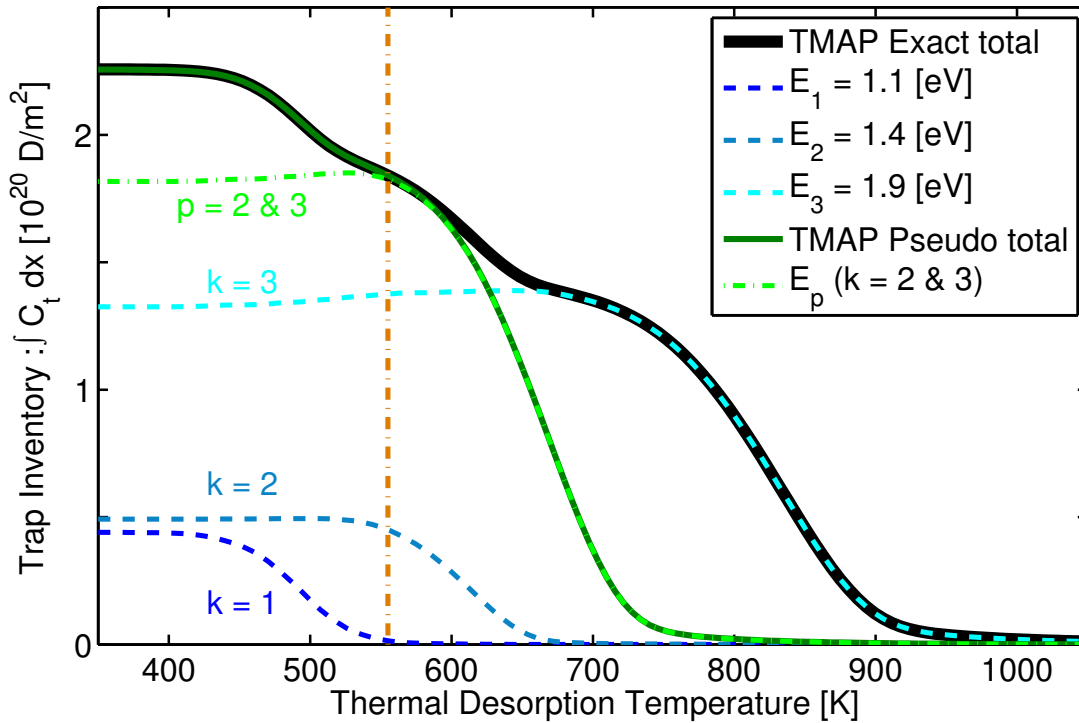


Figure 5.7: The D inventory of each trap displays the trapping and release directly, without the effects of diffusion and surface recombination shown with the surface flux in Fig 6. The total inventory for the exact solution (thick black) is the sum of traps 1-3, whereas the pseudo solution (dark green) is the sum of trap 1 (dashed blue) and the pseudo trap (dashed light green). The total for the exact and pseudo solutions deviate near the peak of the pseudo trap at 555 K (vertical dashed orange).

in [45].

As previously stated for the 3 trap TMAP simulation, the three spatial zones for traps have respective concentrations for each trap. In this case, for six traps, the total number of adjustable concentrations is 18; we can simplify the modeling as follows. First it is reasonable to assume all 6 traps have a spatially uniform intrinsic background concentration. Second, from the undamaged W control sample, the near surface D concentration peak seen in the experimental NRA profile only shows a significant TDS release peak at low temperature. This observation then suggests that traps with the first three energies (0.9, 1.1, and 1.4 eV) are associated with near-surface plasma ion implantation induced defects. These are likely dislocations for the two lower and mono-vacancies for the last detrapping energy[32] Similarly, comparing the TDS release peaks

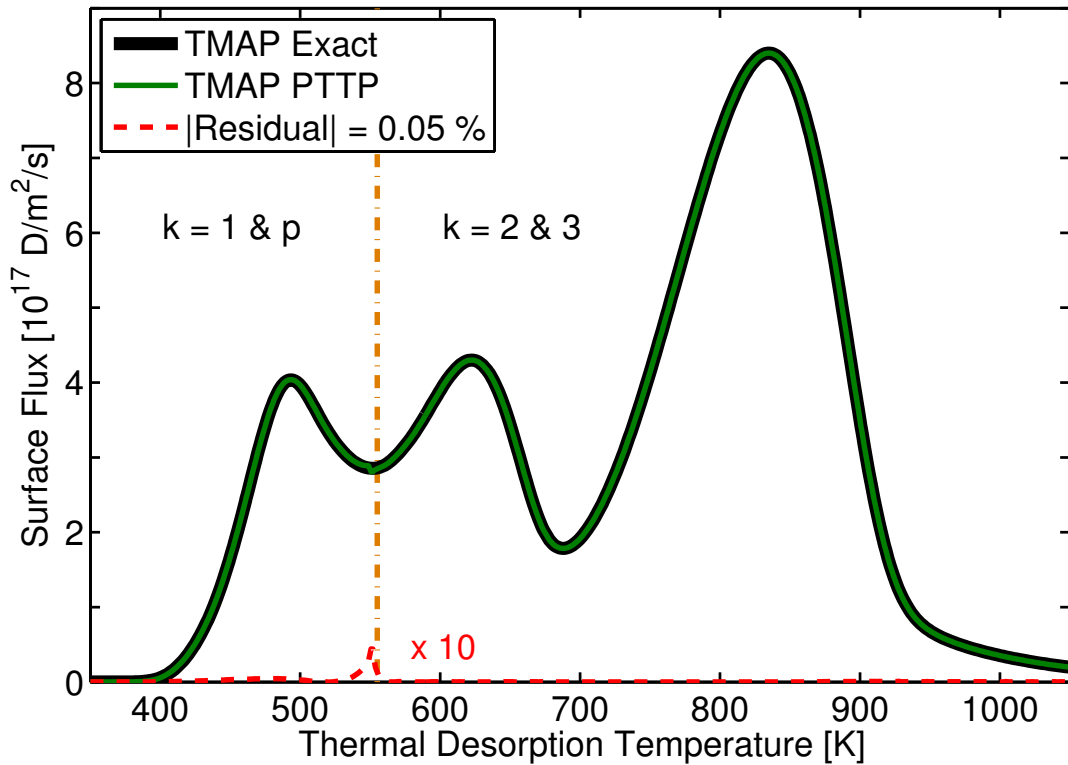


Figure 5.8: PTTP scheme (green) applied using 2 traps at any given temperature. Below 555 K (vertical dashed orange), traps 1 and pseudo are modeled. Above 555 K, only traps 2 and 3 are modeled. The residual error (dashed red), magnified by 10, with respect to the exact solution (thick black) occurs primarily near the transition.

from undamaged and damaged samples suggests that only traps 3-6 are associated with energetic heavy ion induced damage. Therefore the number of free parameters is reduced from 18 to 13. Noting the previously quoted detrapping energies in similar experiments [12, 59, 38, 34, 32, 37], the energy values are selected to correspond to the release peaks seen in the TDS data as shown in fig. 5.3. We can then use these energies together with the known material properties to estimate the residence times for these traps. We find that during the D implantation phase, traps 3-6 fulfill the residence time requirement for the PTTP scheme as seen in fig. 5.9 and thus we can lump these traps together into a single pseudo trap that will represent the net trapping effect due to all high energy traps. Note that all traps included in the pseudo trap have even longer residence time when held at RT. Only the lowest energy trap modeled, $k = 1$ may have appreciable release in the time between implantation and NRA.

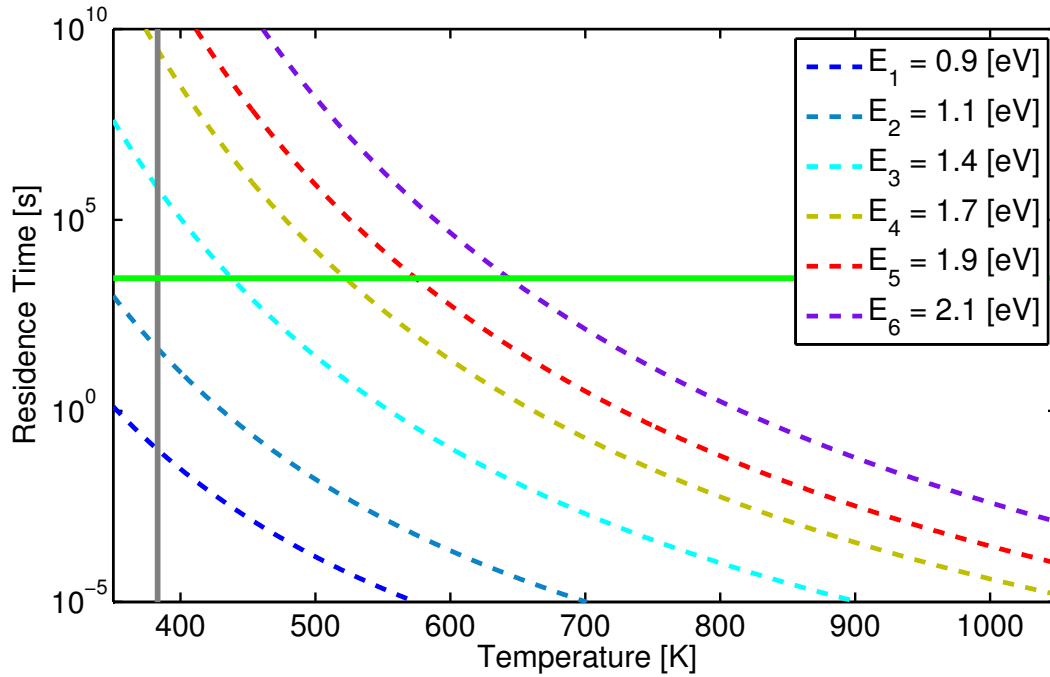


Figure 5.9: The calculated residence time for traps 3-6 exceed the total implantation time (horizontal light green) for the implantation temperature (vertical grey). Thus traps 3-6 can be well modeled as one pseudo trap in the implantation phase.

Modeling active traps 1 and 2, together with this pseudo trap accounting for the higher energy traps (which do not release at the temperature of the implantation process) within TMAP7 then results in the modeled D profile arising from the implantation phase shown in fig. 5.10. Comparing the result to the experimental NRA data in fig. 5.10 shows reasonably good agreement, both in the first $\sim 1 \mu\text{m}$ region where most of the trapped D resides and deeper into the material where D is trapped in the lower level of intrinsic traps.

Fig. 5.11 illustrates the total D held in each trap during the TDS release phase. Here the total inventory for trap k is simply the spatial integration of that traps filled concentration, C_k , inferred from fitting the NRA profile as shown above together with the measured TDS release data. Initially the same trap scheme as used in the implantation is followed, with traps 1 and 2 modeled as active traps and the pseudo trap containing traps 3-6 (which at low temperature do not release any D). As the temperature increases to 470 K, trap 1 is nearly empty, and the pseudo trap begins to significantly release D. At this transition temperature, trap 1 is removed from the

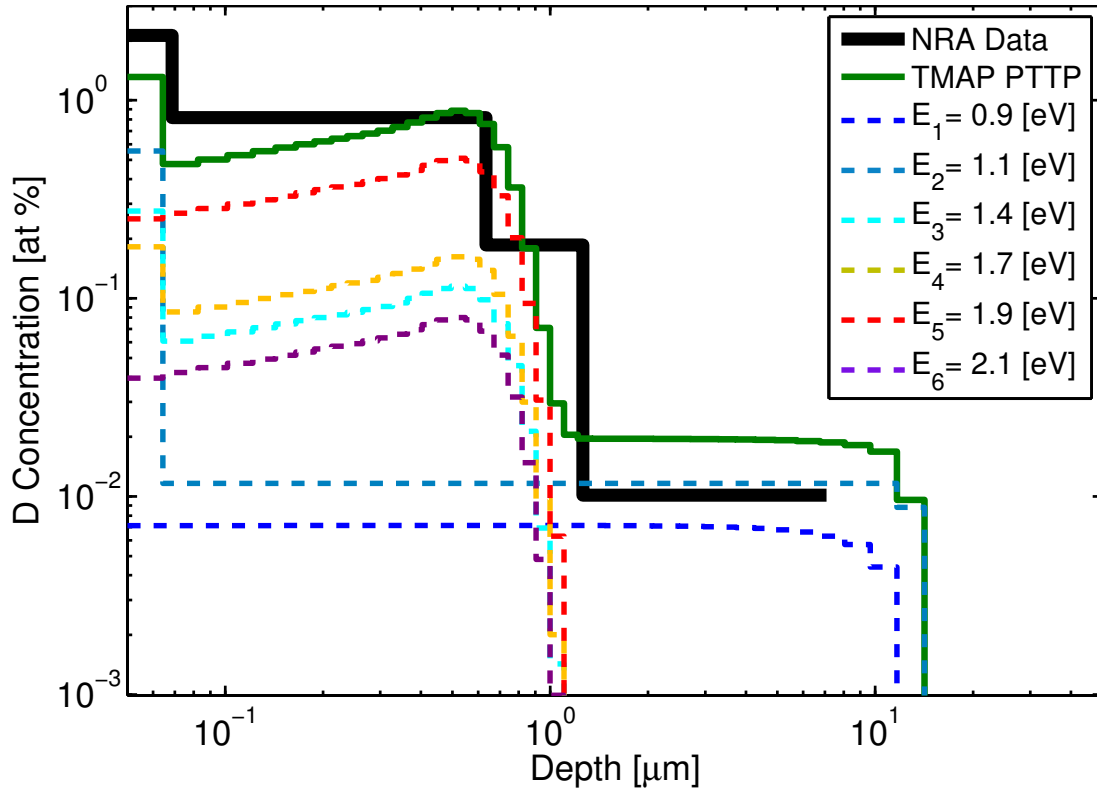


Figure 5.10: The total D concentration simulated with PTTP (green) is the sum of all 6 trap concentrations (dashed lines) after the implantation phase. The pseudo trap is separated into its constituent traps 3 through 6. The NRMSE for the PTTP simulation is 0.7 with respect to the experimental NRA data (thick black), where 1 is a perfect fit.

simulation and the pseudo trap is adjusted to remove trap 3, which now becomes an active trap that releases (and traps) D atoms. The simulation continues into the next temperature segment with traps 2 and 3 as well as the adjusted pseudo trap, which now contains the summation of traps 4 through 6. The process continues with each additional temperature segment as shown in fig. 5.11, each time removing the lowest remaining detrapping energy and adjusting the pseudo trap until eventually only traps 4, 5, and 6 remain in the final segment. The resulting desorption profile is compared to the experimental TDS data shown in fig. 5.12. The results show that the residual error was significantly reduced from 25% to 4% utilizing 6 traps instead of 3.

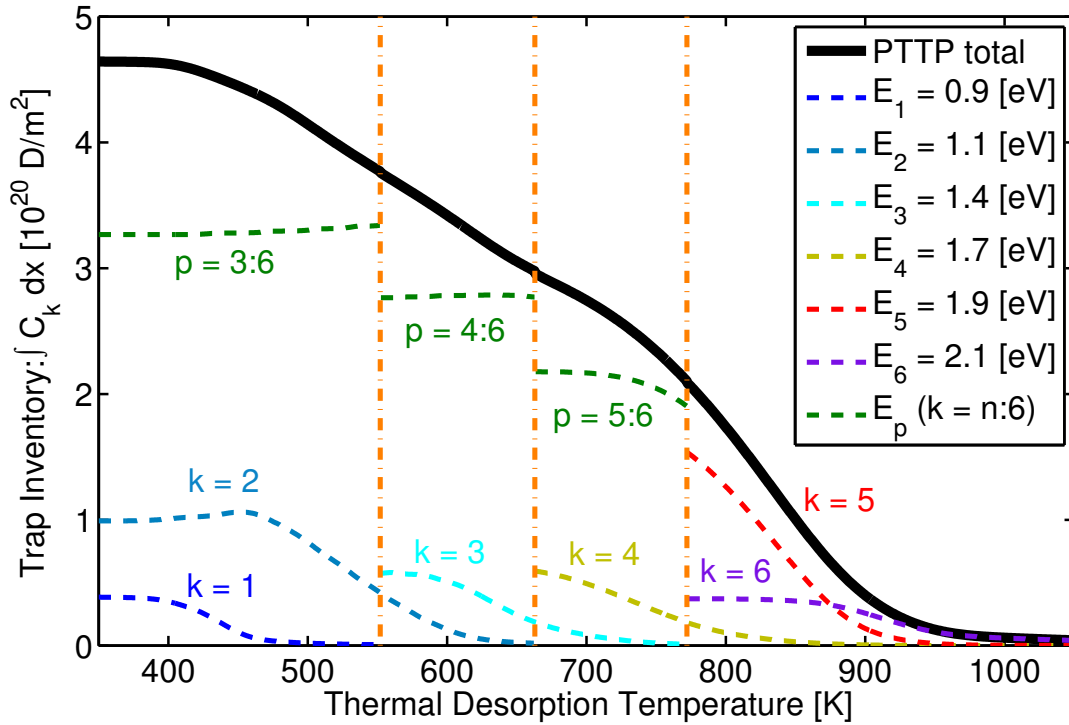


Figure 5.11: The total D inventory in each trap as well as the total inventory (thick black). The discontinuity of the pseudo trap (dashed green) is due to removing the lowest energy trap in the pseudo trap at each transition temperature (vertical dashed orange). Also note that the lowest energy trap in each segment is neglected as it asymptotically approaches zero concentration at each transition temperature.

5.6 Discussion

The applicability of this PTTP scheme is dependent on the overlap of release from traps with the lowest and the highest detrapping energies within a temperature segment. The error has two sources. First, neglecting the lowest detrapping energy by removing it from the set of coupled equations at the transition temperature cuts off the asymptotic tail of its release. Second, approximating the highest detrapping energy which is beginning to release within a temperature segment (i.e. the lowest detrapping energy within the pseudo trap) introduces the previously quantified error in eq. 5.12. The error increases when the tail of the release from the lowest energy trap overlaps significantly with the onset of release from the pseudo trap. That is, the detrapping energies and thus the release rate must be sufficiently separated. For instance, a separation of

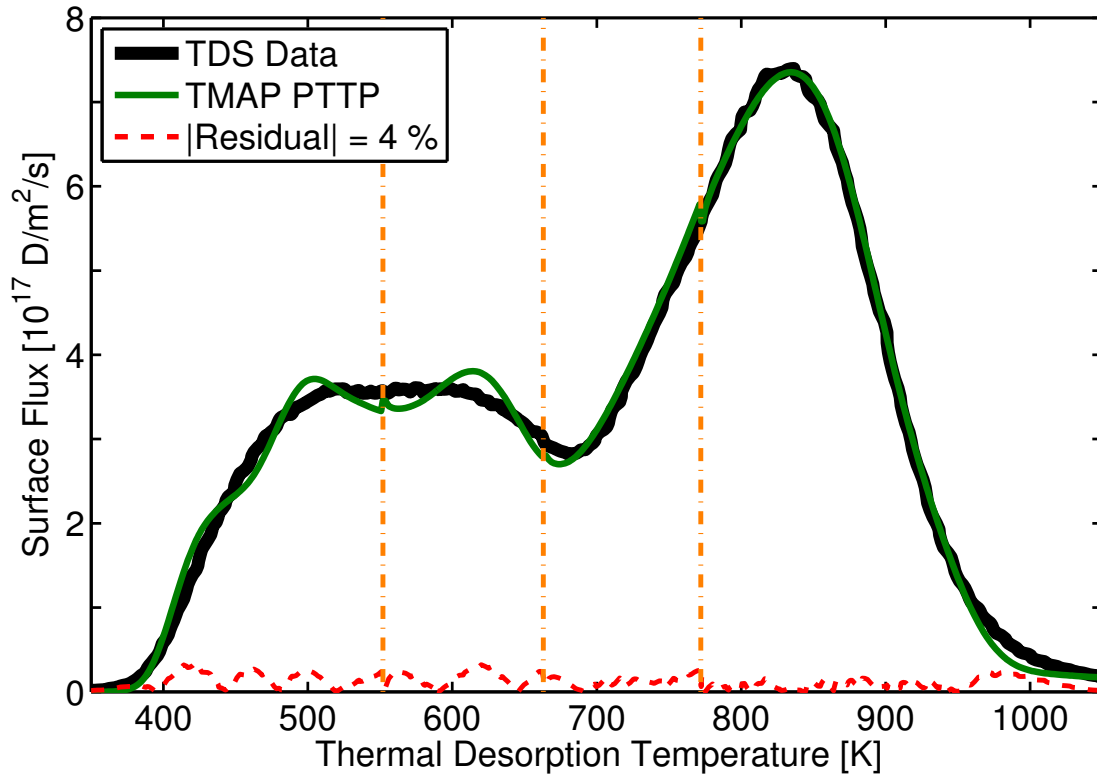


Figure 5.12: The full PTTP simulation (green) with 6 traps compared to experimental RT damaged W (thick black). The residual error (dashed red) is 4% and the NRMSE is 0.95.

0.05 eV while using 3 traps at a time would result in significant overlap of release during the TDS phase for the pseudo and lowest trap. Presented in fig. 11 and 12, the ~ 0.2 eV separation of detrapping energies ensured the lowest energy trap was nearly depopulated before the appreciable release of the pseudo trap. Unlike simply summing the release of uncoupled traps, this scheme retains the majority of the coupled trap interactions that occur.

The same methodology can be used to model multiple traps for other materials/solutes as well as adapted to other migration codes to improve the speed of simulations. It is well known that the additional coupled differential equations can significantly increase computation time. Both a high number of steps chosen in the discretized spatial grid or a large number of inactively releasing traps would be reasons to implement the method. That is, the computations saved using this method can be weighed against the additional computation needed to verify what temperature to transition and adjust the pseudo trap.

We note that there are other computational codes capable of solving systems involving more than three traps, but few of them have been recognized as verified and validated over as wide a range of experiments as TMAP. There are also several advantages to the use of TMAP7. A key feature of TMAP is the speed of simulations that can be run on a single processor. Lastly, we reiterate that the PTTP scheme does not fundamentally change the reaction-diffusion equations used in TMAP7. Instead, the scheme provides the framework to reduce the number of equations needed to model the trapping and release of solute atoms.

5.7 Summary

Utilizing TMAP7, we showed that three detrapping energies can not accurately represent the observed NRA and TDS profiles from our recent experiment [45]. By re-evaluating the HD flux of the TDS profiles, at least 6 distinct release peaks are observable. In order to simulate the experiment with only 3 traps at a given time, we developed a PTTP scheme to model multiple traps with a reduced number of equations. We further outlined the criteria by which to switch off inactive traps and track the most active traps. While this method introduces an error into the implantation and TDS phases, we show how to minimize the error through partitioning the temperature into segments. Lastly, the PTTP scheme was applied to simulate and experiment and shown to fit the data well.

5.8 Acknowledgments

This work was supported by U.S. Department of Energy under DE-FG02-07ER54912 and DE-SC0001999 as well as the University of California Office of Presidential Research Fund under 12-LR-237801. Chapter 5, including text and data, is in part a reprint of the material as it appears in M.J. Simmonds, J.H. Yu, Y.Q. Wang, M.J. Baldwin, R.P. Doerner, G.R. Tynan, Expanding

the Capability of Reaction-diffusion Codes using Pseudo Traps and Temperature Partitioning: Applied to Hydrogen Uptake and Release from Tungsten, J. Nucl. Mater. (2018). The dissertation author was the primary investigator and author of this paper.

Chapter 6

Isolating the Detrapping of Deuterium in Heavy Ion Damaged Tungsten via Partial Thermal Desorption

6.1 Introduction

The retention of tritium in Plasma Facing Materials (PFMs) is an important issue due to both safety concerns as well as maintaining the fuel cycle in fusion devices [36]. The production of fusion neutrons will lead to the degradation of PFMs throughout the bulk of the material. In order to study the effects of neutron damage and tritium exposure, heavy ion damage and deuterium are used as proxies, respectively. The guidelines for the use of heavy ions to simulate neutron damage are outlined in [15].

Experiments conducted to study displacement damaged W typically use NRA and TDS to quantify D retention. NRA probes the D distribution across the near-surface region up to depths of $\sim 10 \mu\text{m}$, whereas TDS measures the released D from throughout the bulk. NRA can not differentiate between trapped and solute D atoms located between W lattice sites, nor can it

directly determine detrapping energy or trap type. The release peaks in TDS data are correlated to both the spatial position and detrapping energy of a particular type of defect because the measured release rate from the surface is the result of the escape of D from multiple types of defects, each having a particular detrapping energy, followed by subsequent diffusion through the material to reach the surface where recombination occurs. The resulting TDS data may display one or more effective release peaks, due to multiple defects with nearby detrapping energies. Experiment and theory have produced detrapping energies spanning 0.9 to 2.4 eV [31, 30], with dislocations likely having a detrapping energy ranging from 0.9 to 1.3 eV, mono-vacancies having a detrapping energy of ~ 1.4 eV, and vacancy clusters having detrapping energies ranging from 1.9 to 2.4 eV. These values are dependent on both the attempt frequency, generally assumed to be 10^{13} s^{-1} , as well as the method and value used to model surface recombination.

Previous studies [30] have used varied sample temperatures during plasma exposure to selectively populate defects. At higher sample temperature, defects with lower detrapping energies can not be effectively filled with D if the release rate is large relative to the trapping rate. The increased temperature may also significantly influence the evolution of defects to be populated, complicating the interpretation of such experiments. For instance, mono-vacancies may be partially annealed as they recombine with mobile interstitials, and above ~ 600 K the vacancies become mobile and can further anneal or agglomerate into clusters [40]. Thus, at high sample temperatures, the assumption of a static population of defects during plasma exposure may no longer be valid. In addition, the increased diffusivity of D at higher temperature will likely increase retention as deeper intrinsic traps become filled. This results in the broadening of each release peak. Therefore the direct comparison of samples prepared with various sample temperatures during plasma exposure is not straightforward.

To better quantify the spatial location and detrapping energies associated with various defects, we devised an experimental approach to sequentially depopulate each defect according to detrapping energy. Whereas previous experimental studies that attempted to model NRA and

TDS data have assumed specific detrapping energies and spatial concentrations, this approach aims to constrain both quantities and test if a discrete detrapping energy model can reproduce the experimental data. In this approach, all damaged samples have the same initial conditions prior to pTDS. By performing pTDS and holding the sample at a fixed elevated temperature, defects with appreciable release rates at that temperature will depopulate. The released D then either travels further into the material, filling traps with higher detrapping energy, or reaches the surface to escape the sample. NRA is carried out after each pTDS procedure to provide a spatial profile of the remaining D atom concentration. The resulting data allows us to then infer the spatial profile with respect to detrapping energies and densities from each spatial zone attributed to plasma-induced, heavy ion beam induced, and intrinsic trap sites.

Within the heavy ion damage region there is a discrepancy between some experimental NRA data and SRIM predicted damage profiles. NRA data from plasma exposure at elevated sample temperatures [3, 50, 59] do not display a significant near-surface peak and are spatially commensurate with the SRIM calculated dpa profile. Yet lower sample temperature during plasma exposure yields a D concentration in the near-surface that can not be explained by plasma induced defects alone. The deviation in trap profile and consequently D concentration measurements is likely due to a different spatial profile for low detrapping energy defects.

6.2 Experiment

6.2.1 Sample Preparation

W samples originated from a certified 99.95 wt.% powder metallurgy polycrystalline rod, 6 mm in diameter and cut into disks 1.5 mm thick. The plasma facing surface received a mirror-like finish by successive polish treatments ending with a 3 μm grit. Contaminants from polishing were removed in successive ultrasonic baths of acetone followed by ethanol. Next, the samples were annealed at 1173 K for 1 hour in a vacuum chamber below 10^{-4} Pa.

As noted in [45], a broken W sample displayed elongated grains perpendicular to the surface with dimension on the order of 10 μm parallel to the surface, as viewed by a scanning electron microscope. The maximum annealing temperature is well below the recrystallization temperature, leaving an intrinsic level of various defects throughout the bulk of the sample.

6.2.2 Heavy Ion Damage

The previously prepared W samples were irradiated with 5.0 MeV Cu^{2+} ions at the TOF beamline of the tandem accelerator laboratory at Max-Planck-Institut für Plasmaphysik in Garching (IPP) while under a low vacuum of 10^{-6} Pa and held at 295 K with a water-cooled sample holder. Details of the setup can be found in [43]. The beam had a full width at half maximum of 2 mm, and was rastered over the samples to achieve lateral homogeneity. The implanted Cu dose was 1.215×10^{18} ions/ m^2 with an average flux of 2.4×10^{15} ions/ m^2/s , which maintained an impurity level below the intrinsic Cu level [8]. In accordance with Stoller *et al.* [48], the Quick Kinchin-Pease option and a displacement damage threshold of 90 eV were used to calculate the displacement profile in SRIM shown in Fig. 6.1 with a peak dpa of 0.12. According to the simulation, on average each energetic Cu ion is estimated to produce a collision cascade with over 5,600 W lattice displacements. This sample temperature during plasma exposure was low enough to avoid the annealing of displacement damage that we have reported in previous work [45].

6.2.3 D₂ Plasma Exposure

One undamaged sample, as well as the identically prepared Cu ion irradiated samples, were exposed to D₂ plasma with a neutral pressure of 0.7 Pa in the PISCES-E device, a plasma etcher with a 13.56 MHz RF source [53]. The air-cooled sample holder was negatively biased to implant D with an ion impact energy of 110 eV and maintained the sample at 373 K as measured

by a thermocouple in contact with the rear of the sample. An RF compensated Langmuir probe inferred an average flux ($\Gamma_{incident}$) of 1.8×10^{20} ions/m²/s uniformly across the surface of the sample holder as detailed in [51]. Each sample received a total fluence of 10^{24} D/m² after ~ 1.5 hours.

6.2.4 Partial TDS

The plasma-exposed samples were kept at room temperature for 25 days before being subjected to pTDS. Samples were mounted on the tip of a thermocouple within a vacuum below 10^{-6} Pa. Parabolic mirrors focused the heat from infrared lamps on the sample surface. A programmable controller was set to heat the samples at a constant rate of 0.5 K/s before plateauing for 2.5 hours at a particular peak-and-hold temperature. That is, instead of completely desorbing the sample as in a typical TDS run by heating the samples to a peak temperature near 1300 K, temperatures well below that were chosen to selectively depopulate the corresponding lower energy traps. In what follows, the label for each pTDS sample refers to this peak-and-hold temperature (e.g. “pTDS at 467 K”). It should be noted that two control samples were not thermally desorbed at this stage, one without pTDS labeled “No pTDS” and one without heavy ion damage, “No Cu”.

6.2.5 NRA

NRA was performed on each sample at IPP Garching 20 days after the pTDS procedure. The $D(^3\text{He},p)^4\text{He}$ nuclear reaction measured the depth profiles of the remaining D concentration as prescribed by Mayer with a detector positioned at a scattering angle of 135° [28]. A ^3He ion beam was used to probe the first $\sim 6 \mu\text{m}$ of D implanted in W with decreasing energies of 3.5, 2.5, 2.0, 1.65, 1.5, 1.3, 1.1, 0.8, and 0.6 MeV. Both the energy spectra of the resultant protons and alphas were captured in solid state detectors to determine the depth distribution of the retained

D. Relative to the protons, the resulting alpha particles are only detectable for low ^3He beam energies since they receive less energy from the nuclear reaction and lose more energy to inelastic Coulomb interactions while escaping the sample. Probing with a ^3He energy slightly below and above the cross section peak (i.e. 0.6 and 0.8 MeV) enhances the near-surface resolution of D concentration. In addition to detecting both product ions, the various sources of straggle are minimized with relatively low probing energies. As a result, we can resolve D trapped within the near-surface (~ 100 nm) region; deeper NRA results have poorer spatial resolution. Using the NRA data, both SimNRA and NRADC were then employed to determine the most probable D concentration as a function of depth [28, 42].

6.2.6 Final TDS

A further 18 days elapsed between NRA and the final TDS run where all samples were heated with a constant 0.5 K/s ramp rate up to a peak temperature above 1300 K to ensure full desorption of D. The partial pressures of H_2 , HD, and D_2 were measured with a quadrupole mass spectrometer (QMS). The thermally desorbed particle flux was calculated by converting the QMS measured partial pressure via a calibrated D_2 leak. The total D flux was calculated as described in further detail by Yu [58], as the sum of the HD and twice the D_2 flux. Note that the HD flux was calibrated to the D_2 leak, without any further correction for ionization efficiency. Since the detection efficiency is expected to increase for ions of lighter mass this procedure leads to a small overestimation of the total D flux. However, as HD contributed only an average of 28% to the total D flux this is of minor importance. As described previously [45], variable ambient laboratory humidity, temperature, and length of vacuum break influence the water content adsorbed to the TDS chamber walls. This leads to a significant H_2 background signal that was scaled to and subtracted from the raw HD and D_2 signals.

6.3 Results

After the pTDS procedure was applied to each sample, and prior to final TDS, the spatial profile of D concentration in each sample was measured with NRA. In Fig. 6.1, the experimental data displays a monotonic decrease in D concentration as the pTDS peak-and-hold temperature is increased. The estimated error determined by NRADC as a concentration range is indicated as the corresponding transparent colored region in the figure. The NRA profiles have distinct spatial zones, labeled I-III respectively: zone I composed of the near-surface ($\sim 0.1 \mu\text{m}$) region, zone II composed of the Cu damage ($\sim 1 \mu\text{m}$) region, and zone III composed of the bulk of the samples depth. Within zone I, the control sample without heavy ion beam damage (solid black) displays a peak D concentration near 1.5 at. % that decays exponentially with a characteristic length of $0.05 \mu\text{m}$. The intrinsic defects left after sample preparation annealing (below the recrystallization temperature) are assumed to have a uniform distribution throughout the bulk, zone III. For Cu ion beam damaged samples, the dominant contribution to total D retention is seen in zone II. The D concentrations for pTDS temperatures of 525 K and higher largely coincide with the SRIM predicted damage profile (dot-dashed orange). The “No pTDS” and the 467 K pTDS samples have profiles that are more heavily weighted closer to the surface. The small, but measurable, D level near $2 \mu\text{m}$ suggests the D diffusion front reached beyond the SRIM profile.

In Fig. 6.2, the surface flux of D atoms released from the W samples during each pTDS and final TDS are shown as dashed and solid lines respectively. The pTDS profiles (dashed lines) display the sequential removal of D from traps with increasing pTDS temperature, and exhibit a sharp drop in released D flux when fixed at their peak-and-hold temperature. This D flux plotted against time instead of temperature (not shown here) displays an exponential decay during the pTDS peak-and-hold, indicating the gradual depopulation of traps that exhibit a significant release probability at the pTDS peak-and-hold temperature. The first and weakest D filled traps are highly sensitive to surface conditions and storage time in between D implantation and TDS [34, 10].

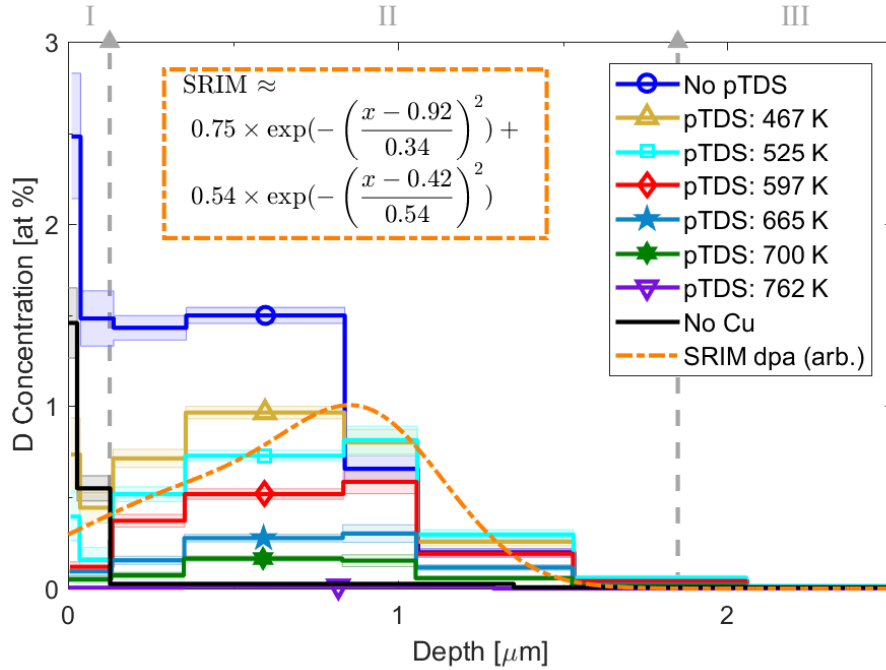


Figure 6.1: The D concentration measured through NRA decreases with increasing pTDS temperature. The SRIM predicted trap profile (dot-dashed orange) for 5 MeV Cu^{2+} displays a peak near $\sim 0.9 \mu\text{m}$ and shown here scaled to 1. Note that the experimental dose resulted in a calculated peak dpa of 0.12. A two Gaussian fit to the SRIM profile is defined by the normalized function. Dashed silver vertical lines indicate the approximate transition between zones I-III.

Whereas the pTDS samples were thermally desorbed after ~ 1 month, the control samples waited ~ 2 months. That extra storage time likely led to the “No pTDS” control (dark blue) having a lower first peak than in the other Cu damaged samples. The “No pTDS” control sample shows a significant increase in the amount of released D as compared to the “No Cu” control sample (black) for all temperatures below 1000 K. The initial release of the “No pTDS” control sample begins near the 373 K plasma exposure sample temperature. For all cases, it appears that the pTDS peak-and-hold temperature is at least 40 K lower than the leading edge of the initial release temperature during the subsequent final TDS. For example, the sample with a pTDS peak-and-hold temperature of 467 K (dashed gold) only begins to appreciably release D when the temperature exceeds 510 K during the subsequent final TDS (solid gold). This separation indicates that the underlying assumptions of the PTP scheme [46] can be used to distinguish and isolate traps with progressively higher release energies. As a result, taken together the NRA

and TDS data can be used to quantify the location and concentration of D residing in each trap, as illustrated in the following discussion.

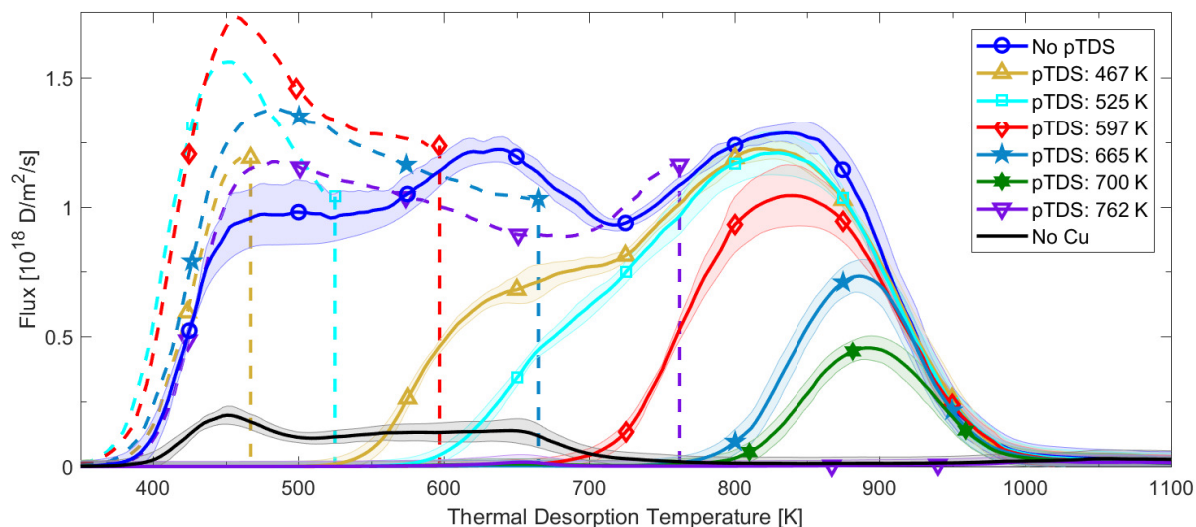


Figure 6.2: The D surface flux during pTDS (dashed) and the final TDS (solid) are plotted with respect to a 0.5 K/s linear heating ramp. Once pTDS samples reached a specific peak-and-hold temperature, the flux during the 2.5 hr peak-and-hold decays exponentially in time and approaches zero at this fixed temperature.

Note that in Fig. 6.1, the NRA profiles for the control samples labeled “No Cu” and “No pTDS” have a high D concentration located in zone I. In the “No Cu” case this zone I population forms the majority of retained D inventory, while for the “No pTDS” case (which did suffer Cu ion beam damage) the zone I retained population sits on top of a significant retained D inventory located deeper in zone II. Comparing the “No pTDS” and the 467 K and 525 K pTDS cases in Fig. 6.1, we observe that the zone I retained D inventory is largely reduced, and is undetectable for the 597 K pTDS case shown in red in Fig. 6.1. Furthermore, the “No Cu” (solid black) and 597 K (solid red) final TDS curves in Fig. 6.2 display a crossing near 700 K. These observations show that the majority of the “No Cu” sample D inventory that was trapped in zone I has been completely released at 700 K whereas the ion beam damaged sample that underwent a 597 K pTDS treatment is just beginning to release D at this temperature. Considering Fig. 6.1 and Fig. 6.2 results together, we can then conclude that the zone I traps are induced by the plasma and

have relatively low detrapping energies that release at temperatures below 700 K. Furthermore, we can conclude that most of the increased inventory in ion beam damaged samples is located in zone II and releases at higher temperatures. These two experimental observations suggest that the NRA, pTDS, and final TDS approach used here may permit the inference of both spatial distribution of traps with differing trapping energies. We take up a deeper examination of the utility of the combined NRA, pTDS, and final TDS data sets after examining the self-consistency of the overall retention data emerging from these combined techniques.

By integrating the NRA profile over the depth into the material we can determine the remaining retained D inventory for each pTDS case. The result of this analysis is shown by the black circle symbols in Fig. 6.3, and shows a gradual reduction in the retained D as the pTDS peak-and-hold temperature is increased. Likewise, by integrating the pTDS release histories shown by the dashed curves in Fig. 6.2, we can determine how much D was released for each pTDS case. The result of this analysis is shown by the filled blue upright triangle data points in Fig. 6.3, and shows a gradual increase in the amount of released D with increasing pTDS peak-and-hold temperature. Finally, integrating the final TDS release curves shown by the solid curves in Fig. 6.2, we can determine the remaining D inventory throughout the bulk of the material. The result, shown as the inverted red triangles in Fig. 6.3 shows a gradual decrease in retained D inventory as the pTDS peak-and-hold temperature is increased, and is in good quantitative agreement with the NRA results. The sum of the pTDS and TDS data (purple diamonds) provides an independent measurement of retained inventory and shows a nearly constant value of $(12 \pm 1) \times 10^{20}$ D/m², consistent with the data point obtained from the damaged control sample (“No pTDS” in Fig. 6.1 and 6.2) which is plotted at 373 K on the x-axis in Fig. 6.3. Thus the independent NRA, pTDS, and final TDS techniques give consistent retained inventory measurements.

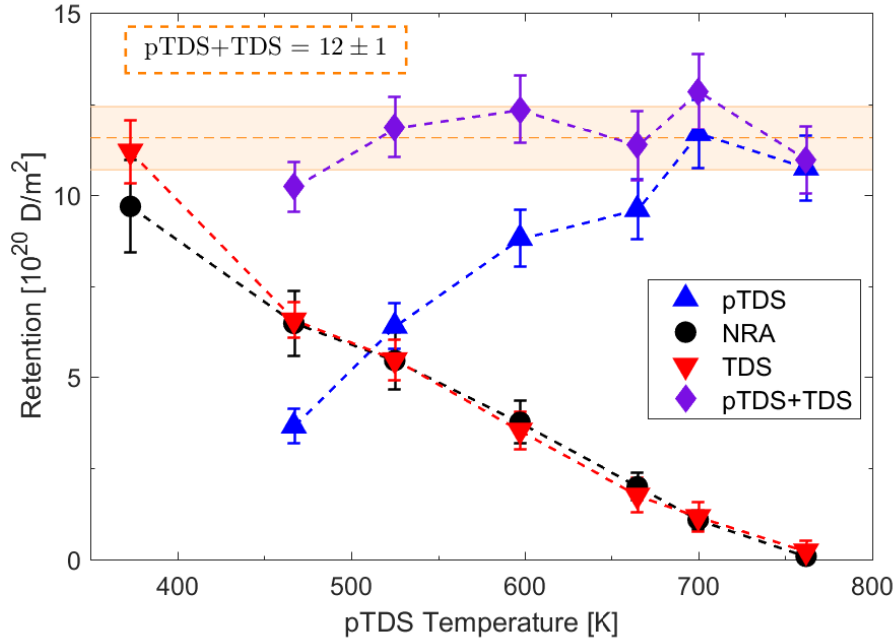


Figure 6.3: The sum total D retention measured in the first $5.5 \mu\text{m}$ through NRA and the bulk through TDS. Plotted at the plasma exposure sample temperature of 373 K, the “No pTDS” sample shows the largest deviation from NRA. The sum of D retention measured from pTDS and TDS is consistent as seen by the average (orange shaded region). Dashed lines are only shown to guide the eye.

6.4 Isolating Detrapping Energies

The simulation of the pTDS, NRA, and final TDS stages are well constrained by both the identical initial conditions and the controlled depopulation of each trap. Here we assume each trap concentration and spatial profile as well as the filling thereof during D implantation are the same for all samples prior to the application of the pTDS procedure. In what follows, we exploit the selective depopulation of traps with lower detrapping energies in order to isolate the spatial location and detrapping energy of the desorbed D. In order to do this, for a given NRA profile or pTDS release dataset, we subtract the next highest pTDS temperature dataset (i.e. consecutive pTDS temperatures). The difference then can be used to determine spatial location (from differential NRA data) or release temperatures (from differential pTDS data). Furthermore,

the spatial location of a given trap energy will be described by a spatial profile function ($f_k^j(x)$) that corresponds to the spatial distribution of the D that was released during consecutive pTDS exposures; we will find that this function will be zone (j) and trap type (k) dependent.

6.4.1 NRA Subtraction

The NRA D profiles shown in Fig. 6.1 display a distinctly different shape for pTDS samples subjected to peak-and-hold temperatures of 525 K and above. Fig. 6.2 shows the remaining D in these higher temperature pTDS samples are trapped in defects with increasing detrapping energy. Fig. 6.4 displays the concentration difference profiles (ΔC) computed as the difference between consecutive NRA D profiles and labeled by the two pTDS temperatures used to produce a given profile. The difference profiles for these higher temperature pTDS samples and the 762 K pTDS sample display a peak at a depth of 0.7-1.0 μm , in agreement with the SRIM predicted dpa profile (dot-dashed orange), showing that the computed dpa distribution at a given depth is correlated to the difference concentration at that location. We therefore use the SRIM predicted spatial profile to define the spatial profile function $f_{high}^{II}(x)$ for zone II, where the trap type ($k = high$) refers to high detrapping energies associated with higher temperature release.

In Fig. 6.5, the D concentration profile for the “No Cu” sample (black) displays a large near-surface component in zone I due to D₂ plasma exposure (note the much larger concentration scale compared to Fig. 6.4). The profile exponentially decays into the bulk as seen in previous work [32, 37]. An exponential fit (dot-dashed red) to the “No Cu” is shown with a characteristic decay length of 0.05 μm above an intrinsic concentration. The exponential fit to the plasma induced trap distribution in zone I is then chosen to define the spatial distribution $f_{low}^I(x)$, and is understood to have low detrapping energy traps (i.e. Fig. 4 shows $f_{high}^I(x)$ equals zero).

In order to isolate and determine the spatial location of low energy traps in zone II, both the “No Cu” and 597 K pTDS profiles are subtracted from the “No pTDS” profile (solid blue). First, noting the similarity in D profile for zone I between the “No Cu” and “No pTDS” NRA

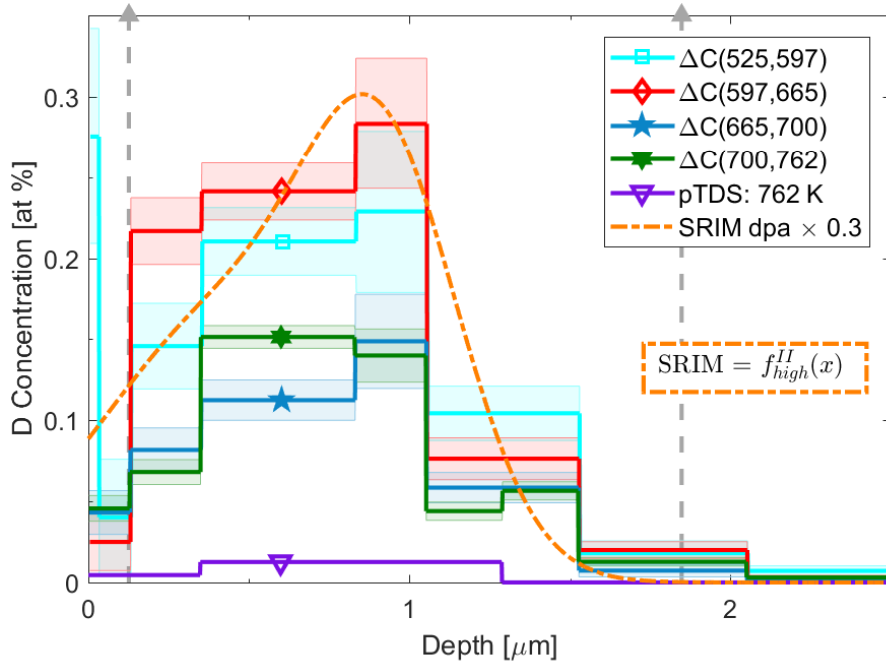


Figure 6.4: The difference in D concentration between consecutive pTDS samples are shown as solid lines. The damage profile of zone II is further defined and fit well by the SRIM dpa profile scaled to 0.3 for ease of comparison (dot-dashed orange).

data shown in Fig. 6.1, we assume the plasma induced traps are represented by the “No Cu” profile. Second, the samples with pTDS peak-and-hold temperature at 597 K and above display no additional zone I component. Lastly, as shown in Fig. 6.4, these higher temperature pTDS samples display a D concentration coincident with heavy ion induced traps located in zone II. Thus the remaining D found after subtracting both the “No Cu” and 525 K pTDS reveals the profile for heavy ion induced traps associated with lower detrapping energies. An empirical fit to this difference ($f_{low}^{II}(x)$) is shown in Fig.6.5 as the sum of two Gaussians (dot-dashed magenta) since the profile appears to have two distinct features. This difference-concentration distribution is quite distinct from both the near-surface zone I concentration profile, and the trapped D located within higher detrapping energy traps found in Fig. 6.4.

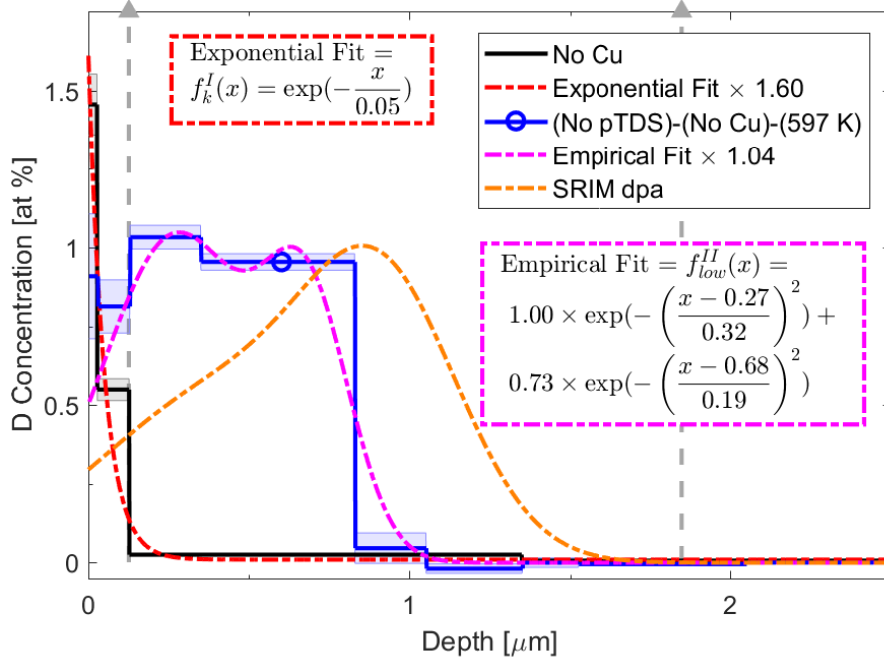


Figure 6.5: The ‘No Cu’ sample is shown as solid black with an exponential decay function (dot-dashed red). The solid blue line representing “No pTDS” subtracting both the “No Cu” and 597 K pTDS NRA profiles isolates the low energy traps due to heavy ion damage. An empirical fit (dot-dashed magenta) to this D profile is significantly shallower than the SRIM profile (dot-dashed orange).

6.4.2 TDS Subtraction

Similarly, the differences between the final TDS data obtained from consecutive pTDS peak-and-hold temperature runs are shown in Fig. 6.6. Using the difference-flux ($\Delta\Gamma$) TDS profiles, we can infer the minimum number of distinct traps in damaged W. The first difference (dark blue) is too broad to be due to a single trap but would appear to have at least two detrapping energies. The separation and width of each additional difference suggest at least four more individual detrapping energies. Note that the overlapping initial release of the last two differences (turquoise and green) is likely due to the same detrapping energy. Lastly, the highest pTDS temperature at 762 K (purple) may have a unique detrapping energy of its own as further evidenced by the corresponding NRA profile in Fig. 6.4. Thus, there are likely at 6 or 7 unique detrapping energies needed to model this data set obtained with a sample temperature of 373 K during plasma

exposure.

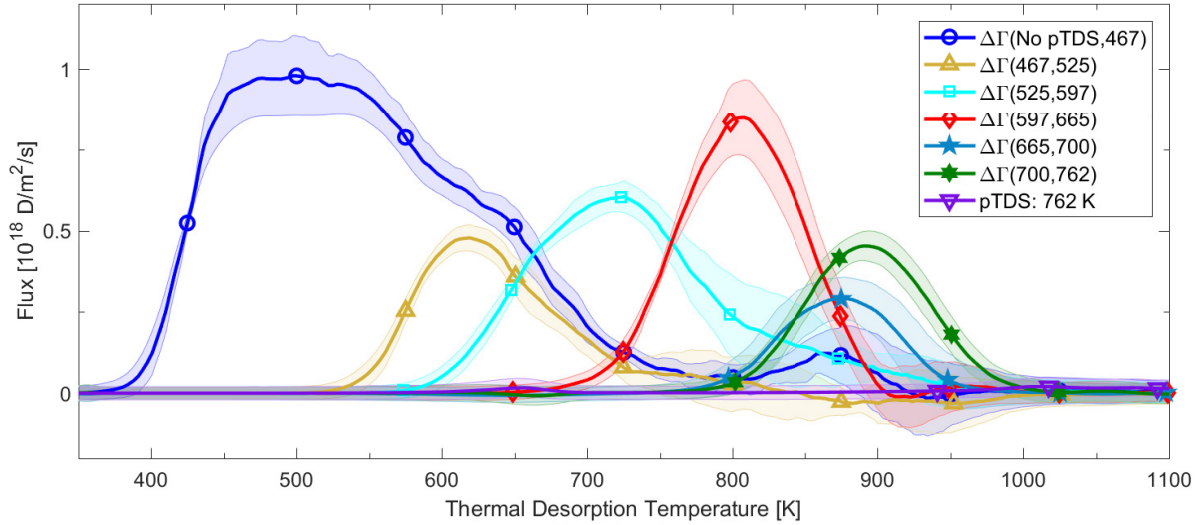


Figure 6.6: The difference in D flux during final TDS ($\Delta\Gamma$) for each consecutive pTDS sample pair are shown. The first dark blue line displays a broader primary peak than the other differences. Each of the remaining differences can be modeled with a single detrapping energy. All of the differences, except for the green line, begin to escape the sample at a unique temperature.

These difference datasets obtained from NRA and final TDS measurements can be used to constrain a reaction-diffusion model of the D in damaged W to determine the spatial distribution and trapping energy that best reproduces these observations. We take up this modeling effort in the following.

6.5 TMAP Simulation with PTTP

In order to use the verified and validated reaction-diffusion code TMAP7 [29, 25, 4] to model these results that require more than three types of traps with distinct detrapping energies, we employed a Pseudo Trap and Temperature Partitioning (PTTP) scheme as outlined and applied to TMAP7 [46]. In brief, for a particular temperature range this scheme utilizes a pseudo trap that accounts for multiple traps with deep energy wells that do not appreciably release but may act to trap mobile D from solute. When applied to TMAP7, only three traps are modeled at a time: the

Table 6.1: Summary of the fixed parameters and activation energies (E_a) used in the TMAP simulation. Note that the recombination coefficient is changed depending on the modeling phase: the Pick and Sonnenberg value is used during plasma implantation and the Anderl value during thermal desorption.

Parameter			E_a [eV]
D	2.9×10^{-7}	[m ² /s]	0.39
K_r^{plasma}	$3 \times 10^{-25} T^{-1/2}$	[m ⁴ /s]	-2.06
K_r^{TDS}	3.2×10^{-15}	[m ⁴ /s]	1.16
v_0	10^{13}	[1/s]	
R	0.65		
$r_{implant}$	4	[nm]	
$\sigma_{implant}$	2	[nm]	

two lowest detrapping energy traps are included and can act to both trap and detrap D atoms, and a pseudo trap (which models all traps with higher detrapping energies) is included and primarily acts to trap D atoms.

All the typical reaction-diffusion parameters as outlined in [46, 37] were used and detailed in Table 6.1. During the D₂ plasma exposure phase, the implanted D flux was simulated as a Gaussian with mean depth ($r_{implant}$) taken from Eckstein [16] and standard deviation ($\sigma_{implant}$) with a reflection coefficient (R). As seen in previous work [7], the use of Anderl’s recombination coefficient during the plasma phase leads to D retention that is much larger than experimentally observed. Either through enhanced reflection, re-emission, or recombination the total D retained must be reduced to match experiment. We chose the Pick and Sonnenberg value for surface recombination (K_r^{plasma}) during the plasma phase to produce retention commensurate with the dataset. Without D₂ plasma exposure (e.g. during the TDS phase), surface recombination is simulated using Anderl’s value (K_r^{TDS}).

The heavy ion damage, together with the intrinsic defects leftover after sample preparation and annealing act as the initial trap concentrations for zone II and III respectively. Since TMAP7 uses a static trap concentration, here we also take the plasma induced trap profile in zone I as an initial condition. The formation of plasma induced defects is postulated to be due to a

solute D saturated region stressing the near-surface zone I [32]. As detailed in [20], equation 6.1 estimates the diffusion limited D solute maximum concentration during D implantation. Using the parameters from Table 6.1 and sample temperature (T) during plasma exposure gives a D saturation level that approaches 2×10^{-4} at. %. TMAP simulations show that within 1 % of total exposure time (< 1 min), the solute concentration has reached this saturation value. Compared to the total plasma exposure time of over an hour, the time required for plasma to induce these traps through saturation of zone I is relatively short and simply approximated as an initial trap concentration.

$$C_{s,max} \approx \frac{(1 - R) \cdot \Gamma_{incident} \cdot r_{implant}}{n_W \cdot D(T)} \quad (6.1)$$

Equation 6.2 defines the total initial trap concentration ($C^o(x)$) as a summation over trap type and spatial zone. Each trap type (k) is identified by a distinct detrapping energy (E_k). Note that the traps are ordered according to increasing detrapping energy. Each spatial zone ($j = I, II, \text{ or } III$) has an associated profile function ($f_k^j(x)$), that is chosen according to the inferred trap distributions found from experimental data and shown in Fig. 6.4 and 6.5. All the profile functions are normalized to a peak value of unity. The profile function is multiplied by the peak concentration (C_k^j) for each trap and zone. For $j = I$, the exponential fit detailed in Fig. 6.5 defines the profile function. For $j = III$, the profile function is simply a constant. We also differentiate the particular trap profile in zone II for low and high energy traps as seen in Fig. 6.4 and 6.5. For $j = II$, the lower detrapping energies use the empirical fit shown in Fig. 6.5 for zone II, while the higher detrapping energies use the SRIM profile. As a result of constraining the profile functions by experiment, the peak concentration (C_k^j) for each trap (k) in each zone (j) and the detrapping energies (E_k) become the free parameters that can be adjusted within TMAP7 in order to fit the experimental NRA and TDS data. Note that the sample preparation and D implantation phase are assumed identical for all samples in this dataset, thus we need only model this part of the

experiment once for a given set of free parameters.

$$\begin{aligned}
 C^o(x) &= \sum_k C_k^o(x) \\
 &= \sum_k [C_k^I f_k^I(x) + C_k^{II} f_k^{II}(x) + C_k^{III} f_k^{III}(x)]
 \end{aligned}
 \tag{6.2}$$

6.5.1 Fitting Results

The complete cycle of D₂ plasma exposure, pTDS, and final TDS was simulated for each sample and all free parameters were optimized utilizing the technique of simulated annealing [23]. During the simulated annealing, the free parameters were constrained according to the differences in consecutive TDS and NRA data previously outlined. The simulation of a particular set of trap parameters results in unique NRA and TDS profiles. Both the experimental and simulation data were interpolated to a finely spaced grid to directly compare the “goodness of fit.” The Normalized Root Mean Square Error (NRMSE) as well as the Normalized Mean Absolute Error (NMAE), defined by the absolute difference between experiment and simulation, were the metrics used to determine the optimal fit. In addition, the resulting NRMSE and NMAE were weighted with respect to their total D retention and added together to determine a single fit metric. For instance, the “No pTDS” sample had the highest D retention and had the largest weight while the highest temperature pTDS at 762 K contributed the least weight when determining the best fit parameters.

The number of traps used to simulate the experiment was varied from 5 to 9. As outlined in the section on TDS subtraction, the best fit was found with 6 traps with detrapping energies near 1.0, 1.2, 1.4, 1.6, 1.8, and 1.9 eV. Using 7 traps, nearly the same energies were found and one additional energy of 2.4 eV produced nearly the same fit metric. The highest pTDS sample at 762 K may either be due to a partially released 1.9 eV trap or a filled 2.4 eV trap. The experimental TDS release temperature appears significantly higher than a 1.9 eV trap. By 762 K,

Table 6.2: Summary of the best fit parameters for each trap (k). The peak concentrations (C_k^j) in each zone (j) and the detrapping energies (E_k) modeled using the PTTP scheme.

k	C_k^I	C_k^{II}	$f_k^{II}(x)$	C_k^{III}	E_k
1	1.12	0.20	Empirical	0.0013	0.99
2	0.39	0.27	Empirical	0.0017	1.15
3	0.40	0.44	Empirical	0.0014	1.35
4	0.30	0.19	SRIM	0.0013	1.56
5	0.00	0.48	SRIM	0.0008	1.76
6	0.00	0.20	SRIM	0.0000	1.94
	[at.%]	[at.%]	Profile	[at.%]	[eV]

an appreciable amount of vacancy agglomeration may have occurred during the peak-and-hold that is not modeled but may account for the higher temperature release. We also note that the results shown are based on the PTTP scheme that assumes a minimal separation in detrapping energies. For instance, a difference below 0.1 eV for consecutive detrapping energies leads to a significant error as outlined in [46]. Table 6.2 provides a summary of the resulting trap concentrations and energies found to give the best fit to the NRA and pTDS data with the least number of traps. The total trap concentration, $C^o(x)$, is shown in Fig. 6.7 (solid black) together with the k -th trap concentration profiles, $C_k^o(x)$, given as the dot-dashed lines. The measured NRA profile from the “No pTDS” sample is also shown and has a shape that overlays with the $C^o(x)$ total trap concentration profile. Examining the absolute value of the trap concentration in Fig. 6.7 and the absolute trapped D magnitude shown in Fig. 6.4, we can see that the two are in absolute agreement if, prior to any pTDS, each trap contains an average about 1.5 D atoms/trap.

The simulated NRA profiles and final TDS release histories (dashed lines) are compared to the experimental data (solid lines) in Fig. 6.8 and 6.9 respectively. The simulated NRA and TDS produced reasonable fits with normalized fit metric values of ~ 0.7 for both. A possible reason for the discrepancy may be due to using detrapping energies separated by at least 0.1 eV. For instance, what appears as a single peak in Fig. 6.9 can be made of several nearby detrapping energies. If three detrapping energies made the peak near 620 K, the lowest energy may be

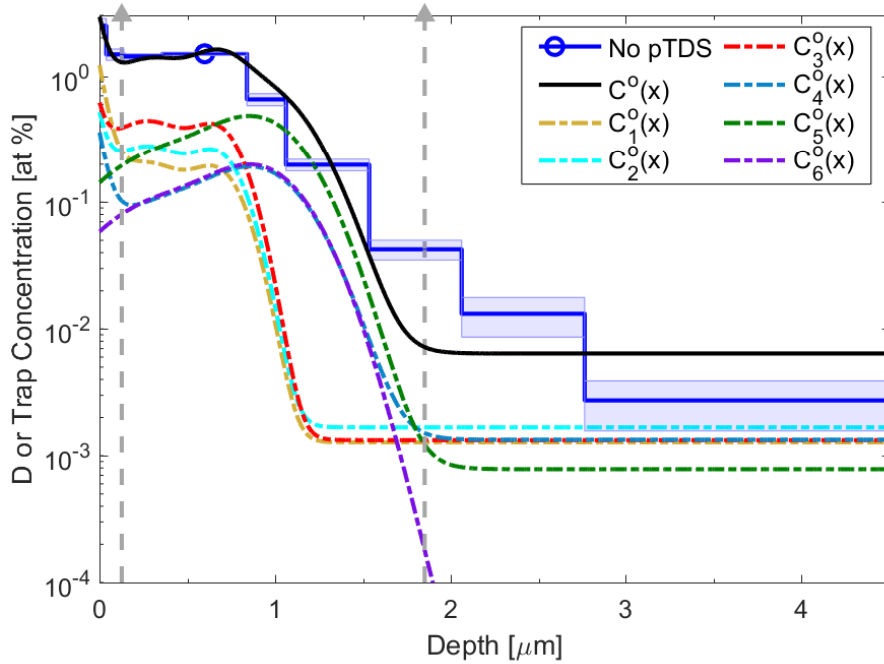


Figure 6.7: The total trap concentration (black) compared to the “No pTDS” NRA data (blue). The individual trap concentrations for $k = 1-6$ are shown as dot-dashed lines.

completely released, the middle partially, and the highest remained filled for a pTDS at 467 K (gold). Several more experimental data points, that is more samples prepared with intermediate pTDS peak-and-hold temperatures, would be needed to discern if this was indeed the case.

6.6 Discussion

The detrapping energies found here are similar to values observed in previous studies. Ogorodnikova speculated the type of defect likely associated with each detrapping energy [30] and suggested that the two lowest energies at 1.0 and 1.2 eV are likely due to grain boundaries and dislocations. Trap 3 at 1.4 eV is likely due to mono-vacancies as seen by studies that use light ion damage to eject a single W from a lattice site [61]. For traps 4 through 6 with detrapping energies of 1.5 to 2.4 eV, the defects are likely related to vacancy complexes, voids, and dislocations.

Recent work done with x-ray spectroscopy [49] has quantified the number of defects due to dislocation loops. For a single crystalline W sample damaged to 0.2 dpa with Cu ions at 5 MeV,

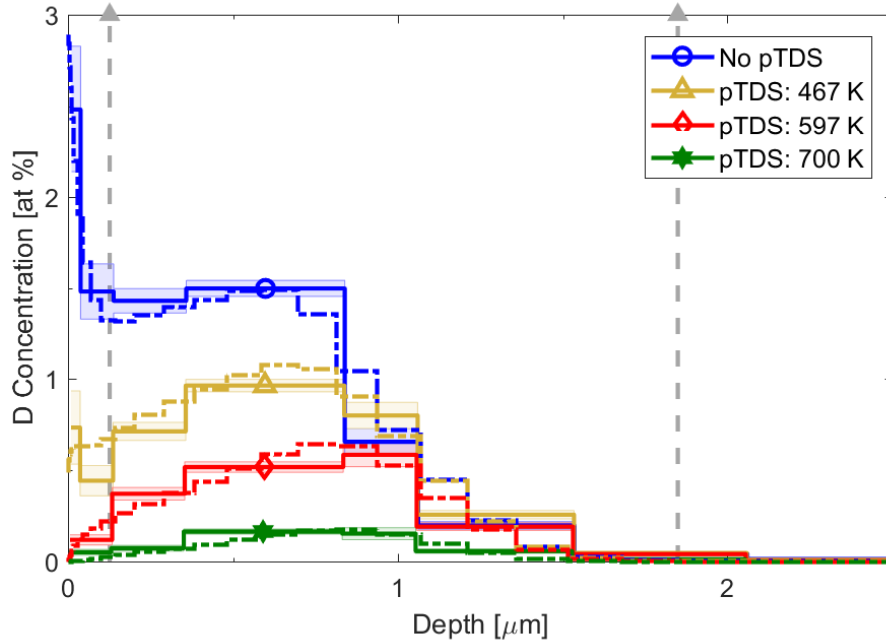


Figure 6.8: The comparison of the NRA data (solid) and the simulation result (dashed) using the optimized fit parameters, summarized in Table 6.2. For clarity, only 4 samples are shown.

the vacancy-type dislocation loop concentration was near 0.1 at.%. The scattering experiment was not spatially resolved but averaged over the first few microns of the W surface, and could not resolve vacancy defects with radii below 5 Å. Thus that quoted vacancy concentration is for larger vacancy complexes averaged over the near-surface region and primarily includes large vacancy complexes. The x-ray scattering results indicated that the average size of a vacancy complex was (6.76 ± 0.16) Å, which would correspond to a dislocation loop incorporating ~ 30 W atoms. Traps 4-6 inferred in our work here have energies that are consistent with such larger vacancy complexes and have atomic concentrations of the same order of magnitude as these x-ray scattering results. The x-ray data also yields the size distribution, where the largest complexes are nearly two orders of magnitude lower in concentration than the smallest (5 Å) observable dislocation loop. Having the largest detrapping energy, the possible 7th is likely due to a large vacancy complex and has a concentration nearly two order of magnitude lower than traps 4-6. This initial necessarily brief comparison between our inferred results and the x-ray scattering results thus shows a similar

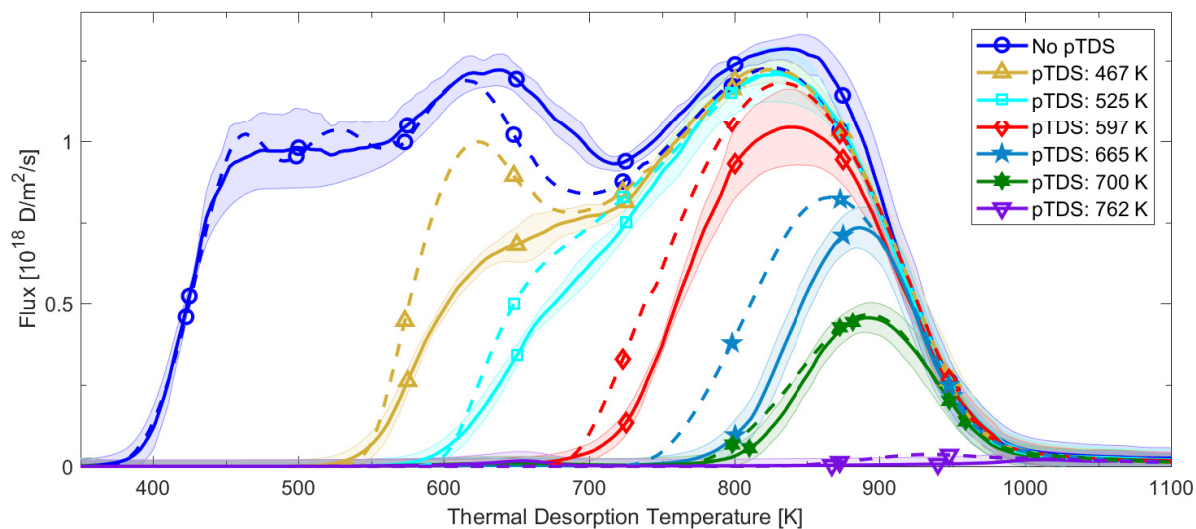


Figure 6.9: The comparison of the TDS data (solid) and the simulation result (dashed) using the optimized fit parameters, summarized in Table 6.2.

order-of-magnitude defect density and similar inferred defect size. Clearly additional work focused on direct measurement of defects, determination of the corresponding trapping energies from computational modeling and D atom capacity is needed in order to determine if the observed D retention and release is self-consistent with actual defect structures produced in the W material.

The spatial segregation of ion damage-induced defects shown in Fig. 6.5 suggest insights into how to compare D retention from ion beam damage with what might be expected to occur from neutron damage. While the neutron only interacts with the nuclei of lattice W, the electronic stopping loss of heavy ions produces a distinctly unique profile for various defects. Our results show evidence for a significant deviation in the spatial location of high and low detrapping energies. The defects with higher detrapping energies (traps $k = 4-6$) correlate to the SRIM predicted Bragg peak while defects with low detrapping energies (e.g. mono-vacancies and small vacancy clusters) are located between the surface and the Bragg peak location. Noting that the neutron damage profile in PFMs should yield similar mono-vacancy and small vacancy clusters, we are then led to speculate that retention and release from such neutron-induced damage might appear similar to what we observe in the intermediate spatial region of our experiments.

Finally we note that SRIM is a kinetic Monte-Carlo code that does not simulate the accumulation or agglomeration of defects [62]. Each simulated energetic ion interacts with a new, undisturbed amorphous target that does not retain the induced damage from previous ions and thus has no memory. The formation of defect structures such as loops or clusters is not accounted for as only displacements are counted when collisions impart enough energy to a lattice atom (i.e. above the displacement threshold). Qualitatively, SRIM predicts that the density of collision cascades increases as the heavy ion projectile loses energy to recoils and the highest density occurs at the peak dpa depth. Closer to the surface, the initially highly energetic heavy ions impart less energy to lattice atoms and are more likely to form smaller collision cascades nearer to the surface. The result may then be a segregation of defects, with more lower-order vacancies produced towards the surface and larger vacancy clusters closer to the peak dpa zone.

6.7 Summary

Trapped D in Cu ion damaged W was sequentially depopulated with increasing temperature to determine the spatial profile and detrapping energies. The total D retention measured through pTDS, NRA, and TDS are shown to be in excellent agreement as well as demonstrating the repeatability of sample preparation. Comparing the NRA data from the control sample, without pTDS, and the lowest pTDS temperatures demonstrates that all of the plasma induced defects in the near-surface were depopulated by holding the sample at 597 K. In addition, the majority of retained D is depopulated by a pTDS temperature of 762 K. For pTDS peak-and-hold temperatures between 525 and 762 K, the D profiles measured via NRA are similar to the displacement damage profile predicted by SRIM. The full cycle of D₂ plasma loading, to pTDS, and finally a final TDS cycle was modeled with TMAP7 utilizing a Pseudo Trap and Temperature Partition (PTTP) scheme. Detrapping energies near 1.0, 1.2, 1.4, 1.6, 1.8, and 1.9 eV were found to fit the experimental data.

6.8 Acknowledgments

This work was supported by U.S. Department of Energy under DE-FG02-07ER54912 and DE-SC0001999 as well as the University of California Office of Presidential Research Fund under 12-LR-237801. Part of this work has been carried out within the framework of the EUROfusion Consortium within the work project PFC and has received funding from the Euratom research and training programme 2014-2018 under grant agreement No 633053. The views and opinions expressed herein do not necessarily reflect those of the European Commission. Chapter 6, including text and data, is in part a reprint of the material as it appears in M.J. Simmonds, T. Schwarz-Selinger, J.H. Yu, M.J. Baldwin, R.P. Doerner, G.R. Tynan, Isolating the Detrapping of Deuterium in Heavy Ion Damaged Tungsten via Partial Thermal Desorption, *J. Nucl. Mater.* submitted (2018). The dissertation author was the primary investigator and author of this paper.

Chapter 7

Conclusions and Future Work

The experimental work presented in this thesis aimed at further understanding the process of defect production and H isotope retention in W. The key results from Chapters 4 - 6 are detailed below:

- Dynamic annealing (i.e. concurrent heavy ion damage at elevated sample temperature) was shown to significantly reduce the production of heavy-ion induced defects, even for sample temperatures well below the recrystallization temperature of W.
- Near 1243 K, the competition between dynamic annealing and heavy-ion induced defect production results in D retention comparable to a control sample with no heavy-ion induced defects, much lower retention than the samples damaged at lower temperatures.
- A Pseudo Trap and Temperature Partition (PTTP) scheme was developed to expand the use of a validated and verified reaction-diffusion code (TMAP), previously limited to 3 concurrent traps.
- Using the PTTP scheme, 6 unique detrapping energies were needed to accurately fit experimental NRA and TDS retention data from heavy-ion damaged W samples.

- A partial TDS (pTDS) experiment was performed to selectively depopulate and further isolate both the detrapping energies as well as the spatial location of various traps.
- Using the PTTP scheme, the pTDS samples revealed a segregation of defects in which lower detrapping energy traps displayed a significantly different spatial profile than traps with higher detrapping energy.
- The various pTDS samples were generally well fit by 6 unique detrapping energies for all pTDS peak-and-hold temperatures below 700 K. The W sample with the highest temperature pTDS at 762 K, had a poor fit that may be explained by vacancy mobility/agglomeration during the D depopulation of the peak-and-hold phase.

7.1 TDS and Detrapping Energies

There is still significant disagreement between Density Functional Theory (DFT) calculations and experimental data. One reason for the discrepancy is the identification of detrapping energies with defect type. The primary method of measuring detrapping energies depends on the analysis of experimental TDS data. Though multiple release peaks are visible in the desorption data, each release peak may be due to multiple nearby detrapping energies.

As shown in the introduction, I presented a way to further analyze TDS data and produce a cleaner desorption profile. An ongoing collaborative effort to compare the various experimental TDS data among many different research groups has yielded some discouraging results. This “Round Robin” experiment involved a set of samples identically prepared with heavy ion damage and D plasma exposure. Each group was given instructions on how to take the data and perform a set of TDS runs, including a background run with no sample. Despite the similarity of samples, a wide range of desorption profiles were collected from the groups. Though most had the same shape, the width of each peak and the position with respect to temperature varied significantly. One possible source of error could be the presence of surface contaminants such as C and O that

may alter the recombination and release of H isotopes from the surface. At the recent Hydrogen Workshop following the 2018 Plasma Surface Interactions conference, it was collectively agreed that a set of best practices and increased analysis of the surface conditions are needed.

7.2 Further Isolating Defects

The partial thermal desorption scheme to depopulate traps selectively may be used in conjunction with other experimental techniques to selectively target traps according to detrapping energy. For instance, Positron Annihilation Lifetime Spectroscopy (PALS) is a technique of implanting positrons within a material that survive longer when they reach vacancy type defects. The larger the vacancy, the longer the lifetime of the positron before annihilation with an electron that in turn produces two 511 keV photons. By analyzing the photon counts and lifetimes, the size of the vacancy type defects can be inferred. By selectively depopulating various traps, higher detrapping energy defects will retain D and not be able to hold positrons. Thus we can isolate the PALS spectra in this manner and conclusively determine the association of various vacancy type defect sizes with detrapping energies.

Similar to this methodology for PALS, we plan to investigate the effect of D occupation in traps on x-ray diffraction data. The various diffraction patterns have already been used to analyze both vacancy and interstitial type dislocation defects. We suspect the presence of D in dislocation defect sites will alter the resulting pattern. While PALS can only detect open-site defects, x-ray diffraction is sensitive to interstitial type defects. Depending on how sensitive the pattern is to the presence of D, this may provide some of the first direct evidence for D trapping at interstitial defects. Additionally, the occupation of D in traps is theorized to stabilize traps. Partial TDS may be used to selectively depopulate traps as well as partially anneal defects that have liberated D.

7.3 TMAP Modification and Updates

The original version of TMAP was written in FORTRAN in the late 1980s and allowed for only a single type of defect with an associated detrapping energy. The current version, TMAP7, added two more traps and made use of desktop computing capabilities of the mid 2000s. The addition of more traps lead to significantly longer computational times. With the further advancement of computational speed and memory, even more traps could easily be included in the code. TMAP also allows for the simulated material to be separated into diffusion segments (e.g. a co-deposit layer on top of a pure material) that may be solved in parallel on separate CPU cores or threads. Additional advancements in computational algorithms (e.g. approximating the inverse of a matrix) have led to faster and higher order convergence. While the diffusion equations for each segment are not inherently parallel, the current version of TMAP can only be run on a single core. The process of finding a fit to the experimental data involves varying the trap parameters and choosing the best fit. This process can be sped by either using multiple CPU cores or threads to parallelize the performance of each TMAP calculation with varied parameters. Furthermore, directly adapting the code to include the PTPP scheme outlined in chapter 5 may further increase computational speed. At least while varying trap parameters over a large parameter space, there is a significant advantage to increased throughput of simulations. Only once the trap parameters are nearly optimized would the more exact, but slower to compute solution be advisable.

Bibliography

- [1] Eurofusion. <https://www.euro-fusion.org/>, 2018.
- [2] Iter organization. <https://www.iter.org/>, 2018.
- [3] V.Kh. Alimov, B. Tyburska-Pschel, Y. Hatano, J. Roth, K. Isobe, M. Matsuyama, and T. Yamanishi. The effect of displacement damage on deuterium retention in iter-grade tungsten exposed to low-energy, high-flux pure and helium-seeded deuterium plasmas. Journal of Nuclear Materials, 420(1):370 – 373, 2012.
- [4] J. Ambrosek and G.R. Longhurst. Verification and validation of tmap7. Idaho National Engineering and Environment Laboratory INEEL/EXT-04-01657 (Rev. 2), 2008.
- [5] T. Amino, K. Arakawa, and H. Mori. Activation energy for long-range migration of self-interstitial atoms in tungsten obtained by direct measurement of radiation-induced point-defect clusters. Philosophical Magazine Letters, 91(2):86–96, 2011.
- [6] M.J. Baldwin and R.P. Doerner. Helium induced nanoscopic morphology on tungsten under fusion relevant plasma conditions. Nuclear Fusion, 48(3):035001, 2008.
- [7] M.J. Baldwin and R.P. Doerner. Hydrogen isotope transport across tungsten surfaces exposed to a fusion relevant he ion fluence. Nuclear Fusion, 57(7):076031, 2017.
- [8] J.L. Barton, Y.Q. Wang, T. Dittmar, R.P. Doerner, and G.R. Tynan. Deuterium retention in tungsten after heavy ion damage and hydrogen isotope exchange in {PISCES}. Nuclear Instruments and Methods in Physics Research Section B: Beam Interactions with Materials and Atoms, 332(0):275 – 279, 2014.
- [9] J.L. Barton, Y.Q. Wang, R.P. Doerner, and G.R. Tynan. Model development of plasma implanted hydrogenic diffusion and trapping in ion beam damaged tungsten. Nuclear Fusion, 56(10):106030, 2016.
- [10] R. Bisson, S. Markelj, O. Mourey, F. Ghiorghiu, K. Achkasov, J.-M. Layet, P. Roubin, G. Cartry, C. Grisolia, and T. Angot. Dynamic fuel retention in tokamak wall materials: An in situ laboratory study of deuterium release from polycrystalline tungsten at room temperature. Journal of Nuclear Materials, 467, Part 1:432 – 438, 2015.

- [11] H. Bolt, V. Barabash, G. Federici, J. Linke, A. Loarte, J. Roth, and K. Sato. Plasma facing and high heat flux materials needs for {ITER} and beyond. Journal of Nuclear Materials, 307–311, Part 1(0):43 – 52, 2002.
- [12] L. Buzi, G. De Temmerman, D. Matveev, M. Reinhart, T. Schwarz-Selinger, M. Rasinski, B. Unterberg, Ch. Linsmeier, and G. Van Oost. Surface modifications and deuterium retention in polycrystalline and single crystal tungsten as a function of particle flux and temperature. Journal of Nuclear Materials, 495:211 – 219, 2017.
- [13] S. Cui, M. Simmonds, W. Qin, F. Ren, G. R. Tynan, R. P. Doerner, and R. Chen. Thermal conductivity reduction of tungsten plasma facing material due to helium plasma irradiation in pisces using the improved 3-omega method. Journal of Nuclear Materials, 486:267 – 273, 2017.
- [14] A. Debelle, M.F. Barthe, and T. Sauvage. First temperature stage evolution of irradiation-induced defects in tungsten studied by positron annihilation spectroscopy. Journal of Nuclear Materials, 376(2):216 – 221, 2008.
- [15] ASTM E521. Standard Practice for Neutron Radiation Damage Simulation by Charged-Particle Irradiation. 1996. Reapproved 2009.
- [16] W. Eckstein. Calculated sputtering, reflection and range values. IPP-Report IPP 9/132, 2002.
- [17] H. Eleveld and A. van Veen. Void growth and thermal desorption of deuterium from voids in tungsten. Journal of Nuclear Materials, 212:1421 – 1425, 1994.
- [18] F. Ferroni, X. Yi, K. Arakawa, S. P. Fitzgerald, P. D. Edmondson, and S. G. Roberts. High temperature annealing of ion irradiated tungsten. Acta Materialia, 90(0):380 – 393, 2015.
- [19] R. Frauenfelder. Solution and diffusion of hydrogen in tungsten. Journal of Vacuum Science and Technology, 6(3):388–397, 1969.
- [20] L. Gao, W. Jacob, U. von Toussaint, A. Manhard, M. Balden, K. Schmid, and T. Schwarz-Selinger. Deuterium supersaturation in low-energy plasma-loaded tungsten surfaces. Nuclear Fusion, 57(1):016026, 2017.
- [21] D.M. Goebel, G. Campbell, and R.W. Conn. Plasma surface interaction experimental facility (pisces) for materials and edge physics studies. Journal of Nuclear Materials, 121:277 – 282, 1984.
- [22] L.K. Keys and J. Moteff. Neutron irradiation and defect recovery of tungsten. Journal of Nuclear Materials, 34(3):260 – 280, 1970.
- [23] S. Kirkpatrick, C. D. Gelatt, and M. P. Vecchi. Optimization by Simulated Annealing. Science, 220:671–680, May 1983.

- [24] Y. Liu, Y. Zhang, H. Zhou, G. Lu, F. Liu, and G.N. Luo. Vacancy trapping mechanism for hydrogen bubble formation in metal. Phys. Rev. B, 79:172103, May 2009.
- [25] G.R. Longhurst. Tmap7 user manual. Idaho National Engineering and Environment Laboratory INEEL/EXT-04-02352(Rev. 2), 2008.
- [26] E. Markina, M. Mayer, A. Manhard, and T. Schwarz-Selinger. Recovery temperatures of defects in tungsten created by self-implantation. Journal of Nuclear Materials, 463:329 – 332, 2015.
- [27] M. Mayer. Simnra, a simulation program for the analysis of nra, rbs and erda. AIP Conference Proceedings, 475(1):541–544, 1999.
- [28] M. Mayer, E. Gauthier, K. Sugiyama, and U. von Toussaint. Quantitative depth profiling of deuterium up to very large depths. Nuclear Instruments and Methods in Physics Research Section B: Beam Interactions with Materials and Atoms, 267(3):506 – 512, 2009.
- [29] B.J. Merrill, J.L. Jones, and D.F. Holland. Tmap/mod 1: Tritium migration analysis program code description and user’s manual. Idaho National Engineering Laboratory EGG-EP-7407, EG and G, 1986.
- [30] O. V. Ogorodnikova. Fundamental aspects of deuterium retention in tungsten at high flux plasma exposure. Journal of Applied Physics, 118(7):074902, 2015.
- [31] O. V. Ogorodnikova, S. Markelj, and U. von Toussaint. Interaction of atomic and low-energy deuterium with tungsten pre-irradiated with self-ions. Journal of Applied Physics, 119(5):054901, 2016.
- [32] O. V. Ogorodnikova, J. Roth, and M. Mayer. Ion-driven deuterium retention in tungsten. Journal of Applied Physics, 103(3):034902, 2008.
- [33] O.V. Ogorodnikova, Yu. Gasparyan, V. Efimov, . Ciupiski, and J. Grzonka. Annealing of radiation-induced damage in tungsten under and after irradiation with 20 mev self-ions. Journal of Nuclear Materials, 451(13):379 – 386, 2014.
- [34] O.V. Ogorodnikova, J. Roth, and M. Mayer. Deuterium retention in tungsten in dependence of the surface conditions. Journal of Nuclear Materials, 313316:469 – 477, 2003.
- [35] O.V. Ogorodnikova, B. Tyburska, V.Kh. Alimov, and K. Ertl. The influence of radiation damage on the plasma-induced deuterium retention in self-implanted tungsten. Journal of Nuclear Materials, 415(1, Supplement):S661 – S666, 2011.
- [36] V. Philipps. Tungsten as material for plasma-facing components in fusion devices. Journal of Nuclear Materials, 415(1, Supplement):S2 – S9, 2011. Proceedings of the 19th International Conference on Plasma-Surface Interactions in Controlled Fusion.
- [37] M. Poon, A.A. Haasz, and J.W. Davis. Modeling deuterium release during thermal desorption of d+ -irradiated tungsten. Journal of Nuclear Materials, 374(3):390 – 402, 2008.

- [38] S. Qin, S. Jin, D. Zou, L. Cheng, X. Shu, Q. Hou, and G. Lu. The effect of inert gas pre-irradiation on the retention of deuterium in tungsten: A tmap investigation combined with first-principles method. Fusion Engineering and Design, 121:342 – 347, 2017.
- [39] J. Roth, E. Tsitrone, T. Loarer, V. Philipps, S. Brezinsek, A. Loarte, G. F. Counsell, R. P. Doerner, K. Schmid, O. V. Ogorodnikova, and R. A. Causey. Tritium inventory in iter plasma-facing materials and tritium removal procedures. Plasma Physics and Controlled Fusion, 50(10):103001, 2008.
- [40] S. Ryabtsev, Yu. Gasparyan, M. Zibrov, A. Shubina, and A. Pisarev. Deuterium thermal desorption from vacancy clusters in tungsten. Nuclear Instruments and Methods in Physics Research Section B: Beam Interactions with Materials and Atoms, 382:101 – 104, 2016. The 21st International workshop on Inelastic Ion Surface Collisions (IISC-21).
- [41] S. Sakurada, K. Yuyama, Y. Uemura, H. Fujita, C. Hu, T. Toyama, N. Yoshida, T. Hinoki, S. Kondo, M. Shimada, D. Buchenauer, T. Chikada, and Y. Oya. Annealing effects on deuterium retention behavior in damaged tungsten. Nuclear Materials and Energy, 9:141 – 144, 2016.
- [42] K. Schmid and U. von Toussaint. Statistically sound evaluation of trace element depth profiles by ion beam analysis. Nuclear Instruments and Methods in Physics Research Section B: Beam Interactions with Materials and Atoms, 281(0):64 – 71, 2012.
- [43] T. Schwarz-Selinger. Deuterium retention in mev self-implanted tungsten: Influence of damaging dose rate. Nuclear Materials and Energy, 12:683 – 688, 2017. Proceedings of the 22nd International Conference on Plasma Surface Interactions 2016, 22nd PSI.
- [44] M. Shimada, G. Cao, Y. Hatano, T. Oda, Y. Oya, M. Hara, and P. Calderoni. The deuterium depth profile in neutron-irradiated tungsten exposed to plasma. Physica Scripta, 2011(T145):014051, 2011.
- [45] M.J. Simmonds, Y.Q. Wang, J.L. Barton, M.J. Baldwin, J.H. Yu, R.P. Doerner, and G.R. Tynan. Reduced deuterium retention in simultaneously damaged and annealed tungsten. Journal of Nuclear Materials, 494:67 – 71, 2017.
- [46] M.J. Simmonds, J.H. Yu, Y.Q. Wang, M.J. Baldwin, R.P. Doerner, and G.R. Tynan. Expanding the capability of reaction-diffusion codes using pseudo traps and temperature partitioning: Applied to hydrogen uptake and release from tungsten. Journal of Nuclear Materials, 508:472 – 480, 2018.
- [47] C. H. Skinner, A. A. Haasz, V. Kh. Alimov, N. Bekris, R. A. Causey, R. E. H. Clark, J. P. Coad, J. W. Davis, R. P. Doerner, M. Mayer, A. Pisarev, J. Roth, and T. Tanabe. Recent advances on hydrogen retention in iters plasma-facing materials: Beryllium, carbon, and tungsten. Fusion Science and Technology, 54(4):891–945, 2008.

- [48] R.E. Stoller, M.B. Toloczko, G.S. Was, A.G. Certain, S. Dwaraknath, and F.A. Garner. On the use of {SRIM} for computing radiation damage exposure. Nuclear Instruments and Methods in Physics Research Section B: Beam Interactions with Materials and Atoms, 310:75 – 80, 2013.
- [49] Peihao Sun, Yongqiang Wang, Mungo Frost, Christopher Schnwlder, Abraham L. Levitan, Mianzhen Mo, Zhijiang Chen, Jerome B. Hastings, George R. Tynan, Siegfried H. Glenzer, and Philip Heimann. Characterization of defect clusters in ion-irradiated tungsten by x-ray diffuse scattering. Journal of Nuclear Materials, 2018.
- [50] M.H.J. 't Hoen, M. Mayer, A.W. Kleyn, H. Schut, and P.A. Zeijlmans van Emmichoven. Reduced deuterium retention in self-damaged tungsten exposed to high-flux plasmas at high surface temperatures. Nuclear Fusion, 53(4):043003, 2013.
- [51] K. J. Taylor, S. Yun, and G. R. Tynan. Control of plasma parameters by using noble gas admixtures. Journal of Vacuum Science & Technology A: Vacuum, Surfaces, and Films, 22(5):2131–2138, 2004.
- [52] D. Terentyev, A. Dubinko, A. Bakaeva, and G. De Temmerman. Strong sub-surface plastic deformation induced by high flux plasma in tungsten. Fusion Engineering and Design, 124:405 – 409, 2017. Proceedings of the 29th Symposium on Fusion Technology (SOFT-29) Prague, Czech Republic, September 5-9, 2016.
- [53] G. R. Tynan, A. D. Bailey III, G. A. Campbell, R. Charatan, A. de Chambrier, G. Gibson, D. J. Hemker, K. Jones, A. Kuthi, C. Lee, T. Shoji, and M. Wilcoxson. Characterization of an azimuthally symmetric helicon wave high density plasma source. Journal of Vacuum Science & Technology A, 15(6):2885–2892, 1997.
- [54] G.R. Tynan, R.P. Doerner, J. Barton, R. Chen, S. Cui, M. Simmonds, Y. Wang, J.S. Weaver, N. Mara, and S. Pathak. Deuterium retention and thermal conductivity in ion-beam displacement-damaged tungsten. Nuclear Materials and Energy, 12:164 – 168, 2017. Proceedings of the 22nd International Conference on Plasma Surface Interactions 2016, 22nd PSI.
- [55] W.R. Wampler. Ion beam analysis for fusion energy research. Nuclear Instruments and Methods in Physics Research Section B: Beam Interactions with Materials and Atoms, 219-220:836 – 845, 2004. Proceedings of the Sixteenth International Conference on Ion Beam Analysis.
- [56] P. Wang, W. Jacob, L. Gao, T. Drbeck, and T. Schwarz-Selinger. Comparing deuterium retention in tungsten films measured by temperature programmed desorption and nuclear reaction analysis. Nuclear Instruments and Methods in Physics Research Section B: Beam Interactions with Materials and Atoms, 300:54 – 61, 2013.
- [57] B.D. Wirth, K. Nordlund, D.G. Whyte, and D. Xu. Fusion materials modeling: Challenges and opportunities. MRS Bulletin, 36(3):216222, 2011.

- [58] J.H. Yu, M. Simmonds, M.J. Baldwin, and R.P. Doerner. Deuterium desorption from tungsten using laser heating. Nuclear Materials and Energy, 12:749 – 754, 2017. Proceedings of the 22nd International Conference on Plasma Surface Interactions 2016, 22nd PSI.
- [59] A. Zalonik, S. Markelj, T. Schwarz-Selinger, and K. Schmid. Deuterium atom loading of self-damaged tungsten at different sample temperatures. Journal of Nuclear Materials, 496:1 – 8, 2017.
- [60] J.P. Zhu, X. Xiao, S. Yan, Y. Gao, J.M. Xue, and Y.G. Wang. Measurement of differential cross section of $d(3\text{He,p})^4\text{He}$ from 0.8mev to 3.6mev. Nuclear Instruments and Methods in Physics Research Section B: Beam Interactions with Materials and Atoms, 412:81 – 85, 2017.
- [61] M. Zibrov, S. Ryabtsev, Yu. Gasparyan, and A. Pisarev. Experimental determination of the deuterium binding energy with vacancies in tungsten. Journal of Nuclear Materials, 477:292 – 297, 2016.
- [62] J.F. Ziegler, J. Biersack, and U. Littmark. The stopping and range of ions in matter. Pergamon Press, 1985.